Institut für Theoretische Physik
Fakultät Mathematik und Naturwissenschaften
Technische Universität Dresden

Rare-gas clusters in intense VUV laser fields

Dissertation
zur Erlangung des akademischen Grades
Doctor rerum naturalium

vorgelegt von
Ionuţ Georgescu
geboren am 15.04.1980 in Braşov

Dresden 2008

Eingereicht am 22.02.2008

1. Gutachter: _____
2. Gutachter: _____
3. Gutachter: _____

Verteidigt am _____

Contents

4

Chapter 1

Introduction

The quest for structural information with atomic resolution, time resolved on the time scale of atomic motion, has lead to the development of novel light sources: free electrons lasers (FEL), as those under construction at LCLS in Stanford, at DESY in Hamburg or at RIKEN in Japan and attosecond laser pulses in the extreme ultraviolet (XUV).

Structural information at the atomic level has been obtained so far at synchrotron facilities by X-ray diffraction, which relies on the ability to bring the sample in crystalline form. All objects scatter X-rays, but regular arrangement of several identical copies leads to coherent superposition of the scattered light at the Bragg peaks, greatly amplifying the signal and lowering the demands on the intensity of the light source. However, more than 60% of the proteins cannot be crystallized and thus X-ray-ed yet, which hinders progress in the area of structural genomics (Altarelli et al. 2006). Synchrotrons cannot provide the photon flux required for single object imaging. At the same time, their pulse duration of typically 100 ps is thousands of times larger than the time scale of atomic motion, such that dynamic information cannot be obtained.

These shortcomings will be removed by the upcoming free electron lasers. They will provide X-ray radiation with laser properties at 0.1 nm wavelength, with pulse durations in the femtosecond down to attosecond range (Feldhaus et al. 2005; Saldin et al. 2004a,b; Zholents and Fawley 2004) and intensities up to 1×10^{18} W/cm^2 (Altarelli et al. 2006) or 10^{12} photons/pulse. They will be able to resolve the pathways of chemical reactions or structural transformations during non-equilibrium processes on the time scale of atomic motion and with atomic resolution in space, as sketched in Figure 1.1.

By providing the photon flux to enable single object imaging, the FELs uncover a knowledge gap namely, the interaction of intense high frequency laser radiation with matter. It is this gap where the current work tries to make a contribution by also employing a second type of radiation, attosecond XUV laser pulses, as a probe. Connecting to experiments performed during the first stage of the FEL in Hamburg (Wabnitz et al. 2002), which lased 2001 in the vacuum ultra-violet (VUV) regime at 98 nm (12.65 eV) (Ayvazyan et al. 2002a,b), we will move to higher frequency 150 eV (8 nm) based on a new interaction model which puts emphasis on screening effects. After comparison to more recent experimental data, a pump-probe scheme will be

presented, where attosecond pulses in the extreme ultra-violet (XUV) will be used to gain insight into the incoherent transient dynamics of a rare-gas cluster during the interaction with the VUV FEL pulse. This slow-pump fast-probe scheme will be advanced to a fast-pump fast-probe setup, which will create and probe a nano-plasma far for equilibrium showing strongly-coupled behavior, as observed previously with much larger ultra-cold neutral micro-plasmas (Kulin et al. 2000; Pohl et al. 2005).
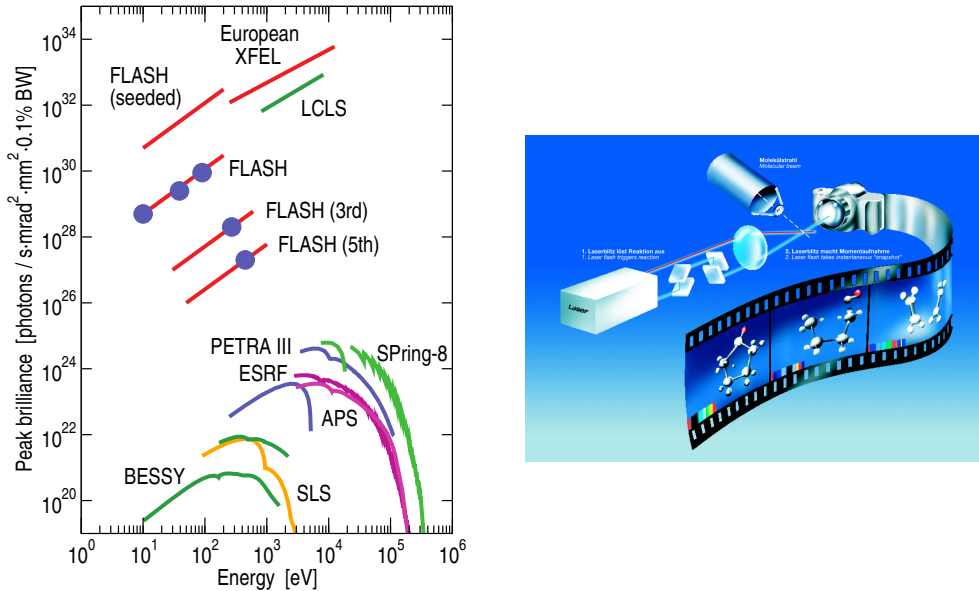

Figure 1.1: The peak brilliance of future and existent FEL facilities compared to the latest-generation synchrotron radiation sources around the world (left, from Ackermann et al. (2007)). FELs will be able to follow time-dependent structural transformations and produce *molecular movies* (right, from XFEL (2008)).

Atomic clusters are ideal objects for studying matter properties. They can be generated in a wide size range (Haberland et al. 1994; Hagena and Obert 1972), from less than ten atoms up to millions, allowing thus to study the transition from the atom to the solid phase. The transition is by far not linear, as experiments of laser-cluster interaction in the infrared domain have shown. Clusters can absorb energy much more efficiently than atoms or solids, leading to spectacular observations, ranging from ultra-fast ions in the MeV range or very fast electrons in the keV domain, to the generation of coherent and incoherent X-ray radiation and culminating with nuclear fusion, where fast neutrons are produced (Ditmire et al. 1999). These phenomena are all rooted in the reduced size of the clusters, which enables new mechanisms of absorption, must of them due to the large surface to volume ratio. Moreover, energy is kept within a well defined volume and fully redistributed among the particles that have absorbed it, unlike in the solid phase, where it dissipates into the lattice.

Attosecond XUV pulses, which will be used in this work to probe the transient cluster dynamics, are filtered from the high harmonics produced when a strong IR laser is focused into a dilute gas (Agostini and DiMauro 2004). Isolated pulses as short as 170 as in the extreme-ultraviolet (Goulielmakis et al. 2007; Schultze et al.

2007) have been achieved. They have been used in pump-probe setups to initiate an excitation, which was probed with the IR field that originally created the XUV pulse in a method called streaking (Kienberger et al. 2004). The momentum and time distribution of an electron wave packet could thus be recorded as it emerges into continuum. Created via photo-ionization, the wave packet allowed the direct measurement of the intensity profile of the attosecond pulse (Hentschel et al. 2001), as well as direct measurement of light oscillations (Goulielmakis et al. 2004). When created via the relaxation of a core hole, it allowed the direct measurement of an Auger-decay (Drescher et al. 2002).

In these experiments, attosecond pulses have only been used to initiate coherent single- to few electron dynamics, whose time structure could have also been determined without an additional probe pulse. Full measurement in the energy domain at the end of the experiment would have returned the same result by a simple Fourier transform, due to the canonical conjugation of time and energy. The dissipative nature of cluster dynamics, where the absorbed energy is quickly redistributed across many degrees of freedom, destroys coherence and makes it impossible to retrieve information about transient states of the system at later times, when the particles have arrived at the detector. For this reason, a pump-probe scheme will be presented, where attosecond pulses will be used not as fast δ-like excitation, but as a fast, instantaneous probe of the internal, incoherent dynamics of the cluster.

Chapter 2 familiarizes the reader with current topics of laser-cluster interaction starting from the basic unit, the atom. Atomic single- and multi-photon, as well as tunnel and field-ionization are reviewed. Then, representative experimental and theoretical findings of laser-cluster interaction will are summarized, with emphasis on their cooperative (read local) or collective character.

Chapter 3 presents the experiment that has sparked this work namely, the surprisingly high energy absorption of rare-gas clusters when exposed to VUV radiation from a free electron laser (Wabnitz et al. 2002). Because the free electron laser in Hamburg (FLASH) was and still is the only FEL actually working in the high frequency range, this experiment will be referred quite often to as "the Hamburg experiment". provide beam time.

Chapter 4 presents a hybrid quantum-classical model for laser cluster interaction with emphasis on plasma effects. Based on the time scale set by localized electrons, a coarse-grained dynamics is introduced, that performs the interpolation between the rate based, quantum-mechanical approach of photo-ionization and the deterministic, classical propagation of the ionized particles which, in a cluster, modify the way bound electrons can absorb photons.

The model is then illustrated in Chapter 5 at the adiabatic excitation of an Ar_{147} cluster by VUV radiation similar to that of the Hamburg experiment. Adiabaticity refers in this context to the very long duration of the laser pulse compared to the time scale of electron dynamics, such that the electron plasma can be considered in equilibrium at any time during the excitation. A comparison to more recent experimental results at 32 nm is also made.

Chapter 6 introduces a pump-probe scheme, aimed for experimental proof, or

distinction between existent theoretical models for the Hamburg experiment. An attosecond XUV laser pulse photo-ionizes valence electrons of the cluster ions, whose charge is imprinted on the kinetic energy of the XUV photo-electrons at the detector.

Chapter 7 analyzes the case where both the pump and the probe pulse are filtered from the high harmonics. The pump pulse is much shorter such that the excitation becomes diabatic, allowing for competition between ionization and relaxation of the nano-plasma. It is shown that the limit of ultra-short excitation can be used to initiate strongly-coupled plasma behavior with as few as 55 electrons, otherwise observed in extended ultra-cold neutral plasma with millions of particles.

The hybrid quantum-classical interaction model, the attosecond pump-probe scheme and the diabatic excitation scheme have been published as Georgescu et al. (2007a), Georgescu et al. (2007b) and Saalmann et al. (2008), respectively.

Chapter 2

Interaction of light with atoms and clusters

Optical properties of atomic clusters have been used since ancient times by the Romans for their glass work. They poured gold salts into the glass mixture to obtain gold nano-particles of various sizes, which they used to change the color of the glass in a wide range from light violet to deep red. The Lycurgus cup, now exposed at the British Museum in London, is considered one of their masterpieces. When illuminated from inside it shows the typical red color, but is green when illuminated from outside, due to the scattering spectrum of the nano-particles. These properties also fascinated Mie, who was the first to wonder about the properties of gold nano-particles if their size could be reduced even more, down to one atom (Mie 1908). Such studies were possible only in the past 20 years with the technological advances in creating size controlled cluster beams in the range from less then ten to millions of atoms. They proved this way to be more than just a liner transition between the atom and the bulk. The complex interplay of high, solid-phase local density, quantum-size effects and large surface to volume ratio have turned them into completely new materials with unique chemical, optical, magnetic and (di)electric properties.

This chapter will summarize optical absorption mechanisms in clusters starting from the atom, the basic unit, with its main photo-ionization mechanisms: single- and multi-photon, tunnel- and field ionization. Then, in the second section, we will move to larger systems, presenting the basic experimental and theoretical findings of the past years, grouped in collective effects, induced by the finite size, and cooperative effects, caused by the high local density.

2.1 Ionization of an isolated atom

First observations of the interaction of light with matter date back to 1839, when Alexander E. Becquerel discovered the photo-voltaic effect (Becquerel 1839). He dipped two electrodes in an electrolyte solution and was able to measure a current when one of them was illuminated by sun light, which he correctly attributed to a chemical reaction (Williams 1960). Its most notable application nowadays is found

in solar cells.

The photoelectric effect was discovered in 1877 by Heinrich Hertz (Hertz 1887), accidentally of course, while looking for resonance phenomena between two *electric oscillations*, electromagnetic radiation generated by electrical discharge between two electrodes. He observed that the strength of the discharge could be amplified with UV-light, but was not very much interested. The investigations were carried on by his student, Wilhelm Hallwachs, who also discovered that negatively charged bodies discharge when exposed to UV light (Hallwachs 1888a), while neutral metallic surfaces acquire positive charge (Hallwachs 1888b). The effect carried his name for a long time.

The explanation was delivered 1905 by Einstein (Einstein 1905). Starting from Wien's law of black body radiation, he studied the entropy of low density radiation within Boltzmann's statistical formulation of thermodynamics and concluded

> ...that: Monochromatic radiation of low density (within the range of validity of Wien's radiation formula) behaves thermodynamically as though it consisted of a number of independent energy quanta of magnitude $R\beta\nu/N$.

Assuming that only one energy quanta interacts with an electron at a given time and that it transfers its whole energy to the electron he wrote down

$$\frac{1}{2}mv^2 = \Pi e = h\nu - P\,, \tag{2.1}$$

where Π is the stopping potential, equal to the kinetic energy of the particles and P is the work necessary to get the electron out of the metal. Equation (2.1) was supported by Lenard's extensive investigations, which showed that the velocity of the emitted particles was dependent on the color of the incoming radiation, but independent of its intensity (Lenard 1902). This was in contrast to standard understanding about resonances, which due to the successful Maxwellian electrodynamics were supposed to lie at the origin of the photo-electric effect.

Although the hypothesis of energy quanta had already been introduced by Planck in 1901 (Planck 1901) and seemed to have experimental support in Lenard's findings, it faced wide criticism. Most of it from Planck himself, who, as many others, was not yet prepared to drop the Maxwellian theory of electrodynamics. Final experimental proof of Eq. (2.1) came 1916 from Millikan, who held Lenard's investigation for insufficient to fully confirm Eq. (2.1) and actually wanted to prove Einstein wrong (Millikan 1916).

The process in which the electron absorbs the energy from a photon was explained another ten years later within the new quantum mechanics. Schrödinger solved the *wave equations* (Schrödinger 1926)

$$i\hbar\frac{\partial\psi}{\partial t} = -\frac{\hbar^2}{2}\Delta\psi + V(r)\psi - \mathbf{E}\cos(2\pi\nu t)\sum_i e_i\mathbf{r}_i\psi \tag{2.2}$$

for a classical electromagnetic field in first order perturbation theory and asserted the absorption of energy from an electromagnetic wave to be indeed a resonance. Not one

in the common sense, where the frequency of the driving matches an eigenfrequency, but one where it matches a difference of eigenfrequencies that is, eigenenergies. The approach emphasizes the wave-like behavior of electromagnetic radiation. Dirac emphasized the particle-like behavior (Dirac 1927) and was thus able to describe not only stimulated emission and absorption of light quanta, but also their spontaneous emission.

In the following we consider the Schrödinger equation

$$i\hbar\frac{\partial}{\partial t}|\,\Psi(t)\rangle = H|\,\Psi(t)\rangle \tag{2.3}$$

with the single electron Hamiltonian

$$H = \frac{\mathbf{p}^2}{2} - \frac{Z}{r} - \mathbf{r}\mathbf{E}(t) \tag{2.4}$$

partitioned as

$$H = H^0 + V(t), \quad \text{with } H^0 = \frac{\mathbf{p}^2}{2} - \frac{Z}{r} \text{ and } V(t) = -\mathbf{r}\mathbf{E}(t), \tag{2.5}$$

to describe the interaction of an atom with electromagnetic radiation. The eigenstates φ_n and eigenvalues E_n of the Hamiltonian H^0 of the field-free atom are known

$$|\,\varphi_n(t)\rangle = e^{-\frac{i}{\hbar}E_n t}|\,\varphi_n\rangle. \tag{2.6}$$

The single-particle formulation has been chosen for simplicity. The following considerations are valid *ad literam* for many-electron atoms as well, but the ionization process itself involves a single active electron.

Starting in an eigenstate $|\,\varphi_i\rangle$ at $t = 0$, one propagates formally the Schrödinger equation in Green's function's formalism

$$|\,\Psi(t)\rangle = |\,\varphi_i(t)\rangle + \int_0^\infty G_0(t,t')V(t')|\,\Psi(t)\rangle \mathrm{d}t', \tag{2.7}$$

where and $G_0(t,t')$ is the Green's function of the unperturbed system

$$\left(i\hbar\frac{\partial}{\partial t} - H^0\right)G_0(t,t') = \delta(t-t') \tag{2.8}$$

given by

$$G_0(t,t') = \frac{1}{i\hbar}\Theta(t-t')\sum_n |\,\varphi_n(t)\rangle\langle\varphi_n(t')|. \tag{2.9}$$

The integral (2.7) was extended to infinity because $G_0(t,t')$ also takes care of time ordering. Recursive application of Eq. (2.7) onto itself leads to the infinite series

$$\begin{aligned}
|\,\Psi(t)\rangle = &|\,\varphi_i(t)\rangle + \int_0^\infty G_0(t,t_1)V(t_1)|\,\varphi_i(t_1)\rangle\,\mathrm{d}t_1 \\
&+ \iint_0^\infty G_0(t,t_1)V(t_1)\,G_0(t_1,t_2)V(t_2)|\,\varphi_i(t_2)\rangle\,\mathrm{d}t_1\mathrm{d}t_2 \\
&+ \int\cdots\int_0^\infty G_0(t,t_1)V(t_1)\cdots G_0(t_{n-1},t_n)V(t_n)|\,\varphi_i(t_n)\rangle\,\mathrm{d}t_1\cdots\mathrm{d}t_n \\
&+ \ldots\,.
\end{aligned} \tag{2.10}$$

The number of laser "kicks" is equal to the number of photons involved. In first order perturbation theory only the first term of the series (2.10) is retained because the light field is much weaker than the attraction of the nucleus. Projection of $\Psi(t)$ onto an eigenstate $\varphi_f(t)$ of H_i^0 selects a single term from the summation in Eq. (2.9) and yields the probability to find the atom in that state at the given time t

$$w_{i \to f}(t) = |\langle \varphi_f(t) \,|\, \Psi(t)\rangle|^2 = \frac{1}{\hbar^2} \left| \int_0^t \langle \varphi_f|V(t_1)|\varphi_i\rangle e^{\frac{i}{\hbar}(E_f - E_i)t_1} \, \mathrm{d}t_1 \right|^2 . \tag{2.11}$$

The time integration can be performed analytically for $V(t) = -\mathbf{r}\hat{\epsilon}_0 \mathcal{E} \cos \omega t$ and an average transition rate is obtained, which can be reduced to a cross-section if the photon current density is eliminated

$$\sigma_{i \to f} = 4\pi^2 \alpha \hbar \omega_\lambda |\langle \varphi_f|\hat{\epsilon}_0 \mathbf{r}|\varphi_i\rangle|^2 \rho(E_f) . \tag{2.12}$$

$\hat{\epsilon}_0$ is the polarization of the field and $\mathcal{E}$ its amplitude; $e\mathbf{r}$ is the electric dipole operator and $\rho(E_f)$ is the final density of states. $\rho(E)$ is a δ-function $\rho(E_f) = \delta(E_f - E_i \pm \hbar\omega)$ if E_f is a discrete level or $\rho(E_f) = 1$ otherwise, provided that $|\varphi_f\rangle$ are also energy normalized

$$\int_{\varepsilon - \Delta\varepsilon}^{\varepsilon + \Delta\varepsilon} \langle \varphi_\varepsilon \,|\, \varphi_{\varepsilon'}\rangle \mathrm{d}\varepsilon' = 1 . \tag{2.13}$$

With increasing field strength there are enough photons in the vicinity of an atom that the higher order terms of Eq. (2.10) become significant. First evaluation of the second order term was presented in 1931 by Maria Göppert-Mayer in her dissertation on *Elementarakte mit zwei Quantensprüngen* (Göppert-Mayer 1931). She studied processes such as spontaneous and stimulated emission of two photons, of equal or different frequency, as well as the emission of a photon due to an inelastic collision.

Experimental observation of multi-photon absorption came much later with the invention of the laser (Maiman 1960, 1967; Schawlow and Townes 1958). The rapid development of laser technology provided soon power densities sufficient for absorption of several tens of photons, even more then the minimum required for ionization in process known as 'above-threshold ionization' (ATI) (Agostini et al. 1979). Even stronger laser fields can bend the nuclear potential so strongly, that the bound electron can tunnel out or even be ionized instantly.

Figure 2.1 presents an overview of ionization processes in atoms. The field intensity increases from left to right, the photon energy from right to left. For weak power density, only single photons of high energy can be absorbed. The multi-photon terms gain significance with increasing laser intensity, such that several photons can contribute to ionize one electron in a single act. If the field is even stronger, it can bend the Coulomb potential of the nucleus so strongly that the electron can tunnel out. It is important though, that the frequency of the laser be less than the revolution period of the electron, such that the electron can make several attempts to tunnel through the barrier. Finally, for even stronger laser fields, when

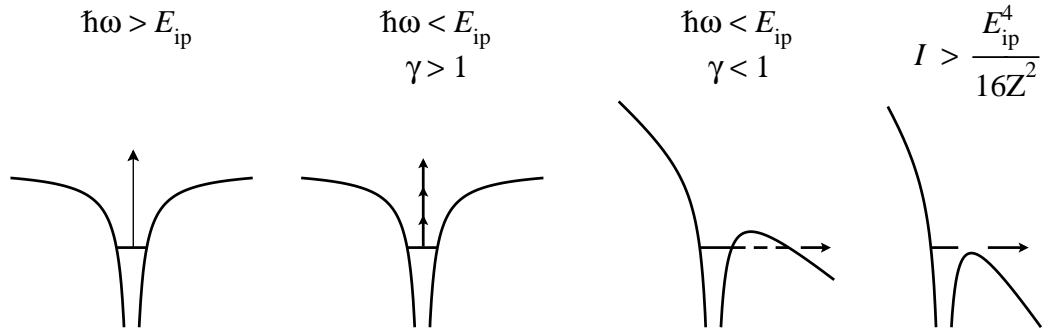$$I > \frac{E_{ip}^4}{16Z^2} \tag{2.14}$$

Figure 2.1: Atomic ionization mechanisms in a light field. From left to right: single-photon, multi-photon, tunnel and field ionization.

the electron is all of a sudden in the continuum. The condition is also known as the Bethe rule (Bethe and Edwin 1977).

The transition between the multi-photon and the tunneling regime is indicated by the Keldysh parameter (Keldysh 1964)

$$\gamma = \omega\tau = \sqrt{\frac{E_{\text{ip}}}{2U_p}}\,, \tag{2.15}$$

which compares the tunneling time τ to the period $2\pi/\omega$ of the light field. E_{ip} is the ionization potential of the electron and

$$U_{\text{p}} = \frac{\mathcal{E}^2}{4\omega^2} \tag{2.16}$$

is the ponderomotive energy, the average kinetic energy of a free electron driven by an oscillating electric field of amplitude $\mathcal{E}$ and frequency ω. The tunneling time τ is defined as the time needed by a classical electron of velocity $\sqrt{2E_{\text{ip}}}$ to travel a distance equal to the width of the barrier.

For $\gamma \ll 1$ the barrier is almost static and the electron can tunnel through. If $\gamma \gg 1$, the field is too fast. The Coulomb potential is shaken quickly back and forth, such that the electron is excited vertically by absorption of one or more photons. In-between both phenomena coexist. Tunneling persists, but is no longer adiabatic. The rapid field oscillations heat up the electron while still being underneath the barrier, initiating the transition to vertical ionization (Ivanov et al. 2005) (see also figures 3 and 4 therein). Recent time-resolved experiments with sub-femtosecond resolution have demonstrated electron tunneling out at field maxima for $\gamma \sim 3$ (Uiberacker et al. 2007).

Multi-photon ionization (MPI) rates can be obtained from Eq. (2.10) by evaluating the lowest order terms. The results can overestimate the rate by a few orders of magnitude (Potvliege and Shakeshaft 1989), but reproduce the angular distributions quite well (Kracke et al. 1988).

S-matrix theories can provide an *ab initio* non-perturbative approach for strong field problems. One such theory is IMST (intense-field many-body S-matrix theory)

(Becker and Faisal 2005), which accounts simultaneously and systematically for the different reference Hamiltonians (or dominant interactions) in the initial and final states, as well as intermediate (virtual) Hamiltonians accounting for internal rearrangement in the many-electron system during the interaction with the laser.

One propagates the Schrödinger equation (2.3) as well

$$
|\Psi(t)\rangle = |\varphi_{\mathrm{i}}(t)\rangle + \int_{t_i}^{t_f} G(t,t')V(t')\varphi_{\mathrm{i}}(t')\mathrm{d}t'\,, \tag{2.17}
$$

but now with the total Green's function $G(t,t')$ of the full Hamiltonian $H(t)$

$$
\left(i\hbar\frac{\partial}{\partial t} - H(t)\right)G(t,t') = \delta(t-t') \tag{2.18}
$$

The initial state of the system is dominated by the interaction with the atom, whereas the final one is dominated by the laser and the atom is rather a weak perturbation, hence a second partitioning $H(t) = H_{\mathrm{f}}^0 + V_{\mathrm{f}}(t)$ is introduced

$$
H_{\mathrm{f}}^0 = \frac{\mathbf{p}^2}{2} - \mathbf{r}\hat{\epsilon}_0\mathcal{E}\cos\omega t\,, \quad V_{\mathrm{f}} = -\frac{Z}{r}\,, \tag{2.19}
$$

which groups the dominant terms into the reference Hamiltonian H_{f}^0. The total Green's function $G(t,t')$ is expanded in terms of the Green's function $G_{\mathrm{f}}(t,t')$ of electron-laser system

$$
G(t,t') = G_{\mathrm{f}}(t,t') + \int_{t_i}^{t_f} G_{\mathrm{f}}(t,t_1)V_{\mathrm{f}}(t_1)G(t_1,t')\mathrm{d}t_1 \tag{2.20}
$$

and inserted back into Eq. (2.17) to obtain

$$
\begin{aligned}
\Psi(t) = \varphi_{\mathrm{i}}(t) &+ \int_{t_i}^{t_f} G_{\mathrm{f}}(t,t_1)V(t_1)\varphi_{\mathrm{i}}(t_1)\,\mathrm{d}t_1 \\
&+ \iint_{t_i}^{t_f} G_{\mathrm{f}}(t,t_2)V_{\mathrm{f}}(t_2)G(t_2,t_1)V(t_1)\varphi_{\mathrm{i}}(t_1)\,\mathrm{d}t_1\mathrm{d}t_2\,.
\end{aligned} \tag{2.21}
$$

The scheme can be extended to higher *interaction* orders by expanding the total Green's function $G(t,t')$ in the second term of Eq. (2.21) with respect to other intermediate partitionings of the total Hamiltonian $H(t)$. Even the first term contains all orders with respect to the number of photons involved (Becker and Faisal 2005).

The eigenstates of H_{f} are the well known Volkov wave functions. The first integral of Eq. (2.21) is thus equivalent to the Keldysh approximation (Keldysh 1964), where the electron is propagated until t_1 in his bound state, is kicked by the laser and propagates further on a Volkov state in the continuum. For a linearly polarized field, the Keldysh-Faisal-Reiss (KFR) approximation (Faisal 1973; Keldysh 1964; Reiss 1980) leads to the ionization rate

$$
\Gamma_{\mathrm{KFR}}^+ = 2\pi\sum_{N=N_0}^{\infty} k_N(U_{\mathrm{p}} - N\omega)^2\int\mathrm{d}\hat{\mathbf{k}}_N J_N^2\big(|k_N|x_{\mathrm{p}}, \frac{U_{\mathrm{p}}}{2\omega}, 0\big)|\langle\varphi_{k_N}(\mathbf{r})\,|\,\varphi_i(\mathbf{r})\rangle|^2\,, \quad (2.22)
$$

where J_N is the generalized Bessel function of three arguments (Becker and Faisal 1994; Reiss 1980) and N_0 the minimum number of photons required for ionization. $U_{\rm p}$ is the ponderomotive energy, $x_{\rm p}$ is the associated ponderomotive amplitude $x_{\rm p} = \mathcal{E}/\omega^2$ of the oscillatory motion. The general ionization rate for elliptic polarization can found in Ref. (Becker and Faisal 2005). The KFR approximation, though only first order in the interaction, contains all photon orders already.

If the expansion of $G(t, t')$ with respect to the final reference Hamiltonian $H_{\rm f}^0$ is applied again in Eq. (2.21), the second order term will correspond to the re-collision of the electron with the ion

$$\iint_{t_i}^{t_f} G_{\rm f}(t, t_2) V_{\rm f}(t_2) G_{\rm f}(t_2, t_1) V_{\rm i}(t_1) \varphi_{\rm i}(t_1) \, {\rm d}t_1 {\rm d}t_2 \,. \tag{2.23}$$

The electron propagates on the atomic bound state, is kicked by the laser, propagates on a Volkov state where it collides against the nucleus and propagates off on a Volkov state again. Appropriate formulation of the initial, intermediate and final Hamiltonians can then describe processes such as high-harmonic generation or double-ionization (Becker and Faisal 2005).

S-matrix theories provide a clear picture of the basic mechanisms involved in ionization and deliver good qualitative results. Quantitatively, they underestimate by more than one order of magnitude because the long range Coulomb interaction is not included in the final state. Coulomb corrected KFR rates, as proposed by Becker *et al.*, are then able to reproduce the results of Floquet calculations, direct numerical 3D time-dependent solutions of the Schrödinger equation and, most important, experiments (Becker et al. 2001)

$$\Gamma_{\rm ion}^+ = \left(\frac{2k_B E_B}{\mathcal{E}} \right)^{2Z/k_B} \Gamma_{\rm KFR}^+ \,. \tag{2.24}$$

3D time-dependent propagation of Schrödinger's equation and Floquet theories provide indeed exact alternatives, but the computational requirements increase exponentially with the number of electrons. However, it is more difficult to single out ionization mechanisms due to the large amount of data.

2.2 Cluster ionization: cooperative and collective effects

Optical excitation of atomic clusters has been the main instrument for investigating their structural and dynamical properties. Photo-electron spectroscopy reveals the ground state density of states, photo-absorption experiments map out the excitation spectrum. Optical excitation has been employed for initiating vibronic excitations, for studying fragmentation, evaporation or dissociation.

We will focus on those experiments dealing with energy absorption from intense electromagnetic radiation. Clusters have proved to absorb energy much more efficiently than atoms or solids, leading to spectacular observations such as MeV fast

ions or even nuclear fusion. This efficiency is mostly rooted in their reduced size, which enables new absorption mechanisms and redistributes the energy only among the particles that have absorbed it. Dissipation into the lattice, as in the solid phase, is here absent.

The first part of this section addresses the main experimental observables. The second part will present those experimental and theoretical results which underline cooperative behavior, a consequence of the high density. The third and last part will then summarize collective effects. A review of laser-cluster interaction has been compiled in much more detail by Saalmann *et al.*(Saalmann et al. 2006).

It is useful to consider the interaction with intense laser fields as a three step process, sketched in Figure 2.2. Clusters have been reported to disintegrate fully already at power densities of 1×10^{12} W/cm^2 for 98 nm radiation (Laarmann et al. 2004). Beyond this value, energy absorption is dominated by plasma effects, which renders the electronic structure of the cluster irrelevant. When the leading edge of the pulse hits the cluster, the atoms interact with the light field as if they were isolated. The charge of the cluster increases gradually, up to a point where it traps the further photo-electrons released by the light field from their mother atoms. The second step of the process starts now, the most complex of them all and where the most energy is absorbed. Complex cooperative and/or collective mechanisms resulting from the high density of the cluster and its finite size are now in action. The third step marks the relaxation of the system after the laser has been turned off. The cluster expands and the energy is redistributed among the various degree of freedom.
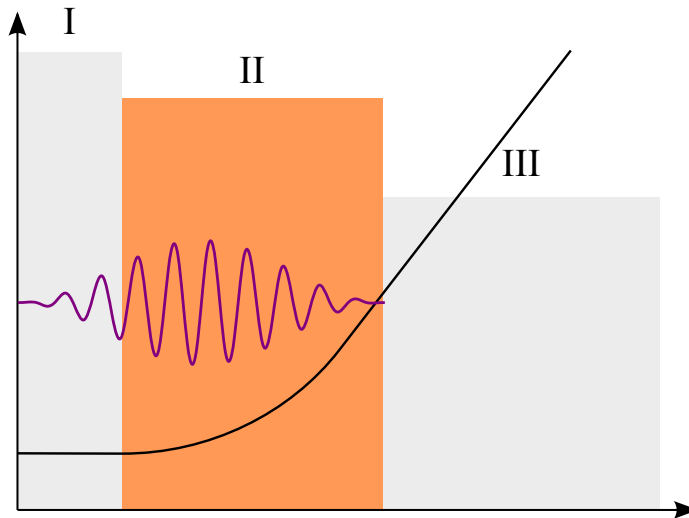

Figure 2.2: Three-step model of the laser cluster interaction. I: neutral cluster, atoms interact with the field as if independent. II: atoms become aware of the neighboring ions and electrons, complex, cooperative and collective phenomena; III: relaxation, energy is redistributed among the various degrees of freedom.

Last and Jortner (1999) named those electrons trapped inside the cluster inner-ionized, or quasi-free. They are delocalized with respect to their mother atoms, but still localized with respect to the cluster due to their negative total energy. They

can acquire positive total energy by further absorption from the laser field or simply collisions with other electrons. In this case they can leave the cluster and are called outer-ionized. The distinction between inner- and outer-ionized electrons will prove essential when analyzing energy absorption mechanisms. Only inner-ionized electrons can further absorb energy from the laser field.

Although a plasma has formed, the cluster is transparent to electromagnetic radiation because it is much smaller than the wavelength of the field. The dipole approximation holds for the cluster as a whole. Propagation effects, such as the skin depth encountered with extended plasmas are not present here.

λ	$\hbar\omega$	$I =$	10^{14} W/cm^2	10^{16} W/cm^2	10^{18} W/cm^2
780 nm	1.5 eV	$\gamma =$	1.17	0.117	0.012
		$U_\mathrm{p} =$	5.67 eV	567 eV	56.7 keV
		$x_\mathrm{p} =$	8.28 Å	82.8 Å	828 Å
98 nm	12.65 eV	$\gamma =$	9.37	0.937	0.094
		$U_\mathrm{p} =$	89 meV	8.9 eV	890 eV
		$x_\mathrm{p} =$	0.466 Å	4.66 Å	46.6 Å
3.5 nm	354.23 eV	$\gamma =$	262	26.2	2.62
		$U_\mathrm{p} =$	0.1 meV	11.4 meV	1.14 eV
		$x_\mathrm{p} =$	0.0006 Å	0.006 Å	0.06 Å

Table 2.1: Keldysh parameter γ, ponderomotive amplitude x_p and energy U_p for laser systems typically employed in experiments with atomic clusters. For γ, the ionization potential $E_\mathrm{ip} = 15.76$ eV of Ar has been used.

The strength of the electron-light coupling is described by the ponderomotive amplitude x_p and energy U_p

$$x_\mathrm{p} = \frac{\mathcal{E}}{\omega^2}, \quad U_\mathrm{p} = \frac{\mathcal{E}^2}{4\omega^2}. \tag{2.25}$$

They describe the amplitude and average kinetic energy of the oscillations performed by a free classical electron driven by an electromagnetic field of amplitude $\mathcal{E}$ and frequency ω. When bound inside an atom, the coupling is additionally described by the Keldysh parameter γ (2.15) which characterizes the photon absorption regime.

Table 2.2 summarizes γ, x_p and U_p for laser systems typically used to study atomic clusters, such as Ti:Sa and FELs. Together they characterize energy absorption as a whole: at atomic level in the first step, as well as at cluster level in the second one. The infrared (IR) regime is dominated by multi-photon or tunnel-ionization. The ponderomotive amplitude x_p exceeds the size of the cluster and U_p reaches in the keV domain. Once ionized, the electrons are dragged forth and back through the whole cluster reaching energies on the order of U_p or larger. With X-rays, both x_p and U_p are negligible and single-photon absorption takes over. In-between, in the VUV range, x_p is small, but not negligible and both multi-photon and single-photon absorption are possible.

2.2.1 Experimental observables

Typical observables are the charge distribution of the ions, as the well as the velocities of the ions and electrons. Highly charged ions (Pt^{20+} (Köller et al. 1999), Xe^{20+} und Kr^{18+} (Snyder et al. 1996), Xe^{8+} (Wabnitz et al. 2002)) have been detected, which can be accelerated up to 1 MeV in the Coulomb explosion (Ditmire et al. 1997b). Much lighter, the fastest electrons reach only 3 keV (Ditmire et al. 1998). The electrons trapped inside the cluster can form a very hot plasma, which will emit continuous bremsstrahlung in the X-ray domain. Electron impact or multi-photon absorption can create core whole excitations in the ions, which then relax by emission of characteristic X-rays (Adoui et al. 2003; Deiss et al. 2006; Lamour et al. 2005; Schroeder et al. 1998), showing transient ionization states of up to Xe^{44+}(McPherson et al. 1994).

Alternatively, one can directly measure the amount of absorbed energy by measuring the intensity of the laser beam after the interaction region (Ditmire et al. 1997a). The method presents the advantage that the energy of very slow electrons and, most important, neutral atoms can be measured because they would otherwise escape undetected. Efficiency beyond 90% (Schroeder et al. 1998) or even $> 95\%$ has been observed (Ditmire et al. 1997a).

Several groups have detected neutrons as products of nuclear fusion from collisions of very fast ions coming from different clusters (Ditmire et al. 1999; Grillon et al. 2002; Madison et al. 2004; Zweiback et al. 2000). Ditmire et al. (1999) have exposed D_2 clusters sizing roughly 50 Å to short, $T = 35$ fs, intense $I = 2 \times 10^{16}$ W/cm^2 laser pulses at $\lambda = 820$ nm and placed neutron detectors at distances of 1, 2.5 and 3.2 m from the interaction region. They allowed them to measure the velocity of the neutrons and, as expected, 2.45 MeV fast neutrons characteristic for the nuclear reaction

$$D + D \rightarrow He^3 + n \tag{2.26}$$

were detected. The equivalent yield of 10^5 neutrons per joule of laser energy was comparable to the efficiency of large-scale laser-driven fusion experiments such as the NOVA laser of the LLNL, with as much as 30 kJ of laser energy and repetition rate of one shot per hour (Dittrich et al. 1994).

2.2.2 Cooperative effects

They could also be called proximity effects. Due to the high density, the ions can cooperate to absorb more photons from the laser field.

The simplest cluster is a diatomic molecule. Strong-field ionization of diatomic molecules has shown enhancement of the ionization rate when they are stretched beyond their equilibrium inter-nuclear separation. The enhancement factor can reach several orders of magnitude over the ionization rates at smaller or larger distances (Boyer et al. 1989; Codling et al. 1989; Frasinski et al. 1987; Seideman et al. 1995; Zuo and Bandrauk 1995) and is largely independent of the laser frequency. Fig. 2.3(left) shows calculated yields for H_2^+ (Zuo and Bandrauk 1995) in a linearly polarized field as a function of the inter-nuclear separation. The ionization yield is low at equilibrium

($R = 2$ Å) due to the large ionization potential $E_{\mathrm{ip}} = 30$ eV. The molecular ion behaves just like an atom. The yield increases with increasing inter-nuclear distance and peaks twice, first at 7 Å and then 10 Å. The ionization of atomic hydrogen is shown for reference with a small rectangle.

The enhanced ionization (EI) proved to be due to the combined action of the laser field and of the partner ion, as shown in Fig. 2.3(right). Together they can lower the internal barrier strongly and increase the chance of the electron to tunnel out into the continuum. Non-adiabaticity is here crucial. If the field changed adiabatically, the electron would tunnel through the internal barrier into the lower well, leaving the upper well empty when the field reaches the maximum. Ionization would only occur by tunneling through the external, higher and wider barrier. The non-adiabatic variation of the laser field keeps the upper level populated by up to 50% (Zuo and Bandrauk 1995), such that the electron can tunnel out. One may say that internal tunneling is suppressed by the non-adiabatically varying field. For larger separations the atomic limit is reached, as seen in Fig. 2.3(left). EI has also been observed with non-symmetric molecules (Kamta and Bandrauk 2007).
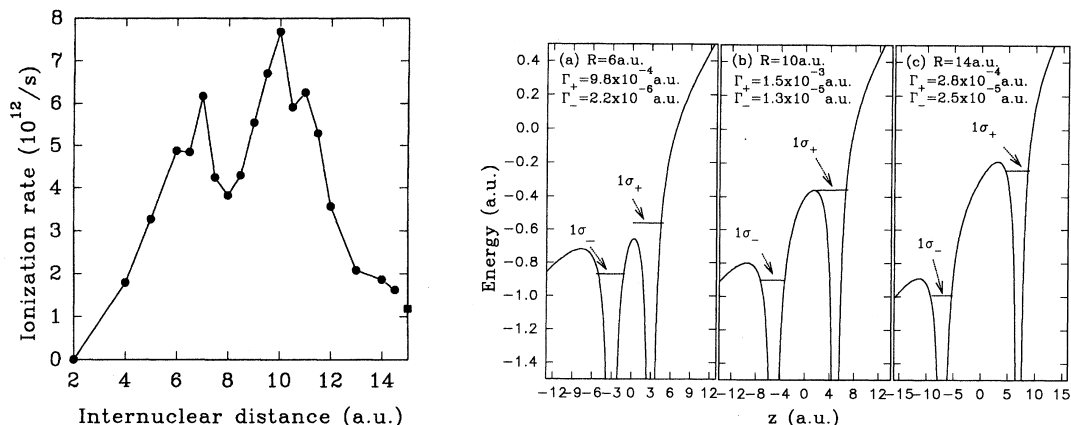

Figure 2.3: Left: ionization rate of the H_2^+ molecular ion in a linearly polarized $I = 10^{14}$ W/cm^2 and $\lambda = 1064$ nm laser field. Right: lowest two dc-field-induced levels of H_2^+, $1\sigma_+$ and $1\sigma_-$, in the effective potential $V_c(R) + E_0 z$. The strength of the dc field is $E_0 = 0.0533$ au ($I = 1 \times 10^{14}$ W/cm^2). From (Zuo and Bandrauk 1995).

EI has not yet been detected experimentally in clusters, but simulations have proved it to be very effective. Siedschlag and Rost (2003) investigated EI in Ne$_{16}$, Ar$_{16}$, Kr$_{16}$ and Xe$_{16}$ clusters . They found in all cases maximum ionization when the average inter-ionic distance reached $R^* = 1.2R_0$, where R_0 is the average inter-atomic distance at equilibrium. The enhancement did not vary significantly for the frequencies they have investigated, namely $\omega = 1.5$, 2 and 3 eV, nor with circularly polarized light. The latter would actually be expected due to the almost spherical symmetry of the clusters. With molecules, EI is suppressed when the light is polarized perpendicularly to the molecule (Bandrauk and Ruel 1999; Banerjee et al. 1999).

Because EI is mostly independent of the laser frequency, it should be possible to

distinguish from a plasmon resonance by varying the laser frequency. Such experiments have not yet been performed.

Higher laser frequency suppresses tunneling, as reflected by the higher Keldysh parameter in Table 2.2. Ionization enhancement occurs now due to inner-ionization. The lower potential barrier allows for single photon excitation of bound electrons into inner-ionized cluster states, as shown in Figure 2.4. This idea was suggested by Siedschlag and Rost (2004) to lie at the origin of the Hamburg experiment that will be described in Chapter 3. The process is very efficient, because the ionization potential of the rare-gas atoms increases linearly with the charge state. The inter-ionic barrier is also proportional to charge, such that, if the mechanism has worked once, it will work until a jump in the ionization potential occurs. This happens when a very strong bound orbital is reached, such as $4d$ in Xe or $2p$ in Ar. Until that point is reached, up to 8 electrons per atom will have been ionized forming a very dense, warm plasma. Driven by the laser field, the electrons perform small oscillations and absorb energy through inverse bremsstrahlung due to scattering at the highly charge ions. There is still no experimental evidence, but Chapter 6 will present how attosecond pulses could provide it.
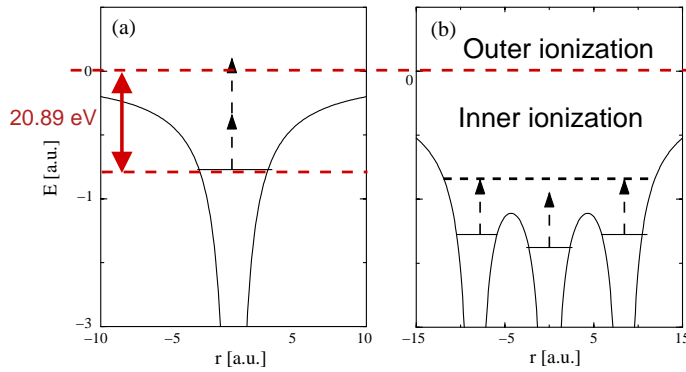

Figure 2.4: Inner-ionization in a cluster. The Hamburg experiment showed that two-photon ionization is much less probable with respect to single-photon absorption. This favors inner ionization, where electrons can be excited from atomic bound states into cluster states by absorption of a single photon. From (Siedschlag and Rost 2004).

Proximity can not only enhance ionization but also inhibit it. Saalmann and Rost (2002) have studied the ionization of Ar clusters with X-rays at 350 eV photon energy. Other than in the previous cases, the photon is absorbed here by a core electron. The remaining vacancy can be refilled with an electron from the valence orbital via Auger-decay, allowing thus for further photo-ionization. On the other hand, valence electrons can tunnel resonantly to a neighboring ion if the equivalent state is vacant there. This leads to an overall delocalization of valence electrons which decreases the refill rate of the core orbitals, preventing absorption of further X-ray photons.

Figure 2.5 compares the charging of two clusters, Ar_{13} and Ar_{55}, when intra-cluster tunneling was considered (dashed lines) or not (dot-dashed lines). Ionization is lower
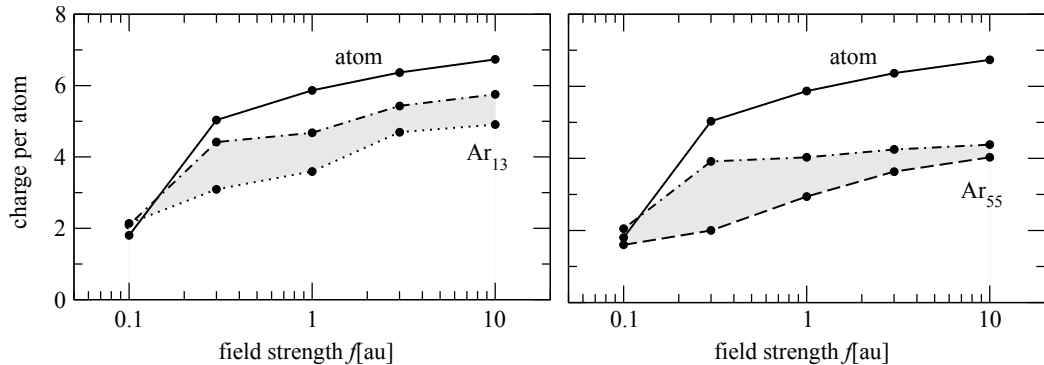
Figure 2.5: Average charge per atom for two Ar clusters, Ar_{13} and Ar_{55}, as a function of the intensity of the 100 fs, 350 eV laser pulses they have been exposed to. Intra-cluster tunneling was included (dashed lines) or not (dot-dashed lines). The continuous lines show the charging of the isolated Ar atom under the same laser parameters.

for the former. In both cases, further plasma heating is absent due to the very low ponderomotive amplitude x_p (see Table 2.2). The average charge of the cluster is thus less than that of the isolated atom due to space charge and recombination effects. In contrast, in the Hamburg experiment the small, but considerably higher x_p allowed for inverse bremsstrahlung which increased the average ionization above the atomic level.

2.2.3 Collective effects

Collective effects concern the motion of the electrons in the ionic potential. The surface plasmon frequency of an Ag_9 cluster is roughly 4.0 eV (Köller et al. 1999). Cluster expansion lowers the plasmon frequency until it matches the frequency of the IR laser, typically 1.5 eV. Experimentally, this moment of the expansion is reached either by increasing the length of the pulse, while also decreasing the intensity to keep the total energy constant (Köller et al. 1999; Zweiback et al. 1999), or by employing a second, probe pulse whose delay with respect to the first one can be varied (Döppner et al. 2006; Fennel et al. 2007). In the first case, shown on the left hand side of Fig. 2.6, an optimum pulse length was observed which maximized the observed charge states. In the second case, shown in Fig. 2.6 on the right, the delay could be adjusted to maximize the yield of specific charge states.

Zamith et al. made a more involved experiment (Zamith et al. 2004). They sent the laser beam through a pulse shaper and tried to maximize the yield of Xe^{q+}, $q \geq 11$ by using genetic algorithms. The optimal pulse proved to be a double pulse structure, with two identical 120 fs long pulses separated by 500 fs.

Saalmann and Rost (2003) have performed molecular dynamics (MD) simulations and analyzed the resonant behavior by comparison with a damped driven harmonic oscillator

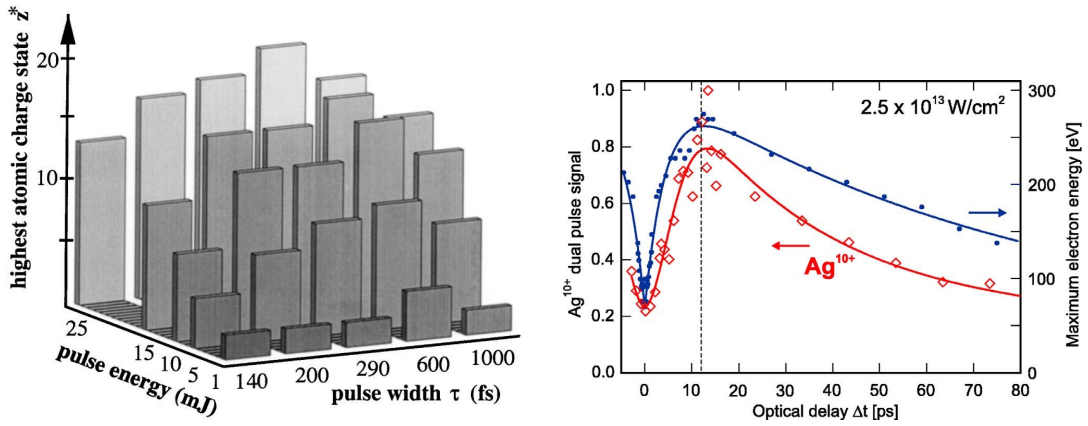$$\ddot{X}(t) + 2\Gamma_t \dot{X}(t) + \Omega_t^2 X(t) = F(t) \,, \tag{2.27}$$

Figure 2.6: Left: Maximum charge state observed with Pt clusters of $\langle N \rangle \approx 20$ atoms that have been exposed to IR $\lambda = 800$ nm pulses of variable energy and length (from (Köller et al. 1999)). Right: Comparison of the Ag^{10+} yield (diamonds, left axis) with the maximum kinetic energy E_{max} of the emitted electrons (dots, right axis) following dual pulse excitation of large Ag_N, $N \approx 22\,000$ with 100 fs, $\lambda = 800$ nm pulses at 2.5×10^{13} W/cm^2 intensity (from (Döppner et al. 2006)).
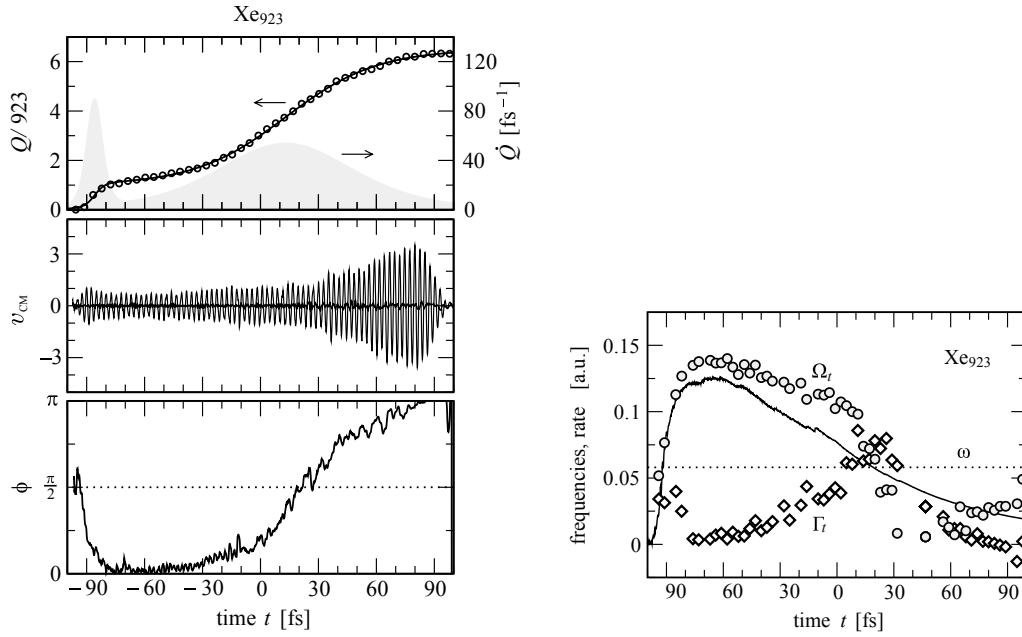

Figure 2.7: Left: Overall charging, CM velocity and CM phase of the electron cloud for a Xe_{923} cluster exposed to a 200 fs, 780 nm and $I = 9 \times 10^{14}$ W/cm^2 laser pulse. Right: eigenfrequency Ω_t and damping Γ_t according to Eq. (2.30); solid line: comparison with the surface plasmon frequency $\Omega_t = \sqrt{Q_{ion}(t)/R(t)^3}$. From (Saalmann and Rost 2003)

where $X(t) = A_t \cos(\omega t - \varphi_t)$ is the center-of-mass (CM) position of the electron cloud, $F(t) = F_0 \cos \omega t$ the driving force, Γ_t the damping and Ω_t the eigenfrequency. The index of Γ_t and Ω_t means that they vary slowly in time. The oscillation amplitude A_t and phase shift φ_t become

$$
\begin{aligned}
A_t &= \frac{F_0}{\sqrt{(\Omega_t^2 - \omega^2)^2 + (2\Gamma_t \omega)^2}} \\
\varphi_t &= \arctan \frac{2\Gamma_t \omega}{\Omega_t^2 - \omega^2}
\end{aligned}
\tag{2.28}
$$

and the cycle averaged energy transfer reads

$$
\langle \dot{E} \rangle = \langle \dot{E}_{\text{loss}} \rangle + \langle \dot{E}_{\text{gain}} \rangle = -\Gamma_t A_t^2 \omega^2 + \frac{1}{2} F_0 A_t \sin \varphi_t \, .
\tag{2.29}
$$

Obviously, maximum energy transfer occurs when $\varphi_t = \pi/2$, i.e. resonant behavior $\Omega_t = \omega$. Fig. 2.7(left) shows the total charging of a Xe_{923} cluster, together with the CM velocity and the CM phase of the electron cloud with respect to the field. The highest charging rate, as well as the sudden increase of the CM velocity coincide with the $\pi/2$ crossing of the phase. Inverting Eq. (2.28), one can obtain the eigenfrequency Ω_t and the damping Γ_t as function of the amplitude A_t and the phase φ_t, which are obtained directly from the simulation

$$
\begin{aligned}
\Omega_t^2 &= \omega^2 + \frac{F_0}{A_t} \cos \varphi_t \\
\Gamma_t &= \frac{F_0}{2 A_t \omega} \sin \varphi_t \, .
\end{aligned}
\tag{2.30}
$$

The right hand side of Fig. 2.7 shows Ω_t and Γ_t as function of time. They match the laser frequency almost simultaneously and stay relatively equal afterwards. The solid line is the surface plasmon frequency $\Omega_t = \sqrt{Q_{\text{ion}}(t)/R(t)^3}$.

Highly excited inner-ionized electrons whose mean free path compares to the cluster size can be accelerated in the polarization field of the cluster, as shown in Figure 2.8(b) (Fennel et al. 2007). If at a maximum of the plasmon polarization $\mathbf{p}$, the electron is situated at the cluster boundary and both $\mathbf{v}_e \cdot \mathbf{r}_e < 0$ and $s = \mathbf{v}_e \cdot \mathbf{p}$ hold, then it can be accelerated not only during its transit through the cluster, but also afterwards. The typical signature are sub-cycle bursts of very fast electrons, as depicted in Fig. 2.8(a). Both experiment and theoretical simulations found that the fastest electrons carry 100 times more energy than the ponderomotive energy. This is remarkable, since compelled by limitations of the theoretical model, the authors had to simulate Na clusters with a single active electron instead of Ag and the laser intensity was reduced by a factor of 10 to $I = 8 \times 10^{12}$ W/cm^2. The mechanism is particularly efficient if the laser is resonant to the surface plasmon, such that the authors have named it SPARC, surface-plasmon-assisted re-scattering in clusters. They also interpret it as a kind of multi-plasmon deexcitation instead of damping, since energy is redistributed into selected single particle channels.
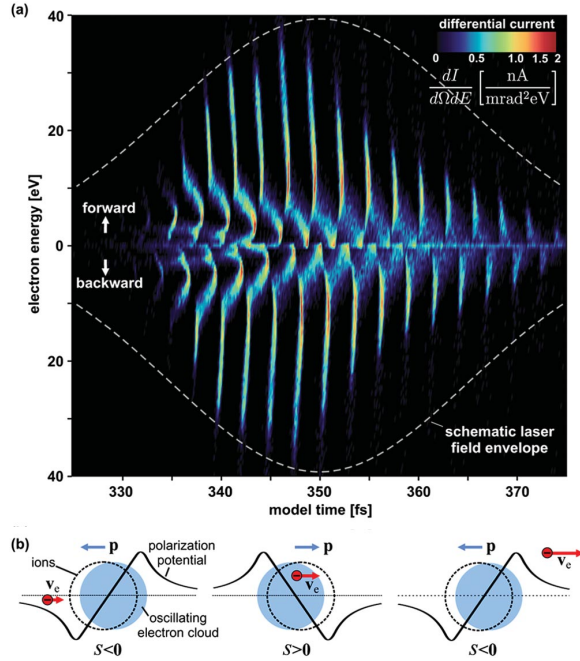
Figure 2.8: Surface-plasmon-assisted re-scattering in clusters (SPARC) (Fennel et al. 2007). Na_{147} clusters are excited with two identical 800 nm, 25 fs and $I = 8 \times 10^{12}$ W/cm^2 pulses. The second pulse is resonant to the surface plasmon. (a) differential current of electrons emitted in a cone $\Omega = 0, 2\pi$ as function of energy and time; (b) Schematics of SPARC. From (Fennel et al. 2007).

A similar effect has been observed by Taguchi et al. (2004) in PIC simulations of much larger Ar clusters, up to 38 nm in diameter. In an analogy to Brunel heating (Brunel 1987), they were able to derive a size dependent scaling law for the laser intensity at the onset of strong absorption.

Mulser et al. (2005) have focused on nonlinear collective phenomena. They considered the electron cloud as a hard sphere of not necessarily identical total charge and size as the ionic one. For large deviations of the electron sphere from equilibrium the restoring potential is no longer harmonic but turns into a Coulombic one. Oscillation frequency decreases here with total energy that is, with the amplitude of the motion. For sufficiently high field strengths ($I = 6.78 \times 10^{17}$ W/cm^2), the electron cloud is pulled out just enough that the oscillation frequency is equal to that of the laser. The energy absorption increases by 5 orders of magnitude. The harmonic oscillator model for the surface plasmon $\omega_0 = \omega_p/\sqrt{3}$ yields here zero absorption.

At intensities of 1×10^{18} W/cm^2, such as those where Mulser et al. find resonant behavior, all atoms are ionized within the first half cycle of the leading edge. The laser field is much stronger than the field of the ions, such that it drives the electron cloud as if it were frozen.

Schroeder et al. (1998) have performed experiments under similar conditions, but with much smaller Xe_{13} clusters and with two different laser systems: a Ti:Sa laser at 800 nm generating $T = 90$ fs pulses with $I = 2 \times 10^{18}$ W/cm^2 and a KrF* system at

248 nm, with $T = 270$ fs and $I = 1 \times 10^{19}$ W/cm^2. Surprisingly, the X-ray yield was enhanced by a factor of 3000 with the UV laser over the IR one. At the intensities employed here, all six 5p electrons of Xe are field ionized within the first half cycle of the leading edge. The electron cloud is removed as a whole from the cluster and then driven back a half cycle later with $E_{\mathrm{coll}} = 20$ keV in the IR field or $E_{\mathrm{coll}} = 10$ keV in UV. The re-colliding electrons can ionize core electrons, leading to emission of characteristic X-rays. However, the excursion of the electron cloud outside the cluster is roughly 20 times larger in the IR field due to the much larger ponderomotive amplitude. It can collide against neighboring clusters, such that its return probability can be more than 500 times smaller. Moreover, the excursion time is larger due to the 3 times longer period, which allows the electron cloud to expand more. The current density of the re-colliding cloud is thus decreased by at least a factor of 9. At the same time, the Lorentz force in the IR field deviates the cloud by at least 5 cluster radii, such that it misses the cluster upon return. Adding up, the IR proves to be less efficient in driving the re-collision, even though the re-collision energy is twice as large as with the UV field and should produce in principle much higher X-ray yields.

To summarize, the high local density of atomic clusters lowers the potential barrier between neighboring ions, increasing the probability for ionization, be it tunnel-ionization or single-photon absorption. It can also have the counter effect, by increasing the probability of resonant tunneling, as shown in Fig. 2.5 at the decrease of photon absorption rate in the X-ray domain. The finite size increases the surface to volume ratio, which favors surface effects such as Mie resonance or Brunel heating over bulk ones, like the volume plasmon excitation. It enables at the same time various resonance appearances, which are all linked to the ability of selected, or all electrons to traverse the whole cluster without collision in a single half cycle.

Chapter 3

Experiments with clusters in the field of a free electron laser

Although based on the same principle as the synchrotron, the free electrons laser achieves its spectacular properties by using the radiation generated by relativistic electrons in a single pass, as shown in Fig. 3.1 (Feldhaus et al. 2005). In a synchrotron, the electron beam is reused millions of times per second before being dumped. The quality of the beam decreases in every pass due to the recoil momentum of the emitted photons, down to a level where it can no longer be corrected by the magnetic fields.
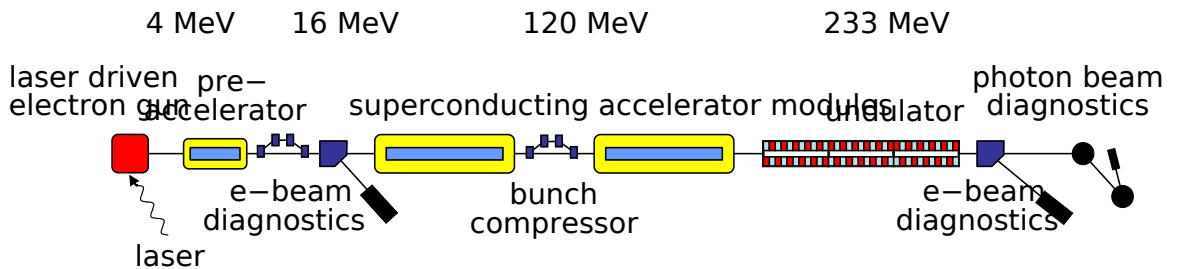

Figure 3.1: Schematic layout of the VUV-FEL at DESY, Hamburg. From Altarelli et al. (2006).

In 2001, the testing facility of the FEL in Hamburg obtained lasing in the range $80 - 120$ nm. Figure 3.2 shows time of flight spectra of Xenon clusters irradiated with 100 fs, $I = 2 \times 10^{13}$ W/cm^2 pulses at 98 nm (12.65 eV) (Wabnitz et al. 2002). With Xenon gas, whose ionization potential $E_{\mathrm{ip}} = 12.1$ eV is just slightly less than the photon energy, isolated atoms were photo-ionized and only singly charged ions have been observed[1]. Clusters have shown higher charges, reaching 8 fold ionization with $N = 30,000$. As shown in the inset, 2.5 keV fast ions have been detected with $N \approx 1500$ clusters. A total absorption of 450 eV, or almost 40 photons per atoms has

---

[1]Additional experiments with a more sensitive MCP detector have shown charges as high as Xe^{6+} already at $I = 1.3 \times 10^{13}$ W/cm^2. These will be discussed in the following. It should noted for the moment that the two-photon ionization rate of Xe$^+$ is very low, roughly 25 times lower than single-photon ionization rate of neutral Xe.

been measured with $N = 2500$ clusters, in very high contrast with the single photon absorption of isolated atoms.
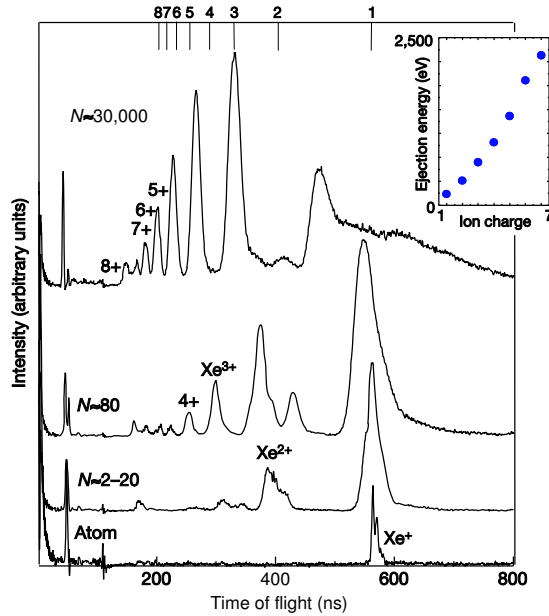

Figure 3.2: TOF mass spectra of Xe clusters of variable sizes exposed to 100fs FEL laser pulses at 98nm (12.65eV) and $I = 2 \times 10^{13}$W/cm^2 power density. Inset: kinetic energy of ions from $N \approx 1500$ clusters as function of their charge. From Wabnitz et al. (2002).

These results were not dependent on the electronic structure of the cluster. Further experiments were performed on Ar clusters, where the FEL was tuned in resonance either to the surface exciton at 105 nm, or to the bulk exciton at 100.5 nm or simply off-resonant at 96.6 nm. Figure 3.3(left) depicts the absorption spectrum of Ar$_{800}$ clusters along with the three employed wavelengths of the FEL. The right hand side of Figure 3.3 shows the TOF spectra for these frequencies, at low intensity ($I = 1.9 \times 10^{11}$ W/cm^2) in the lower panel and high intensity ($I = 1.5 \times 10^{13}$ W/cm^2) in the upper one. In the latter case, where the intensity was similar to the Xe cluster experiment described above, the spectra show no difference at all. Moreover, the clusters were determined to disintegrate completely already at $I = 1.8 \times 10^{12}$ W/cm^2 for all frequencies. With resonant excitation the threshold was 4 times lower, namely slightly above 4×10^{11} W/cm^2. The lower threshold can be easily understood when considering the lower right panel of Fig. 3.3 for the low intensity regime. The spectrum for off-resonant excitation is dominated by singly charged ions and cluster fragments, such as dimers and trimers. With resonant excitation, the fragment signal weakens and higher charged ions such as Ar^{2+} appear instead.

That clusters behave identically at all frequencies for power densities beyond 1.8×10^{12} W/cm^2 indicates that energy absorption in this intensity regime is mostly due to plasma heating and that photo-ionization has already saturated early in the pulse, for both resonant and non-resonant photon absorption.
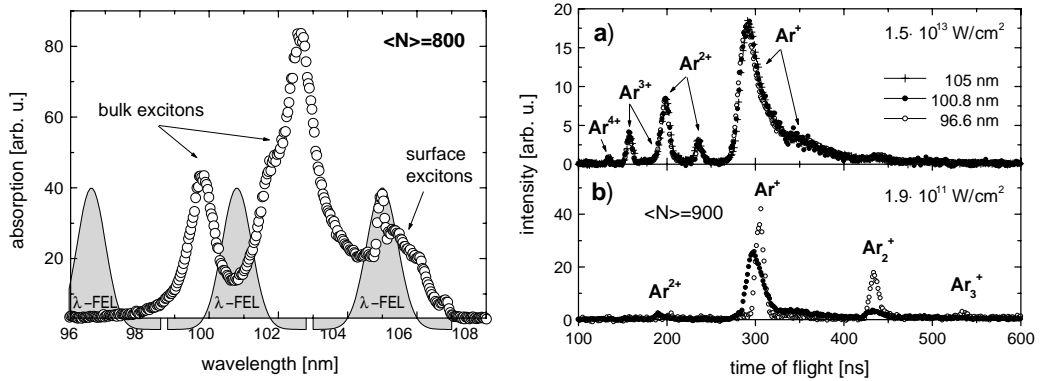
Figure 3.3: Left: Photo-absorption spectrum of Ar_{800} clusters. The FEL radiation wavelength was tuned to surface ($\lambda = 105$ nm) and bulk excitons ($\lambda = 100.8$ nm), as well as off resonant ($\lambda = 96.6$ nm). Right: TOF mass spectra of Ar_{900} clusters at these three FEL wavelengths for $I = 1.5 \times 10^{13}$ W/cm^2 (top) and $I = 1.9 \times 10^{11}$ W/cm^2 (bottom). From Laarmann et al. (2004).

The surprise of the high energy absorption lies in the ponderomotive amplitude x_{p} and energy U_{p}, shown in Table 2.2 in the previous chapter. With IR radiation x_{p} is at least comparable, if not larger than the size of the cluster and U_{p} can reach the order of keV. The electrons are swept back and forth through the whole cluster, which explains the violence of the experiments summarized previously. On the other hand, at already 8 times shorter wavelength, as in these experiments, x_{p} is less than the mean radius of a Xe valence orbital, while U_{p} is negligible on the order of meV.

The findings have sparked theoretical investigations in several groups (Bauer 2004; Georgescu et al. 2007a; Jungreuthmayer et al. 2005; Rusek and Orlowski 2005; Santra and Greene 2003; Siedschlag and Rost 2004). All of them have identified inverse bremsstrahlung (IBS) as the main absorption mechanism, but disagree strongly with respect to the origin of its efficiency.
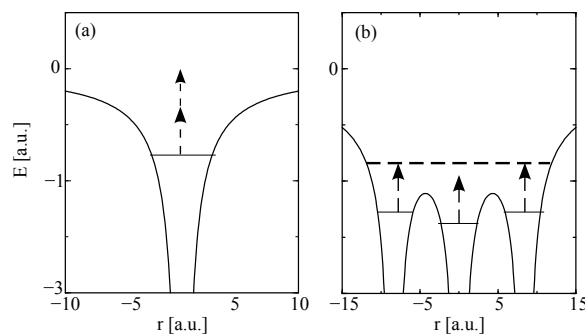

Figure 3.4: Inner-ionization in a cluster. The Hamburg experiment showed that two-photon ionization is much less probable with respect to single-photon absorption. This favors inner ionization, where electrons can be excited from atomic bound states into cluster states by absorption of a single photon. From Siedschlag and Rost (2004).

The ansatz of Siedschlag and Rost (2004) employs the concept of inner-ionization depicted in Figure 3.4. Single-photon ionization of all atoms in the cluster occurs within less than 1 fs. Due to the small distance between the cluster ions, the Coulomb potential is bend so strongly, that further single photon absorption can promote bound electrons into so called inner-ionized cluster states. They are bound with respect to the cluster, but delocalized with respect to the mother atom. The mechanism is very efficient due to the linear increase of the ionization potentials of the rare gas atoms, shown in Figure 3.5. The barrier lowering is proportional to the charge of the atoms, but so does the ionization potential. If the first step is energetically possible, than all of them are until a jump of E_{ip} is encountered, corresponding to a stronger bound next sub-shell. This leads to 8 fold ionization of all atoms in the cluster within a very short time. Efficient IBS is obtained due to the large number of electrons performing small oscillations with the laser field while scattering against highly charged ions.
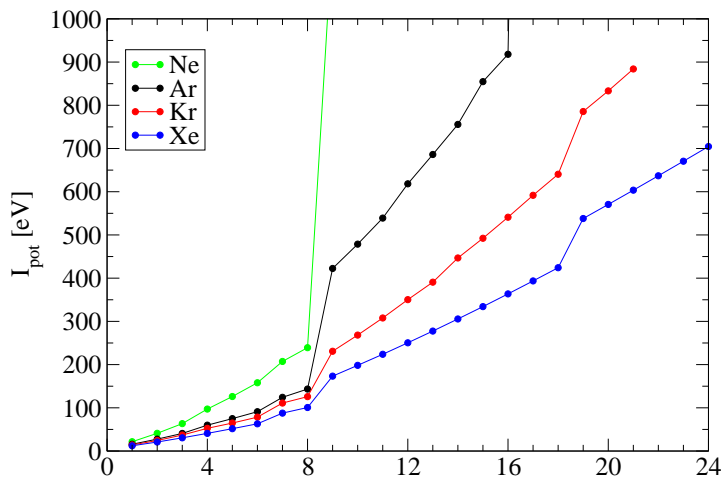

Figure 3.5: Ionization potentials of Ne, Ar, Kr, Xe and their ions.

At the other end, Santra and Greene (2003) introduced a more accurate atomic potential, which allows the electron to feel the full charge of the nucleus as it penetrates the electron cloud. They observe strong scattering of the electrons in this potential, which enhances IBS absorption over scattering in the pure Coulomb potential by a factor of 20. The average transient charge of the cluster ions is only Xe^{2+}. They also considered plasma effects in form of Debye screening.

Two-photon ionization has been initially ruled out by all models on ground of the experimental results shown in Figure 3.2. Evaluation of further data (Laarmann et al. 2004) obtained in different runs with different FEL parameters and a more sensitive MCP detector have shown another picture. Xe^{2+}, even Xe^{3+} charge states appear for power densities as low as 2×10^{12} W/cm^2, and Xe^{6+} already at 1.3×10^{13} W/cm^2. Xe^+ saturates at $< 1 \times 10^{12}$ W/cm^2 for the same pulse length. Santra and Greene (2004) have performed calculations on multi-photon ionization of Xe and its ions at 12.7 eV. Although they find a Xe^+:Xe^{2+} ratio of roughly 2:1 at the end of the pulse, it should be noted that for $I = 7 \times 10^{13}$ W/cm^2 Xe^+ saturates already in 0.5 fs if one considers the experimental cross-section $\sigma_1(Xe) = 65$ Mb (Chan et al. 1992; Samson

and Stolte 2002). The authors overestimated this cross-section by a factor of two. That a considerable amount still exists at the end of the 50 fs long pulse, speaks for a very low Xe^{2+} production rate. With $\sigma_2(Xe^+) = 4.5 \times 10^{-49}$ cm^4s, the ionization rates $\sigma_1 I/\omega$ and respectively $\sigma_2(I/\omega^2)$ stay in a ratio of 25:1 at $I = 7 \times 10^{13}$ W/cm^2.

The combination of photon energy and ponderomotive amplitude make VUV radiation unique. With IR fields, photo-electrons are placed in the continuum with little to zero momentum, because they are created by multi-photon or tunnel ionization. Due to the strong coupling, they are accelerated to several eV within just one laser period. With X-rays, electrons have high momentum from the beginning due to the large photon energy. They no longer interact with the light field once they are in the continuum. The VUV range is just at the cross-over. The photo-electrons are slow, because the photon energy is slightly higher than the ionization potential E_{ip}, and the interaction with light after ionization is very weak. The electrons form a dense, warm plasma, which screens the cluster ions and modifies their atomic properties, such as ionization potential or photo-ionization cross-section.

This work extends the hybrid quantum-classical description employed by Siedschlag and Rost and puts emphasis on the description of atomic structure and plasma environment, which modifies the former through screening. Moreover, a probe method with attosecond XUV laser pulses will be presented in Chapter 6, which could shed more light on the variety of absorption mechanisms proposed so far.

Chapter 4

Clusters under strong VUV pulses: A quantum-classical hybrid description incorporating plasma effects

Hybrid quantum-classical approaches to laser cluster interaction have proved very powerful when the cluster dynamics is dominated by plasma effects and is not influenced by the electronic structure of the cluster, as in the previously described experiment. In the spirit of the three step-model, photo-ionization is dealt with quantum-mechanically through ionization rates, whereas the ionized particles are propagated classically by solving Newton's equations. Such approaches have been employed by many groups (Ditmire et al. 1998; Jungreuthmayer et al. 2005; Last and Jortner 1999; Rose-Petruck et al. 1997; Saalmann and Rost 2003; Siedschlag and Rost 2002) because they have the great advantage to scale to very large systems and to consider electron correlation effects exactly in the plasma dynamics. Quantum-mechanical approaches are limited to small systems, and, as employed for example by Santra and Greene (2003), Walters et al. (2006) or Krainov (2000), do not consider electron correlation for the dynamics of the inner-ionized electrons.

As outlined in the previous chapter, the VUV interaction regime is unique due to screening effects. At the cross-over between the IR and the X-ray regime, the photo-electrons are both slow and interact weakly with the laser field after ionization. They form a dense, warm plasma and localize about the ions, modifying their atomic properties such as ionization potentials and cross-sections. But exactly these electrons define a time scale, suitable to formulate a coarse grained dynamics in the cluster. It allows us to include those processes which in our approach lie at the interface between quantum and classical mechanics, such as the influence of the surrounding *classical* charged particles (ions and electrons) on the photo-ionization rate of bound *quantum* electrons.

We will address here the photo-ionization of many-electron atoms in a cluster environment. Starting from the isolated atom, we will consider the lowering of the

ionization threshold through neighboring ions, then identify those electrons which localize about the ions, effectively screening them. The ionization potential and photo-ionization cross-section of screened bound electrons will be introduced. The last section will address the classical propagation of electrons and ions, with emphasis on the model potentials used to avoid the Coulomb singularity at the interaction of charged particles. This was not an issue in the IR-regime because the ponderomotive amplitude x_{p} was much larger than the spatial extent of the atoms, where the non-singular approximations deviate from the Coulomb potential. In the VUV regime, x_{p} is much smaller than the atom, such that the electron motion is sensitive to the exact shape of these potentials, and an examination of the implications is needed.

The model will be illustrated in the next chapter at the example of Ar_{147} under VUV radiation similar to the one available at FLASH, in Hamburg (Ayvazyan et al. 2002a, 2006; Wabnitz et al. 2002).

4.1 Photo-ionization into the cluster

4.1.1 Photo-ionization of a single cluster atom

Considering the initial and final configurations of a photo-absorption process, we do not resolve the full level splittings, but instead average over all allowed transitions, as sketched in Fig. 4.1.
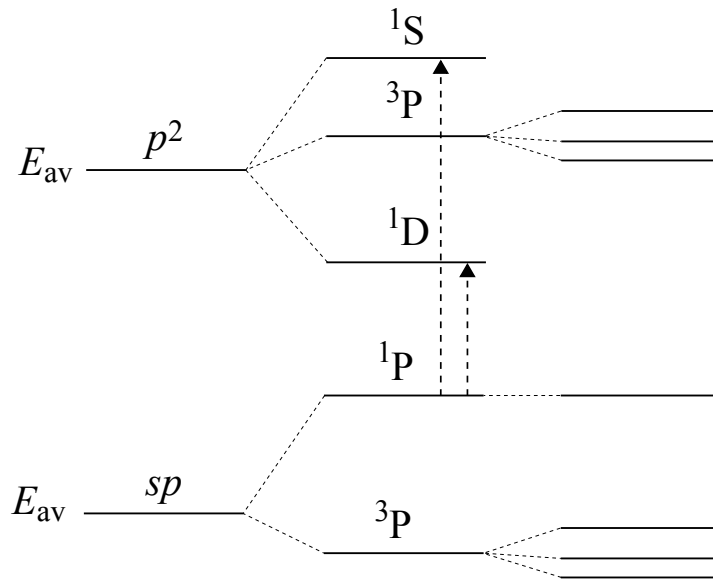

Figure 4.1: Average over all allowed transitions between two configurations, in this case sp and pp. The average transition energy is not simply the difference of the configuration-average or center-of-gravity energies because many transitions are not allowed in the dipole approximation.

The transition cross-section is obtained by summing over all allowed final states and taking the mean over all initial states. The mean of the transition energies will

be taken as the effective transition energy.

In the independent-particle model, the electrons move in a self-consistent, spherically symmetric potential without interacting with each other. The angular momenta are thus constants of motion and the one-electron wave function is an eigenfunction of $\mathbf{l}_i^2$, l_{z_i}, $\mathbf{s}^2$ and s_{z_i}

$$\varphi_i(\mathbf{r}_i) = \frac{1}{r}\phi_{n_i l_i}(r_i) \cdot Y_{l_i m_i}(\theta_i, \phi_i) \cdot \sigma_{m_{s_i}}. \tag{4.1}$$

The total wave function $|\Psi\rangle$ of the atom is constructed by coupling and anti-symmetrization of the product wave functions $\prod_i |\varphi_i\rangle$.

This work will mainly use conventions and techniques from R.D. Cowan's *Theory of atomic structure and spectra* (Cowan 1981), which is also accompanied by a powerful Hartree-Fock code provided at `ftp://aphysics.lanl.gov/pub/cowan`.

Coupling and anti-symmetrization are performed by means of the *coefficient of fractional parentage*, or *cfp* technique (Cowan 1981, §9-5, 9-8). $\phi_{n_i l_i}$ are then determined numerically from the Hartree-Fock equations by minimizing the configuration-average energy

$$E_{\mathrm{av}} = \frac{\sum_b \langle \Psi_b | H | \Psi_b \rangle}{\sum_b} \tag{4.2}$$

under the constraint of the orthogonality of $\phi_{n_i l_i}$

$$\int_0^\infty \phi_{nl}(r)\phi_{n'l}(r)dr = \delta_{nn'}. \tag{4.3}$$

The summation in (4.2) runs over all basis functions of the configuration in question.

One could also minimize the energy of each eigenstate of the given configuration, but that would involve too much a numerical effort. Instead, one evaluates the radial component $\phi_{n_i l_i}$ first and then recomputes the expectation value of the Hamiltonian for each of the eigenstates, leading to correlation, exchange, spin-orbit and Zeeman corrections, as the electron-electron, spin-spin, spin-orbit and magnetic interactions are taken into account.

The photo-ionization cross-section is given by

$$\sigma_{\mathrm{ph}} = 4\pi^2 \alpha \hbar \omega |\langle \gamma' J' M' | \hat{\epsilon}_0 \sum_i \mathbf{r}_i | \gamma J M \rangle|^2 \tag{4.4}$$

with anti-symmetrized many-electron initial and final states, $|\gamma J M\rangle$ and $|\gamma' J' M'\rangle$ respectively (Cowan 1981; Friedrich 2006). J is the total angular momentum and M its magnetic quantum number. γ represents the set of all other good internal quantum numbers of the atom.

Summing over all final states and averaging over all initial ones

$$\frac{\sum_{\gamma J, \gamma' J'}(2J+1)\sigma_{\mathrm{ph}}(\gamma, J; \gamma' J')}{\sum_{\gamma J}(2J+1)} \tag{4.5}$$

leads to (see Appendix A for the full derivation)

$$\sigma_\ell(\omega) = \frac{w_i}{3}\frac{4\pi^2 \alpha \omega}{2\ell+1}[(\ell+1)d_r^2(\ell, \ell+1) + \ell d_r^2(\ell, \ell-1)]. \tag{4.6}$$

w_i is the occupation number of the initial orbital i and $d_r(\ell, \ell')$ is the radial dipole matrix element

$$d_r(\ell, \ell') = \int_0^\infty \phi_{n\ell}(r)\, r\, \phi_{n'\ell'}(r) dr\,. \tag{4.7}$$

The average transition energy is computed in a similar manner

$$\Delta E_{i \to f} = \frac{\sum_{\gamma J \to \gamma' J'} (2J+1)(E(\gamma' J') - E(\gamma J))}{\sum_{\gamma J.\gamma' J'} (2J+1)}\,. \tag{4.8}$$

In contrast to (4.5), the denominator also includes the additional sum over $\gamma' J'$. The average transition cross-section performs a sum over all final states, the transition energy involves their average.

It should be noted that (4.8) is not equivalent to the difference of the configuration-average energies (4.2)

$$\Delta E_{\mathrm{av}} = \frac{\sum_{\gamma' J'} (2J'+1)E(\gamma' J')}{\sum_{\gamma' J'} (2J'+1)} - \frac{\sum_{\gamma J} (2J+1)E(\gamma J)}{\sum_{\gamma J} (2J+1)}\,. \tag{4.9}$$

On the one hand, most of the levels are not included in the allowed transitions array. On the other hand, the final energies $E(\gamma' J')$ do not enter the Eq. (4.8) with their full multiplicity $2J'+1$ due to the limitations imposed by the dipole transition rules $M' - M = 0, \pm 1$.

The neighboring ions in the cluster lower the ionization threshold. What was a discrete photo-excitation for an isolated atom becomes at the same photon energy photo-ionization into the cluster. We define a continuous absorption cross-section in the discrete region of the spectrum by distributing the oscillator strength f_n of each spectral line onto the corresponding energy interval,

$$\sigma_n(\omega) = \frac{2\pi\alpha f_n}{(E_{n+1} - E_{n-1})/2}\,. \tag{4.10}$$

n is here simply an index of the average spectral lines $\gamma J - \gamma' J'$ which start from the ground state γJ. We demand at the same time that the renormalized photo-excitation cross-section merges into the photo-ionization cross-section at threshold. This is confirmed in Fig. 4.2, where the continuous line shows the result of (4.10) for Ar.

Fig. 4.2 also shows a comparison with two other approximations for the photo-absorption cross-section. The first one belongs to Rost (1995) and gives the photo-ionization cross-section of a single-electron atom mainly as a function of its radial wave function at $r = \omega^{-1/2}$

$$\sigma(\omega) = \frac{2\pi^2\alpha Z^2 \sqrt{l+1}}{3\omega^{5/2}} |\phi_{nl}(r = \sqrt{\frac{l+1}{\omega}})|^2, \tag{4.11}$$

which for a $1s$ wave function $\phi_{1s} = 2\beta^{3/2}e^{-\beta r}$ with the effective charge β becomes

$$\sigma_\beta(\omega) = \frac{8\pi^2\alpha Z^2 \beta^3}{3\omega^{7/2}} e^{-2\beta/\sqrt{\omega}}. \tag{4.12}$$
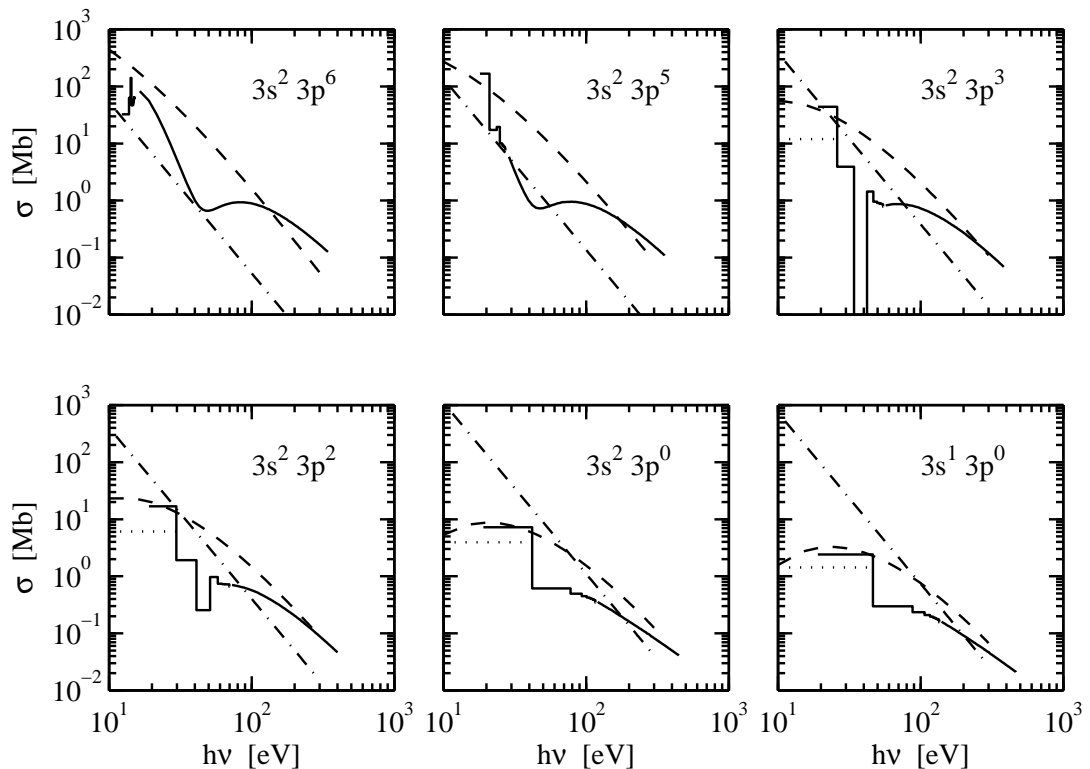
Figure 4.2: Comparison of several approximations of the photo-absorption cross-section. Full line: (4.10). The discrete spectrum has been calculated up to the final principal quantum number $n' = 16$. The energy of the outgoing electron in the continuous part of the spectrum starts at 1.5 eV above threshold; dotted line: lower bound of the cross-section when ionizing into the cluster, as described in (4.14); dashed line: (4.12); dash-dotted line: (4.13).

Eq. (4.11) and (4.12) can be generalized to N-electrons. For the uncorrelated ground state of He, it leads to the simple relation $\sigma(\omega) = 2\sigma_\beta(\omega)$.

The second ansatz is again a hydrogenic one and was introduced for bound-bound or bound-free transitions of slow electrons, that is, electrons of either high principal quantum number n or low asymptotic momentum k (Zel'dovich and Raizer 1966, V.§12), (Cowan 1981, §14-14), (Bethe and Edwin 1977, §71)

$$\sigma_{(n)}(\omega) = \frac{32\pi\alpha}{3\sqrt{3}} \cdot \frac{E_{\text{ip}}(n)^2}{n\omega^3} \,, \tag{4.13}$$

where $E_{\text{ip}}(n)$ is the ionization potential of the state to be ionized.

For the comparison we have multiplied both (4.12) and (4.13) by the occupation number w_i of the initial orbital. In (4.12) we have set $Z = 18$ and the effective charge β was related to the ionization potential $\beta = \sqrt{2n^2 E_{\text{ip}}(n)}$. $\sigma_\beta(\omega)$ of Eq. (4.12) and $\sigma_n(\omega)$ from (4.10) show good agreement at the asymptotes. For medium energies, (4.10) shows the well known Cooper effect, an interference effect which is not included in (4.12).

Special care needs to be taken in case of the renormalization (4.10) for the first spectral line above the ionization threshold, n_thr. The corresponding energy interval extends then from the threshold itself to the next higher spectral line $n_\mathrm{thr} + 1$

$$\sigma_{n_\mathrm{thr}}(\omega) = \frac{2\pi\alpha f_{n_\mathrm{thr}}}{(E_{n_\mathrm{thr}+1} + E_{n_\mathrm{thr}})/2 - E_\mathrm{thr}}. \tag{4.14}$$

As will be shown later, E_thr is influenced strongly by the cluster environment and can fluctuate in quite a wide range. The dotted line in Fig. 4.2 marks the lower bound of the renormalized photo-ionization cross-section for the case of the lowest possible threshold, corresponding to the widest energy range the oscillator strength can distributed onto.

4.1.2 Identification of localized electrons

Once an electron absorbed a photon, it is propagated classically in the field of the laser and of the other charged particles. For the given photon energies (10 eV $<$ $\hbar\omega <$ 30 eV) and ionization potentials (10 eV $< E_\mathrm{ip} <$ 20 eV), the generated photo-electrons are slow and redistribute the energy among each other quickly. A simple estimation using Spitzer's self-collision time (Spitzer 1962, §5.3)

$$t_c = \frac{v^2}{\langle(\Delta v_\perp)^2\rangle} = \frac{(3k_BT)^{3/2}}{4\pi n_e\{\mathrm{erf}(\sqrt{1.5}) - G(\sqrt{1.5})\}\log\left(\frac{9k_B^3T^3}{4\pi n_e}\right)} \tag{4.15}$$

yields a thermalization time on the order of 0.8 fs. The Debye length $\lambda_D = \sqrt{k_BT/4\pi n_e}$ was chosen for the upper limit of the Coulomb logarithm and the temperature was set according to the average kinetic energy of the electrons, assuming that every second atom would be ionized once instantaneously, that is $3k_BT = 2E_\mathrm{kin} \approx 2\hbar\omega$. $\mathrm{erf}(x)$ is the error function and $G(x)$ is defined as

$$G(x) = \frac{\mathrm{erf}(x) - x\,\mathrm{erf}'(x)}{2x^2} \tag{4.16}$$

The very fast thermalization of the cluster plasma will be confirmed in the next chapter, Sec. 5.1, by means of molecular dynamics simulations. It should be noted though that t_c describes the energy redistribution about the average particle energy (MacDonald et al. 1957). $\langle(\Delta v_\perp)^2\rangle$ is a diffusion coefficient in velocity space (Chandrasekhar 1943). By definition, t_c represents therefore the time needed by a particle of the average kinetic energy of a Maxwellian plasma to be deflected by an angle of 90° and change its energy by 100%. Further on, it can take up to $10t_c$ until the higher tail of the Maxwell distribution is filled (MacDonald et al. 1957).

We are interested in the lower part of the single particle distribution function, because these electrons will localize about the ions, being in effectively excited states about them and screening the bound electrons. In order to find these electrons we trace the revolution angle $\phi_j^{j_\alpha}$ of each electron j around the closest ion j_α. Whenever j_α changes, $\phi_j^{j_\alpha}$ is reset to zero. Should $\phi_j^{j_\alpha}$ become larger than $\phi_0 = 4\pi$, so is the

electron localized about the ion. The choice $\phi_0 = 4\pi$ is motivated by Fig. 4.3. It shows the energy of each electron in the system with respect to its closest ion against the angle it has revolved about that ion. For all time instants, one can clearly identify a region of small revolution angles and rather high energies and a region of very large revolution angles and low energies. The former can be attributed to delocalized electrons, which visit many ions, while the latter corresponds to localized electrons, which spend a lot of time, or revolutions, about a single ion. The separation is at roughly 3π, for safety reasons we set $\phi_0 = 4\pi$.
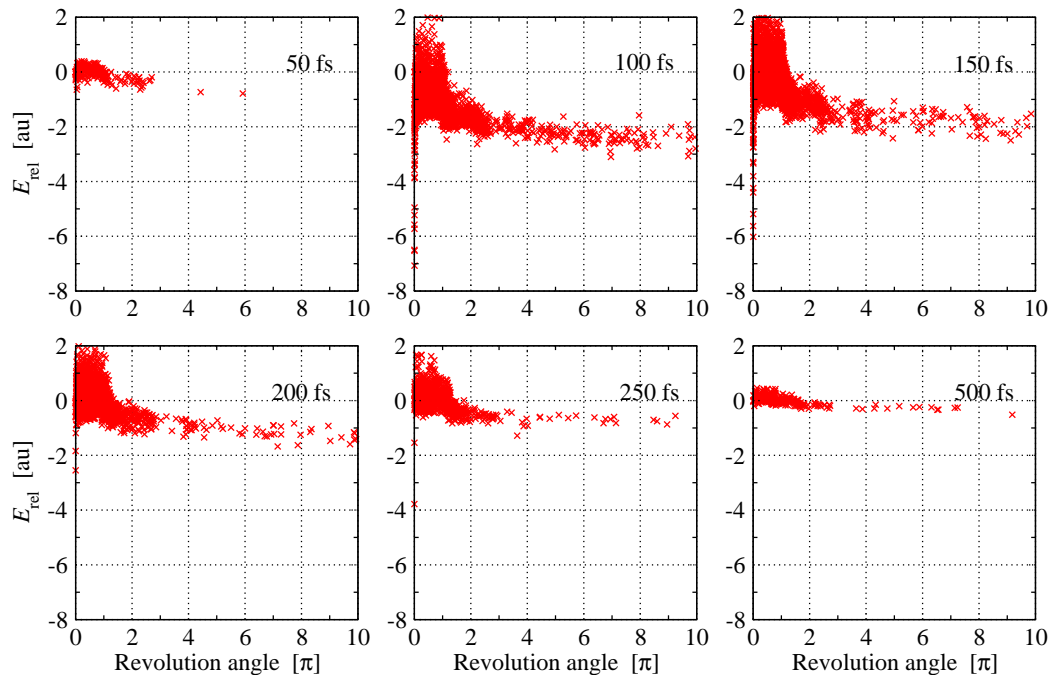

Figure 4.3: Electron energy with respect to the closest ion against the angle of revolution around that ion. Extracted from the simulation of a Xe_{147} cluster exposed to a 100 fs, $\hbar\omega = 12.7$ eV and $I = 7 \times 10^{13}$ W/cm^2.

To support our localization criterion, we plot in Fig. 4.4 the electron energy against the position in the cluster and color code the localization status according to the new criterion. Red for localized electrons, green for delocalized electrons. All electrons which find themselves inside a cylinder of Wigner-Saitz radius along the longest axis of the cluster have been collected from 40 independent realizations. The blue line shows the potential landscape in the cluster averaged over these realizations according to the method described in Appendix B. A clear separation line between the red and the green region can be observed, running parallel to the saddle points of the averaged potential.

Knowing that there a lot of electrons performing many rotations around the same ion, we can consider the mechanisms, or the interactions inside the cluster nanoplasma from a different perspective. The localized electrons are effectively in excited, or Rydberg states about the ions. These ions, together with the localized electrons
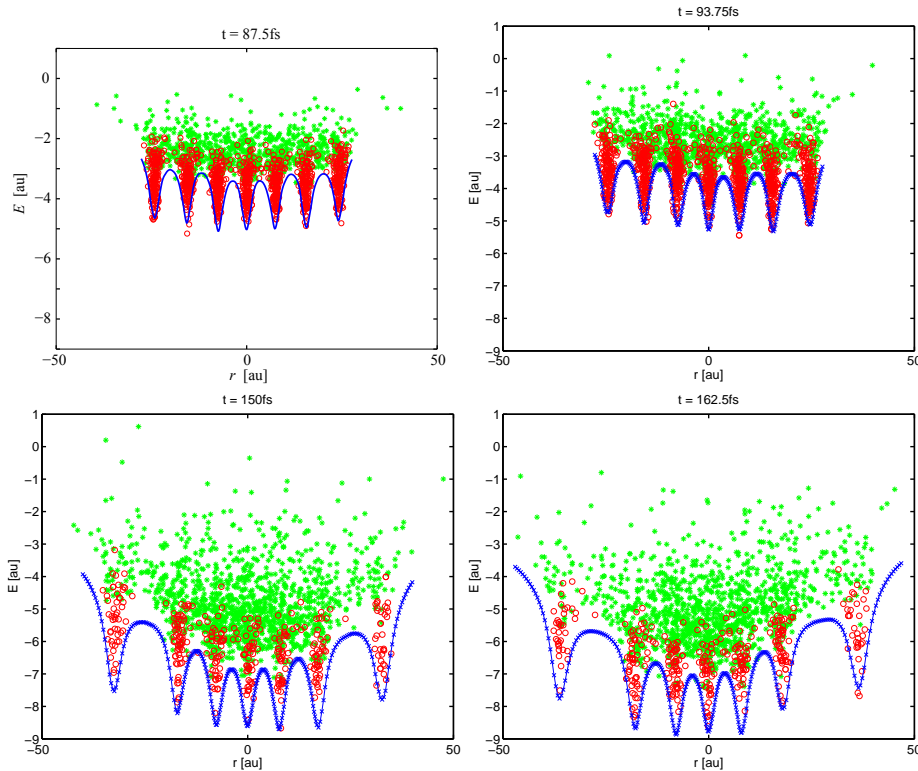
Figure 4.4: Electron total energy against position in cluster for the same situation as in Fig. 4.3. The localization status according to the revolution angle about the closest ion is color coded: red for localized, green otherwise. Visible are all electrons within a cylinder along the longest collinear chain of atoms in the cluster and with a radius equal to the Wigner-Saitz radius.

on Rydberg orbits are embedded in a low density, delocalized electron plasma with which they stay in thermal equilibrium.

The mean revolution period of the localized electrons sets the time scale for a coarse-grained dynamics. With an initial guess $T_0 = 1$ fs, we update T_{i+1} at time $t_i = \sum_{j=0}^{i} T_j$ according to the general sequel

$$\bar{T}_{i+1} = \frac{1}{N} \sum_j \frac{2\pi}{\phi_j^{j_\alpha}(T_i)} T_i \,, \tag{4.17}$$

where $\phi_j^{j_\alpha}(T_i)$ is the revolution angle completed by the electron during the last interval T_i. We also add one standard deviation σ_{i+1} to make sure most of the localized electrons have made a full revolution

$$T_{i+1} = \bar{T}_{i+1} + \sigma_{i+1}. \tag{4.18}$$

The time intervals T_i defined by the localized electrons play a crucial role in the description of the entire cluster dynamics. They provide a natural time scale to interpolate between the quantum-mechanical, rate based description of the ionization

process and the classical, fully deterministic treatment of the ionized electrons. Over the time interval $t_i < t < t_i + T_{i+1}$ all processes involving quantum rates will be considered within a fixed cluster environment, whose properties have been averaged over the previous time interval $[t_i - T_i, t_i)$.
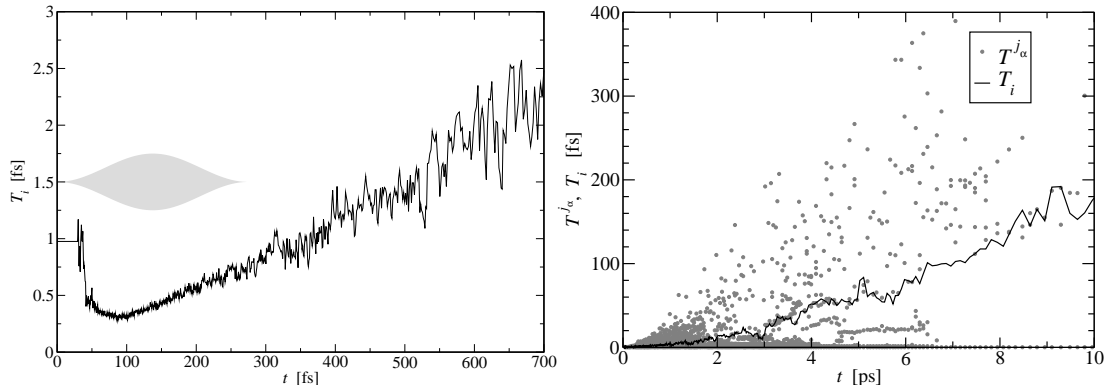

Figure 4.5: Intervals T_i as in Eq. (4.18). Left: small time scale, comparable with the laser pulse. Right: long time scale. The dots show single revolution periods T^{j_α}. With the increasing inter-ionic distance, very large orbits with large revolution periods become possible.

The evolution of the time intervals T_i is shown in Fig. 4.5. With the disintegration of the cluster, very wide revolution orbits are possible due to the increasing inter-ionic distance. These orbits have very large revolution periods, thus increasing the overall T_i. They will not enter Eq. (4.17) when T_{i+1} is computed because they will not have yet completed a full revolution, but will be considered for T_{i+2} or later. These lead to very large fluctuations of T_i, meaning again that some of the orbits will be alternatively over- and under weighted in (4.17). For this reason we also keep track of the last revolution period $T^{j_\alpha}_{\text{prev}}$ of each electron and use it in Eq.(4.17) if the electron is localized until it has completed a new full revolution, that is $\phi^{j_\alpha}(T_i+T_{i+1}+\ldots) >= 2\pi$. T^{j_α} is then updated to the new value.

With the localized electrons in excited states about the ions, the next two sections will deal with the ionization potential and the photo-ionization cross-section of a core electron in the presence of Rydberg electrons, respectively.

4.1.3 Equivalent configurations

We keep record of the number of electrons n_α localized about each ion α and average their total energy over the time intervals T_i

$$E_\alpha^* = E(q_\alpha) + \sum_{j=1}^{n_\alpha} \left(\frac{p_j^2}{2} - q_\alpha v(j,\alpha) \right) + \sum_{j>k=1}^{n_\alpha} v(j,k) . \qquad (4.19)$$

$E(q_\alpha)$ is the center of gravity ground state energy E_{av} (4.2) of ion α. $v(j,k)$ is for the moment a generic potential describing the interaction between charged particles. It

is finite at origin, but turns into a Coulomb potential as quickly as possible. Explicit shapes will be discussed in Section 4.2.

We set E_α^* equal to the energy of some multiply excited ion of the same total effective charge q_α^{eff}, as shown in the lower left of Fig. 4.6

$$q_\alpha^{\text{eff}} = q_\alpha - n_\alpha. \tag{4.20}$$

The ionization potential of a core electron in this situation is the energy difference between the final state, where the active electron is missing (upper left), and the current state. To simplify the calculations we introduce the equivalent configuration of the ion on the right column of Figure 4.6. It has the same total energy, but all excited electrons except one are relaxed onto the last occupied orbital. The remaining electron is then "raised" on an even higher Rydberg state, to keep the total energy constant.
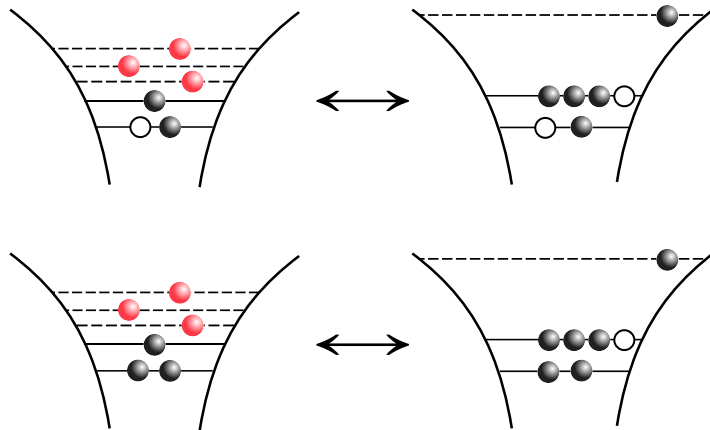

Figure 4.6: Construction of the equivalent configuration for two ions, $3s^2 3p^1$ and respectively $3s^1 3p^1$, with three localized (red) electrons each. The open circles denote holes.

We assume that neither the principal quantum number n, nor the angular momentum ℓ of the spectator Rydberg electron change during ionization from a deeper orbital. The ionization potential E_{ip} is then given by

$$E_{\text{ip}}(C_q, n\ell) = E(C_{q+1}, n\ell) - E(C_q, n\ell) \tag{4.21}$$

where $E(C_q, n\ell)$ represents the total energy of a q-fold charged ion with orbital configuration C_q. An electron of C_q is on a Rydberg orbit $n\ell$.

Fig. 4.7 shows $E(C_q, n\ell)$ against the principal quantum number n for several charge states of Ar and $\ell = 0$, 1 and 2, respectively. Given the total energy E_α^*, we identify a possible initial configuration $(C_q, n\ell)$. With the previous assumption, n and ℓ do not change during ionization of a deeper orbital, any ionization process from such an orbital is just a vertical jump to the curve of the final configuration $(C_{q+1}, n\ell)$. The energy difference is the ionization potential.
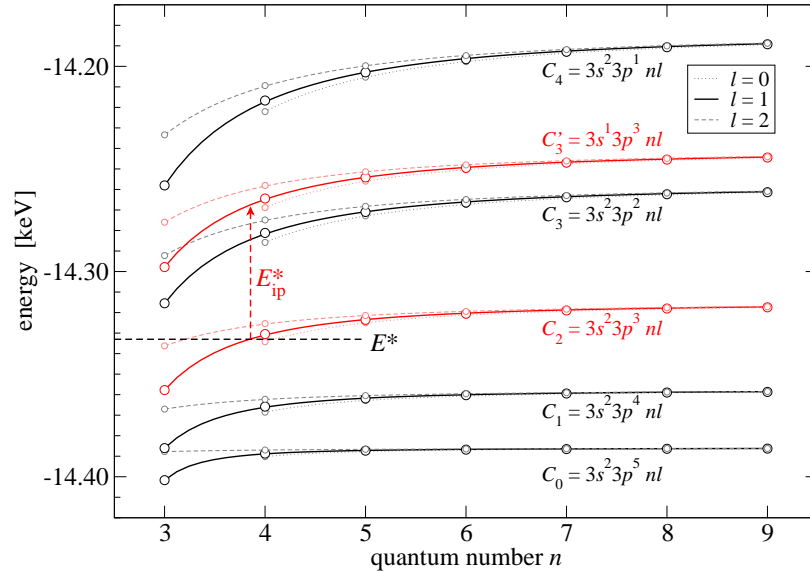
Figure 4.7: The total energy $E(C_q, n)$ for several Ar^{q+} ions with one electron in a Rydberg state of principal quantum number n and $\ell = 1$ (circles), as calculated with Cowan's HF code (Cowan 1981). Full line: the quantum-defect fits according to Eq. (4.22). The dashed vertical line shows the ionization of an s electron from an equivalent configuration of total energy E^* as defined in Eq. (4.19). E_{ip}^* denotes the ionization potential (4.21), (4.26).

For finite values of n, $E(C_q, n\ell)$ can be approximated by a quantum defect formula (Bransden and Joachain 2003)

$$E(C_q, n\ell) = E(C_q, \infty) - \frac{1}{2}\left(\frac{Z_{\text{eff}}(q, \ell)}{n - \mu_{q,\ell}}\right)^2 , \qquad (4.22)$$

where $E(C_q, \infty)$ does not depend on ℓ and $Z_{\text{eff}}(q, \ell)$ is defined over the ionization potential $E_{\text{ip}}(C_q, n_\ell \ell)$ of the lowest ℓ state n_ℓ

$$\begin{aligned}
Z_{\text{eff}}(q, \ell) &= (n_\ell - \mu_{q,\ell})\sqrt{2 \cdot E_{\text{ip}}(C_q, n_\ell \ell)} \\
&= (n_\ell - \mu_{q,\ell})\sqrt{2[E(C_q, \infty) - E(C_q, n_\ell \ell)]} .
\end{aligned} \qquad (4.23)$$

For the argon configurations depicted in Fig. 4.7, $n_\ell = 4$ for $\ell = 0$ and $n_\ell = 3$ otherwise. $\mu_{q,\ell}$ is a free parameter in these expressions, which has been fitted for best agreement of Eq.(4.22) with the Hartree-Fock energies shown in Fig. 4.7. The result of the fits is represented there by the lines connecting the data points. The quantum defect approximation is thus very accurate at intermediate n, where we need it. The following table summarizes the fit parameters $\mu_{q,\ell}$ for those configurations shown in Fig. 4.7

	q	$\ell = 0$	$\ell = 1$	$\ell = 2$
$3s^2 3p^5\ n\ell$	0	2.25	2.26	0.072
$3s^2 3p^4\ n\ell$	1	1.82	1.81	0.65
$3s^2 3p^3\ n\ell$	2	1.51	1.47	0.70
$3s^2 3p^2\ n\ell$	3	1.26	1.20	0.59
$3s^1 3p^3\ n\ell$	3	1.25	1.17	0.62
$3s^2 3p^1\ n\ell$	4	1.05	0.98	0.45

$\mu_{q,\ell}$ is very low for d states, which do not penetrate the core much due to the centrifugal barrier. It is also mostly dependent on q and less on the detailed structure of the core, as $3s^2 3p^2 n\ell$ and $3s^1 3p^3 n\ell$, both with $q = 3$ show. The quantum defect is much smaller with higher charge states, but changes relatively little over a single ionization step $\Delta q = 1$ if ℓ, the angular momentum of the spectator Rydberg electron does not change. Let us assume $\mu_{q,\ell}$ stays constant across one ionization step. Inserting the quantum defect approximation (4.22) for both C_q and C_{q+1}, the initial and respectively the final configurations in (4.21), one obtains a simple equation system

$$E_{\mathrm{ip}}^*(C_q) \equiv E_{\mathrm{ip}}(C_q, n) = E(C_{q+1}, \infty) - \frac{E(C_{q+1}, \infty) - E(C_{q+1}, n_0)}{(n - \mu_q)^2} - E_\alpha^*$$

$$E_\alpha^* = E(C_q, \infty) - \frac{E(C_q, \infty) - E(C_q, n_0)}{(n - \mu_q)^2}\,, \tag{4.24}$$

where we assumed that the energy of the initial state is known $E(C_q, n\ell) = E_\alpha^*$. $(n - \mu_{q,\ell})$ can be fully eliminated

$$E_{\mathrm{ip}}^*(C_q) = [E(C_{q+1}, \infty) - E^*] - \frac{E_{\mathrm{ip}}(C_{q+1}, \ell)}{E_{\mathrm{ip}}(C_q, \ell)}[E(C_q, \infty) - E^*]\,. \tag{4.25}$$

The dependence on ℓ persists in the ionization potentials $E_{\mathrm{ip}}(C_q, \ell) = E(C_q, \infty) - E(C_q, n_\ell\ell)$. For low charge states, such as $3s^2 3p^5 n\ell$ or $3s^2 3p^4 n\ell$, hardly any configuration other than $\ell = 1$ is possible. For higher charges, Eq. (4.25) yields similar results for all ℓ, which is also the optical impression of Fig. 4.7. We choose therefore $\ell = 1$ for these particular cases and generally, ℓ will be set equal to the angular momentum of the ground state of C_q, such as $3s^2$ for C_6. Eq. (4.25) becomes

$$E_{\mathrm{ip}}^*(C_q) = [E(C_{q+1}, \infty) - E^*] - \frac{E_{\mathrm{ip}}(C_{q+1})}{E_{\mathrm{ip}}(C_q)}[E(C_q, \infty) - E^*]\,, \tag{4.26}$$

where $E_{\mathrm{ip}}(C_q)$ is the ionization potential of the ground state C_q. Eq. (4.26) does not depend on n or ℓ anymore. It is a simple interpolation between the ionization potential of C_q and the ionization potential of C_{q+1}, with E_α^* as the interpolation key.

4.1.4 Over-barrier inner-ionization

We have so far separated the cluster environment in localized and delocalized electrons and ions. The localized electrons define the time intervals T_i and have been

mapped, together with their respective ions, to effective excited ions. The charge of an effective ion is the charge of the ion minus the number of localized electrons. The lowering of the ionization threshold in the cluster due to neighboring ions, as sketched before in Fig. 2.4 for a simple three ion scenario, will now be taken a step further to the effective ions.

Following the conclusion of the Sec. 4.1.2, we will evaluate the average charge distribution in the cluster over the time intervals T_i, to determine the potential landscape and thus the threshold for inner ionization. The delocalized electrons are recorded as such, the localized ones are counted together with the ions they are localized about by means of the effective charge q_α^{eff}. The charge distribution is recorded on a grid which is resized automatically to keep up with the cluster expansion. The spacing is chosen such, that there are 8 points between the closest two atoms. At the end of T_i, the potential is computed by a convolution method presented in Appendix B. The charge distribution is then reinitialized to zero and the calculated potential is used throughout T_{i+1}.

The energy balance for an electron to be photo-ionized reads

$$E_i + V_i + \hbar\omega = E_f + V_f \,, \tag{4.27}$$

with the initial and final local contributions from the mother ion

$$E_i = -E_{\text{ip}}^*, \quad E_f = E_{\text{kin}} - (q_\alpha^{\text{eff}} + 1)v(\alpha, \text{bar}), \tag{4.28}$$

and the time averaged cluster contributions

$$V_i = \sum_{j \neq \alpha} q_j v(j, \alpha), \quad V_f = \sum_{j \neq \alpha} q_j v(j, \text{bar}) \,. \tag{4.29}$$

Index j runs over all delocalized electrons and all ions but ion α. E_{ip}^* is the ionization potential (4.26), and $v(i, j)$ is the interaction potential (4.42) between two particles at $\mathbf{r}_i$ and $\mathbf{r}_j$, respectively. V_i is the potential created by all other particles at the position of atom α, V_f is the same potential at threshold, as shown in Fig. 4.8. Letting $E_{\text{kin}} = 0$ in (4.27) and (4.28) leads to the amount of energy needed to ionize an electron bound to a screened atom into the cluster

$$E_{\text{ip}}^{\text{eff}} = E_{\text{ip}}^* - (q_\alpha^{\text{eff}} + 1)v(\alpha, \text{bar}) + V_f - V_i. \tag{4.30}$$

The position $\mathbf{r}_{\text{bar}}$ of the barrier is determined by the lowest saddle point of $V_f(\mathbf{r}) - (q_\alpha^{\text{eff}} + 1)v(\alpha, \mathbf{r})$

$$\frac{\partial}{\partial \mathbf{r}}\left[V_f(\mathbf{r}) - (q_\alpha^{\text{eff}} + 1)v(\alpha, \mathbf{r})\right] = 0 \tag{4.31}$$

It should be noted that the grid based calculation returns the full cluster potential $V(\mathbf{r})$, which also includes the contribution of the parent ion α. Eqs. (4.30) and (4.31) become in this case

$$E_{\text{ip}}^{\text{eff}} = E_{\text{ip}}^* + \{V(\mathbf{r}_{\text{bar}}) - v(\alpha, \text{bar})\} - \{V(\mathbf{r}_\alpha) - q_\alpha^{\text{eff}}v(0)\} \tag{4.32}$$

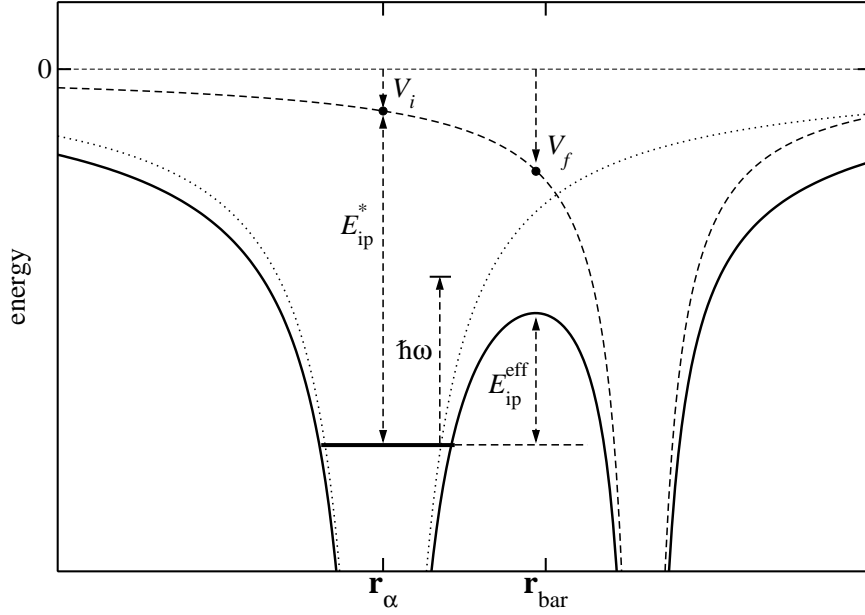$$\frac{\partial}{\partial \mathbf{r}}\left[V(\mathbf{r}) - v(\alpha, \mathbf{r})\right] = 0 \,, \tag{4.33}$$

Figure 4.8: Sketch of the energy balance for the photo-ionization of a cluster ion α. The cluster potential is symbolized by a single neighboring ion. The thick full line indicates the full cluster potential, the thin long dashed line represents the cluster environment, i.e. the cluster potential without the contribution from the ion itself. The dotted line is the Coulomb potential for $q_\alpha^{\text{eff}} + 1$, i.e. the field of the ion if the electron would be ionized. The interaction of the bound electron with the nucleus is represented by E_{ip}^*.

where the *self-interaction* has been subtracted from the total potential to obtain V_i. For V_f one additional nuclear charge had to be added.

The solutions of Eq. 4.33 are located each between the ion α and one of the next neighbors. It is therefore sufficient to look for a maximum of $V(\mathbf{r}) - v(\alpha, \mathbf{r})$ along each of these directions. The lowest maximum is chosen as the ionization threshold. The maximization problem is solved with a golden section algorithm (GSL 2007).

4.1.5 Effective cross-section for inner ionization

In the mapping procedure presented so far, the radial component of the screened, therefore delocalized, atomic orbitals was stated in terms of the unscreened, delocalized orbitals of the equivalent configuration. The former is induced by the cluster environment, whereas the latter is inherent in the mutual repulsion of the larger number of bound electrons. One may speak, in this context, of a projection of the screened wave function onto a delocalized, unscreened basis set.

We can now take advantage of Eq. (4.6). In the new "basis", the radial dipole matrix elements (4.7) are already available in the form of the photo-ionization cross-section of the equivalent configuration. It is only needed to replace the multiplicity w_i in Eq.(4.6) by the number of the actually active, *quantum* bound electrons (black

electrons in Fig. 4.6)

$$\sigma^{\mathrm{scr}}(q) = \frac{w_{\mathrm{act}}}{w_{\mathrm{eqv}}}\sigma(q_{\mathrm{eqv}}) \tag{4.34}$$

4.2   Classical propagation of charged particles

The ionization cross-section is evaluated for each atom j in the cluster in each time step. Then, in Monte-Carlo manner, the ionization probability for the current time step δt is computed

$$w_j(i \to f) = \frac{I}{8\pi\alpha\omega}\sigma_j \cdot \delta t \tag{4.35}$$

and compared to a random number x uniformly distributed in the range $[0,1)$. $I(t)$ is the instantaneous laser intensity, α the fine structure constant, ω the photon energy and σ_j the ionization cross-section computed in the previous section. If $w_j(i \to f) > x$, then the charge of the ion is increased by $+1$ and an electron with the asymptotic kinetic energy

$$E_{\mathrm{kin}} = \hbar\omega - E_{\mathrm{ip}}(j) \tag{4.36}$$

is created. From now on, it is propagated classically in the field of the laser and of the other electrons and ions in the system. The direction of the initial momentum is random. As already estimated in Section 4.1.2, the electron plasma thermalizes quickly, erasing any anisotropy of the initial angular distribution (Sec. 5.1).

The following two parts will deal with the choice of the model interaction potential and the force computation methods, respectively.

4.2.1   Non-singular approximations of the Coulomb potential

A main concern in molecular dynamics (MD) simulations is the choice of the interaction potential. One wants to avoid those situations, where the electron falls onto an energy state below the quantum-mechanical ground state. With the pure Coulomb potential, if two electrons collide near the nucleus, one of them can fall to a very deep energy and the other one will be ionized with the energy difference. Both effects are unphysical.

One approximation, also used in astrophysical calculations for efficiency reasons, is the so called *soft-core* potential

$$U(r) = -\frac{Z}{\sqrt{r^2 + a^2}} . \tag{4.37}$$

We choose the parameter a according to the ionization potential of the ground state if the electron were bound

$$\lim_{r \to 0} U(r) = -\frac{Z}{a} = -E_{\mathrm{ip}}^{(Z-1)} . \tag{4.38}$$

For rare gas clusters this is on the order of one: $a = 1.7$ for Xe, with $E_{\mathrm{ip}} = 12.1$ eV and $a = 1.4$ for Ar, with $E_{\mathrm{ip}} = 15.75$ eV.

The soft-core, or U-shaped potential becomes harmonic for very low energies, leading to artificial resonances if the frequency of the driving laser field matches the eigenfrequency $\omega_0 = \sqrt{Z/a^3}$.

$$U(r) = -\frac{Z}{a} + \frac{Z}{2a^3}r^2 - \frac{3Z}{8a^5}r^4 + O(r^5). \tag{4.39}$$

a \ Z	1	2	3	4	5	6	7	8
				ω_0 [eV]				
1.4 (Ar)	16.43	23.23	28.45	32.85	36.73	40.24	43.46	46.46
1.7 (Xe)	12.28	17.36	21.26	24.55	27.45	30.07	32.48	34.72

Table 4.1: The eigenfrequency $\omega_0 = \sqrt{Z/a^3}$ of the U-shaped potential for several charge states $1 \leq Z \leq 8$ and parameters a.

The range spanned by the eigenfrequency ω_0 of the U-shaped potential for the charges Z and parameters a encountered in the current work is shown in Table 4.1. Unfortunately, the possible values for ω_0 overlap half of the operation range $12 - 100$ eV of FLASH (Ackermann et al. 2007; Ayvazyan et al. 2002a, 2006). To avoid this drawback we have also considered a V-shaped potential

$$V(r) = -\frac{Z}{r}(1 - e^{r/a}), \tag{4.40}$$

for which $\lim_{r \to 0} V(r) = -Z/a$ also holds. The oscillation frequency for small oscillations diverges however, because $V(r)$ is not differentiable at origin

$$\lim_{E \to -Z/a} \omega_V = \lim_{E \to -\frac{Z}{a}} \frac{\pi}{4}\sqrt{\frac{Z}{a}}\left(E + \frac{Z}{a}\right)^{-\frac{1}{2}} = \infty \tag{4.41}$$

Section 5.2 and Appendix C will investigate the implications of each of these two potentials deeply. The following considerations have a general character and do not depend on the specific form of the potential. A generic form $v(i,j)$ will therefore be used instead

$$v(i,j) = \begin{cases} 1/\sqrt{(\mathbf{r}_i - \mathbf{r}_j)^2 + a^2} & \text{U-shape} \\ (1 - e^{-r/a})/r & \text{V-shape} \end{cases}. \tag{4.42}$$

4.2.2 Force computation algorithms

If the total number of particles does not exceed a few thousands, we compute the forces upon each particle by direct summation. Otherwise we switch over to a hierarchical tree code, introduced by Barnes and Hut in 1986 for astrophysical calculations (Barnes and Hut 1986).

The main advantage of hierarchical tree codes is that the number of explicit force calculations scales as $\mathcal{O}(N \log N)$, as opposed to the simple direct summation, which scales as $\mathcal{O}(N^2)$. Very advanced tree codes, such as Greengard's Fast Multipole
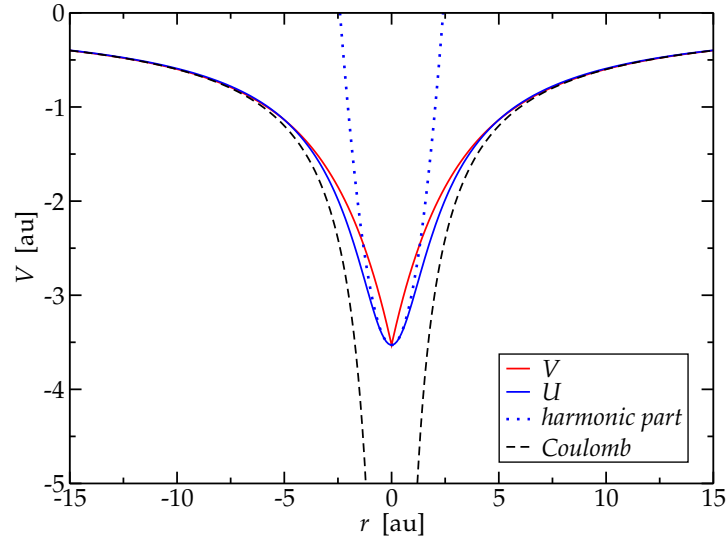
Figure 4.9: Comparison of the U- and V-shaped potentials with the Coulomb potential for $Z = 6$ and $a = 1.7$ (Xe). The dotted line shows the harmonic limit of the U-shaped potential for small oscillations.

Method (FMM) (Cheng et al. 1999; Greengard and Rokhlin 1987; White and Head-Gordon 1994) or Dehnen's $\mathcal{O}(N)$ tree code (Dehnen 2002) scale as good as $\mathcal{O}(N)$ or even less (Dehnen 2002).

The basic idea of these algorithms is to build hierarchical groups of particles. Fig. 4.10 describes the original idea of Barnes and Hut for a 2D system. The top of the hierarchy is represented by a box including all particles in the system. This box is then divided and each particle is assigned to one of the 4 boxes. The process is repeated for each of the new boxes, until each particle is assigned to a box and doesn't share it with any other particle. Empty boxes are discarded.
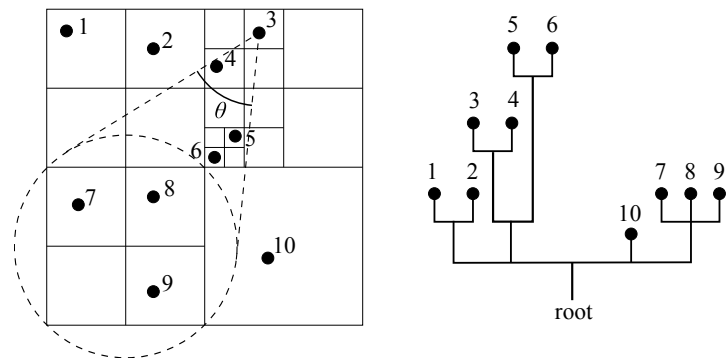

Figure 4.10: Hierarchical, unbalanced grouping of a system of particles as described in Barnes and Hut (1986) and implemented in Barnes (2001). $\theta = 0.9$, meaning that the interaction between particle 3 and each of the particles 7, 8 and 9 will be evaluated.

When the force upon a particle is computed, the hierarchy is traversed from top to bottom. If a box is far enough, then there is no need to go deeper and *look* inside.

Instead, the force upon the particle is computed directly by using the monopole and higher multipoles of the box. The great advantage is that multipoles are computed once, quite easily actually, while the hierarchical structure is being built, and used many times during the force calculation. A box is distant enough if it can be seen under an angle smaller than an angle θ_0 chosen at the beginning of the simulation. $\theta_0 = 0.4$ and multipoles until the quadrupole are a very good compromise (Pfalzner and Gibbon 1996).

Other tree codes avoid deep hierarchies by limiting the minimum number of particles in a box between 6 and 20 (Dehnen 2000). At the same time, they also consider a symmetric multipole expansion, such that the interactions can already be evaluated at a box-to-box level, further reducing the complexity of the algorithm to $\mathcal{O}(N)$ (Dehnen 2000).

We have used Barnes and Hut's method summarized above and maintained by J. E. Barnes as a software package at `http://ifa.hawaii.edu/~barnes/treecode`.

Chapter 5

Adiabatic pumping: clusters in FEL VUV radiation

We have so far presented a new method for describing the interaction of atomic clusters with laser radiation. The photo-ionization of a many-electron atom has been adapted to the cluster environment. The surrounding ions lower the ionization threshold and the plasma formed by the quasi-free electrons trapped in the space charge of the ions screen the attraction of the nucleus, lowering the binding energy of the bound electrons. We have identified those plasma electrons which localize by the ions, screening them effectively. The mean revolution period of their motion about the ions defines the time scale for a coarse-grained dynamics, which makes the link between the classical, deterministic motion of the quasi-free electrons and the rate based, quantum mechanical description of the dynamics of the bound electrons, including photon absorption.

We will illustrate this model with the example of an Ar_{147} cluster illuminated by a 100 fs, $\hbar\omega = 20$ eV and $I = 7 \times 10^{13}$ W/cm^2 laser pulse, similar to those available at the free electron laser facility at DESY, in Hamburg (Ayvazyan et al. 2002a; Wabnitz et al. 2002). The rise of the pulse is very slow on the time scale for plasma equilibration Eq. 4.15, such that the electron plasma is in quasi-equilibrium and will adiabatically follow the pulse envelope. *Real-time*, as well as coarse-grained dynamics during the interaction with the laser pulse will be presented, followed by typical experimental observables, such as ion charge distribution or electron energy spectrum, obtained after propagation for several picoseconds. The second part will analyze the transition to higher photon energy, meanwhile also available (Ackermann et al. 2007; Ayvazyan et al. 2006), more precisely the impact on the way energy can be transferred from light to matter. We will also analyze the role played by the choice of the model interaction potential $v(i,j)$ Eq. (4.42) on these results, i.e. check for artificial resonances. The last section will benchmark the presented framework on very recent, yet unpublished experimental results at 38.7 eV photon energy (Möller 2007).

5.1 Coarse-grained dynamics in Ar_{147}

Rare gas clusters are held together by van der Waals forces, whose most stable structures are the famous Mackay icosahedra (Haberland 1995), having $N = 13, 55, 147, 561 \ldots$ atoms. Doye (1997) provides a large database of lowest energy configurations for Lennard-Jones cluster with sizes $3 \leq N \leq 1000$, normalized to the length of the dimer. The $N = 147$ structure has been calculated by Northby (1987). We have assumed a dimer length of 3.405 Å (Napari and Vehkamaki 2004).

The pulse envelope was chosen to be a $\sin^2$, which is very close to a Gaussian, but has the advantage to have a real zero at the beginning and at the end

$$E(t) = \begin{cases} E_0 \sin^2 \left(\frac{t}{\alpha T} \pi \right) \sin \omega t & \text{if } 0 \leq t \leq \alpha T \\ 0 & \text{otherwise.} \end{cases} \tag{5.1}$$

T is here the full width at half maximum of the laser intensity and $\alpha = 1/(1 - 2\arcsin(0.5^{1/4})/\pi) \approx 2.74$.

Fig. 5.1 shows the main quantities characterizing the interaction, namely energy absorption, ionization degree, plasma temperature and average inter-ionic distance. The first part of the pulse, until ≈ 60 fs, is dominated by photo-ionization. Inverse bremsstrahlung sets in with increasing electron density, to contribute finally two thirds of the total energy absorption. Panel (b) shows the number of ionized electrons per atom. Most of these ($n_{\text{quasi-free}}$) remain trapped in the positive background charge, but evaporate slowly with increasing energy absorption. The number of localized electrons n_{loc} increases initially because of the very fast photo-ionization, but starts to decrease due to the increasing temperature. At $t \sim 140$ fs the pulse reaches maximum intensity, but the temperature starts to decrease due to the rapid cluster expansion and n_{loc} increases. The cluster expansion is described by the rms next-neighbor inter-ionic distance

$$R_{\text{avg}} = \sqrt{\frac{1}{N} \sum_i \min_{i \neq j} \mathbf{r}_{ij}^2} \, . \tag{5.2}$$

The temperature can be defined soon after the first electrons have been trapped in the cluster. A simple estimation, Eq. (4.15), pointed to a thermalization time of roughly $0.8 - 8$ fs if every second ion were ionized at once. In contrast, 10, even 20 fs are needed from this point on to further reach full ionization or double ionization, respectively, as shown in Figure 5.1(b). The velocity distributions in Fig. 5.2 confirm the fast onset of a Maxwell-Boltzmann distribution. The first two distributions were recorded at the times marked by the vertical dotted lines in Fig 5.1, namely at 56 and 202 fs, when the laser has reached 12% and respectively dropped to 30% of the peak intensity. At long expansion times, such as $t \geq 2.44$ ps, the cluster has disintegrated and only the delocalized quasi-free electrons maintain a thermal distribution. The electrons localized about an ion cannot exchange energy with other electrons due to the large inter-ionic separation, such that their velocity distribution is almost frozen. Slow changes still occur, of course, due to the non-vanishing interaction with the dilute, cold electron plasma.
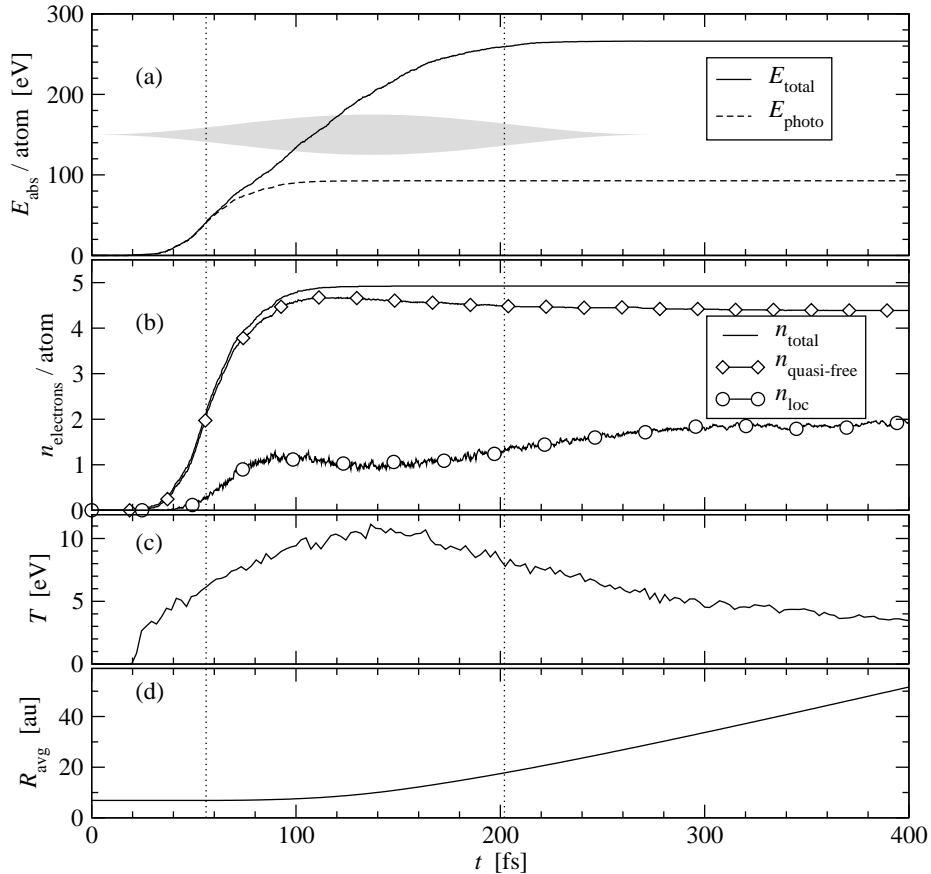
Figure 5.1: Main quantities describing the explosion of Ar_{147} when illuminated by a VUV laser pulse. (a) total energy absorption compared to the contribution of photo-ionization. (b) total number of ionized electrons per atom, with quasi-free and localized quasi-free electrons. (c) the temperature $k_B T = \langle v^2 \rangle / 3$ of the quasi-free electrons. (d) average inter-ionic distance according to Eq. (5.2).

The coarse-grained dynamics introduced in the previous chapter is illustrated in Fig. 5.3 and 5.4 at the example of the central and some surface atom of the cluster. Fig. 5.3 shows the overall evolution over the whole laser pulse. Fig. 5.4 zooms into Fig. 5.3 such that the time intervals T_i become visible. The total energy E^* of the ion and its localized electrons are averaged over the T_i.

Starting in the neutral, lowest energy state, the energy of the ions increases with each ionized electron. The sharp rising steps of the total energy E^* point exactly the ionization events, where a photon has been absorbed and an electron has been released. It should be noted that the height of each step increases with increasing charge and they are higher than the photon energy. This is just a technical artifact leading to a faulty energy balance in Eq. (4.19). Once ionized, an electron is counted as delocalized because its revolution angle is less then 4π. Naturally it is missing from Eq. (4.19) where only localized electrons are considered. The energy of the effective ion seems therefore to have increased by more than $\hbar\omega$ after ionization because the
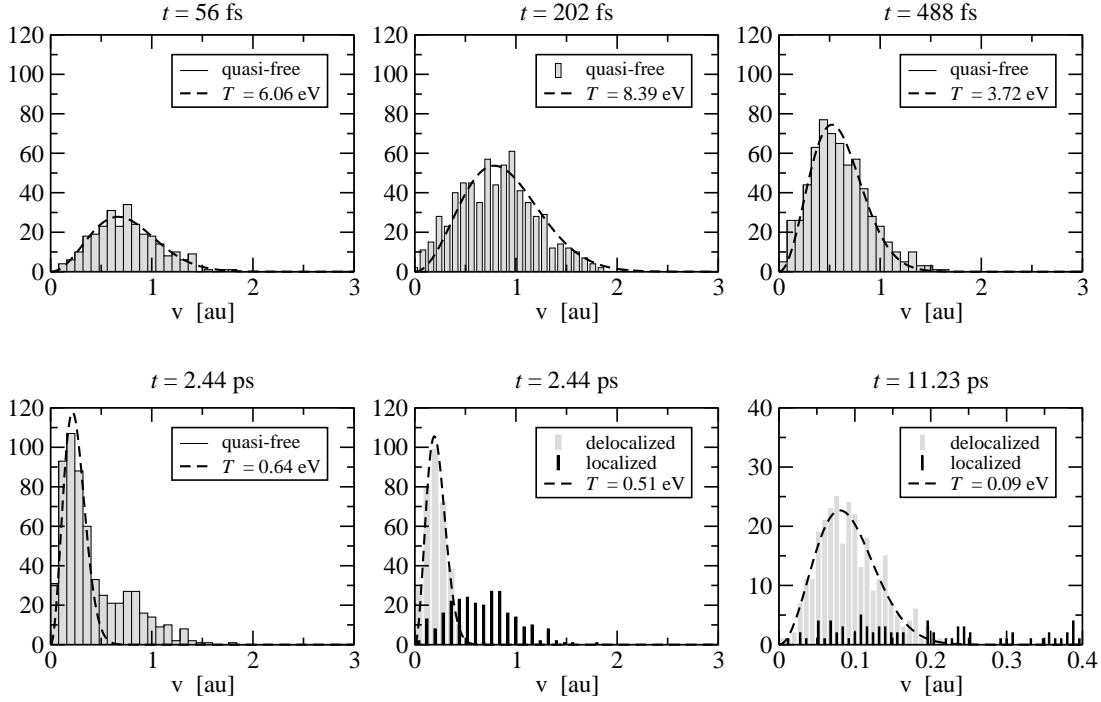
Figure 5.2: Electron velocity distributions in Ar_{147} at several time instants during the interaction with the laser and the subsequent expansion. The time instants of the first two panels, that is $t = 56$ fs and respectively $t = 202$ fs, have been marked by vertical dotted lines in Fig. 5.1. When the cluster has disintegrated, the Maxwell-Boltzmann distribution is restricted to delocalized electrons.

energy of the outgoing electron is fully neglected.

The plateaus of E^* in Fig. 5.3, in Fig. 5.4 also visible for the central atom, correspond to situations of zero localized electrons, as shown by n_{loc} in the same figure. Electron localization is equivalent to relaxation and therefore E^* will quickly decrease as soon as this happens. At the end of the pulse the surface atom is less charged than the central atom. Moreover, electron localization at this ion is rather an isolated event.

The quasi-free electrons neutralize the core of the cluster, leaving the excess of positive charge at the surface. The ions there will experience the highest acceleration and expand faster than the rest. The rapidly increasing inter-ionic distance raises the potential barrier between neighboring ions, preventing further ionization. Moreover, the electron density is much lower, such that the localization of electrons and thus the screening of the atomic orbitals is less effective.

When the cluster disintegration is complete, some of the quasi-free electrons will have recombined with ions. The detector will measure the charge distribution of the ions, as well as their velocities and the velocity of the electrons. Fig. 5.5 shows the final ionic charge and electron kinetic energy distribution after an expansion time of 6.4 ps. The ion charge distribution doesn't change considerably with further expansion. For $E_{kin} > 5$ eV the electron kinetic energy distribution won't change either and can be
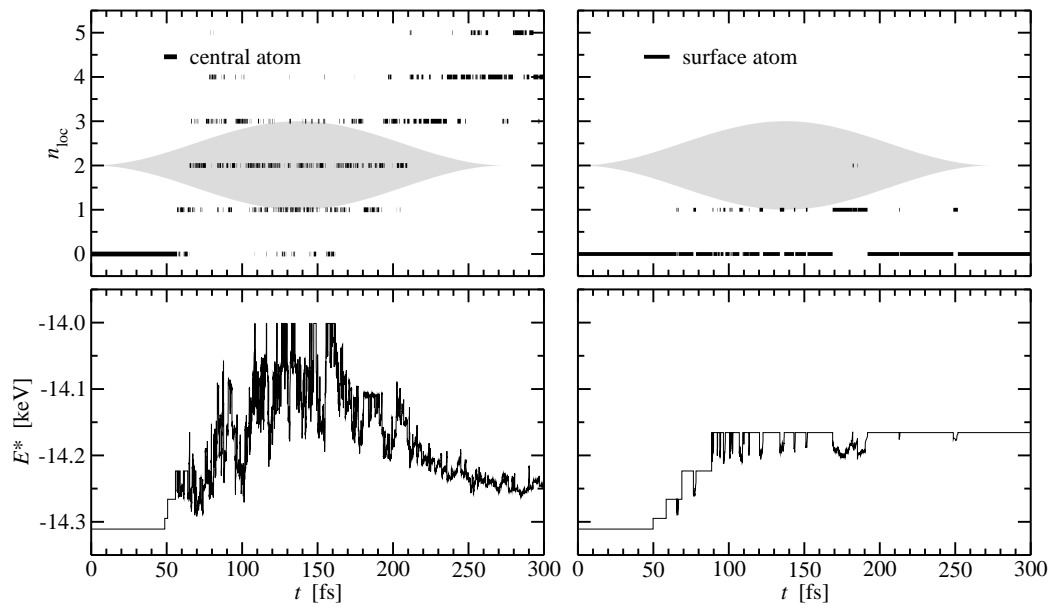
Figure 5.3: Number of localized electrons n_{loc} introduced in Sec. 4.1.3 and total energy E^* as in Eq.(4.19) for two representative ions of Ar_{147}: the central atom and another one on the surface.
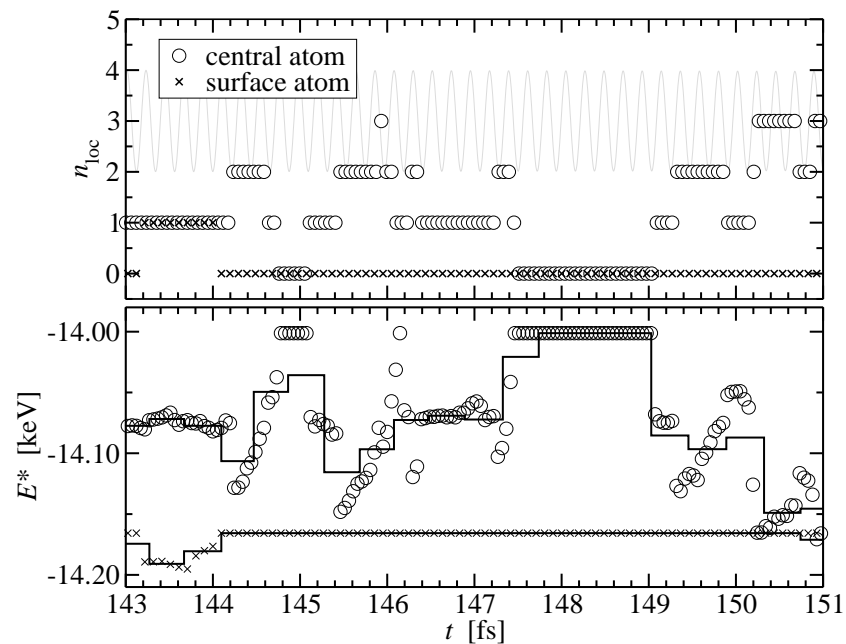

Figure 5.4: Coarse-grained dynamics: zoom of Fig.5.3 at the scale of the T_i. The continuous lines show the average of E^* for both ions over the intervals T_i. The gray line in the top panel depicts the assisting laser field.

fitted by an exponential e^{-E_{kin}/E_0} with $E_0 = 5.4$ eV, thus emphasizing the thermal nature of these electrons. This value in remarkable agreement with the experimental findings of de Castro et al. (2005), who have found a Maxwell-Boltzmann distribution peaking at 5 eV. The agreement should rather be considered in the broader limits of the order of magnitude, since the authors have investigated Ar_{270} clusters exposed to 100 fs, $\hbar\omega = 13$ eV and $I = 4.4 \times 10^{12}$ W/cm^2 laser pulses. That is less power density and smaller cross-section of the two-photon absorption on the one side, but more efficient energy absorption on the other side due to the large cluster size, more kinetic energy impinged on the photo-electrons by the two photons and more efficient IBS due to the lower driving frequency, as it will be shown in the next section.
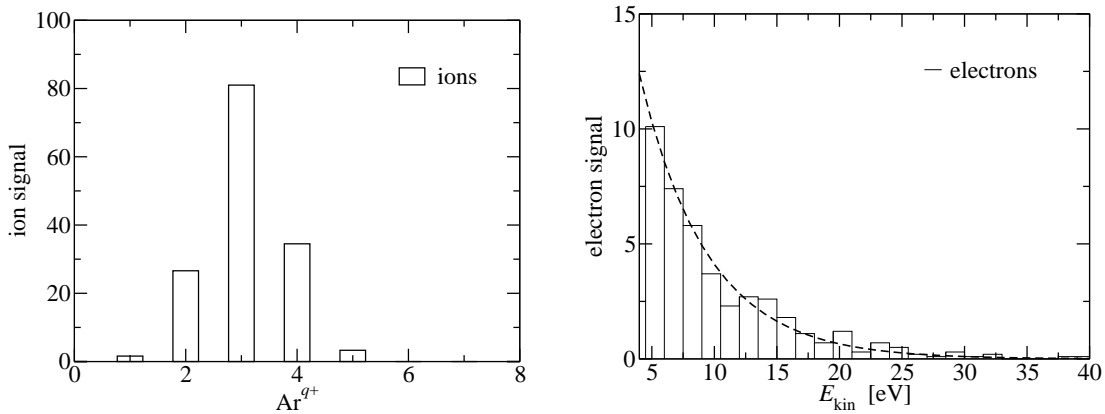

Figure 5.5: Ion charge distribution (left) and electron kinetic energy distribution (right) as measured on the detector after a very long expansion time. The effective ion charges including localized electrons have been displayed. The electron kinetic energy spectrum can be very well fitted by an exponential e^{-E_{kin}/E_0} with $E_0 = 5.4$ eV (dashed line). The propagation time was 6.4 ps

The energy cut off has been chosen on two considerations: on the one hand, the very first photo-electrons which leave the cluster do not thermalize by any means and should therefore not be included in the fit. Their kinetic energy is $E_{kin} = \hbar\omega - E_{ip}(Ar) = 4.76$ eV, just underneath the chosen cutoff.

On the other hand, the cluster expansion cools the electron plasma over several orders of magnitude, as shown in Fig. 5.6. The expansion lowers the trapping potential at the same time, such that the hotter plasma electrons have positive total energy and can leave the cluster. They form a continuous stream of electrons of constantly decreasing kinetic energy, according to the temperature they have evaporated from. Hence the second reason for the cutoff in Fig. 5.5, since slow electrons cannot generally be measured accurately in an experiment (de Castro et al. 2005). They are numerous and saturate the detectors. Moreover, they are sensitive to stray fields always present in an experimental setup, such that their energy would not contain much information anyway, if it could be measured at all.

As shown in Fig. 5.6, the plasma cools by a power law with a coefficient of ≈ 1.1.
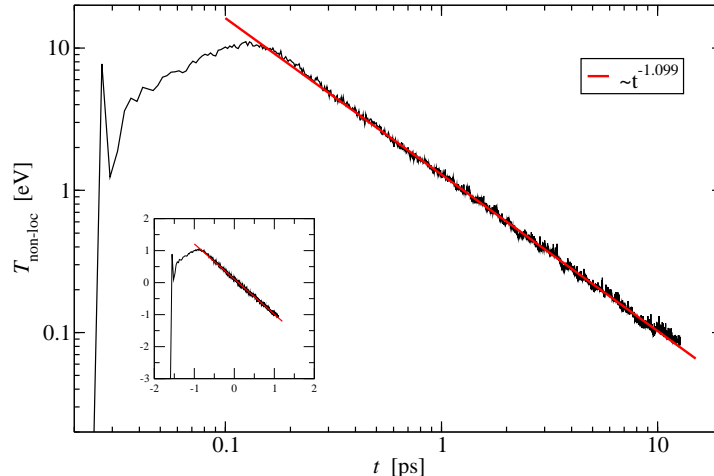
Figure 5.6: The temperature of the delocalized electrons decays as a power law with an exponent of 1.099 over very long expansion times. Inset shows linear fit.

If the equation of state $pV = \nu k_B T$ of an ideal gas is applied, with

$$p \sim \frac{\text{electric field at the cluster boundary}}{\text{surface}} \sim R^{-4},$$

then $k_B T \sim R^{-1} \sim t^{-1}$ since the cluster expands at constant speed now, as shown in Fig. 5.1. The deviation from -1.1 could be attributed to losses via electron evaporation and the long range Coulomb interaction of the electron gas.

5.2 Decoupling the quasi-free electrons in the extreme ultraviolet

Inverse bremsstrahlung has been shown so far to dominate the energy absorption process in the VUV range. It is the response of the quasi-free electrons which, trapped inside the cluster, scatter against all ions at once while being driven by the laser field. The inherent dephasing leads to a net acceleration of the electrons. Electron-electron correlation and screening effects also contribute to the picture. Both the ponderomotive energy U_p and amplitude x_p decrease with the square root of the laser frequency. It should therefore be expected that a weaker coupling at high frequencies diminishes inverse bremsstrahlung until cancellation.

Krainov (2000) has predicted a decay of the IBS heating rate as $\omega^{-8/3}$ for a Maxwell-Boltzmann plasma of ionic density n_i, average ionic charge Z and electron temperature T exposed to a laser field of frequency ω and intensity E^2

$$\left\langle \frac{\mathrm{d}E}{\mathrm{d}t} \right\rangle = \frac{2^{13/6} \, \pi^{3/2} \, Z^{4/3} \, n_i \, \mathcal{E}^2}{15 \times 3^{5/6} \, \omega^{8/3} \, \sqrt{T}} \cdot \frac{\Gamma\left(\frac{1}{3}\right)}{\Gamma\left(\frac{2}{3}\right)} . \tag{5.3}$$

Siedschlag and Rost (2004) have integrated Eq. (5.3) with the time dependent laser intensity $\mathcal{E}^2(t)$ and plasma parameters $n_i(t)$, $Z(t)$ and $k_B T(t)$ extracted from

a microscopical simulation. They have obtained very good agreement with the IBS absorbed energy observed numerically if the average ionic charge $Z(t)$ was reduced by $f = 0.6$ to account for screening effects in the plasma.
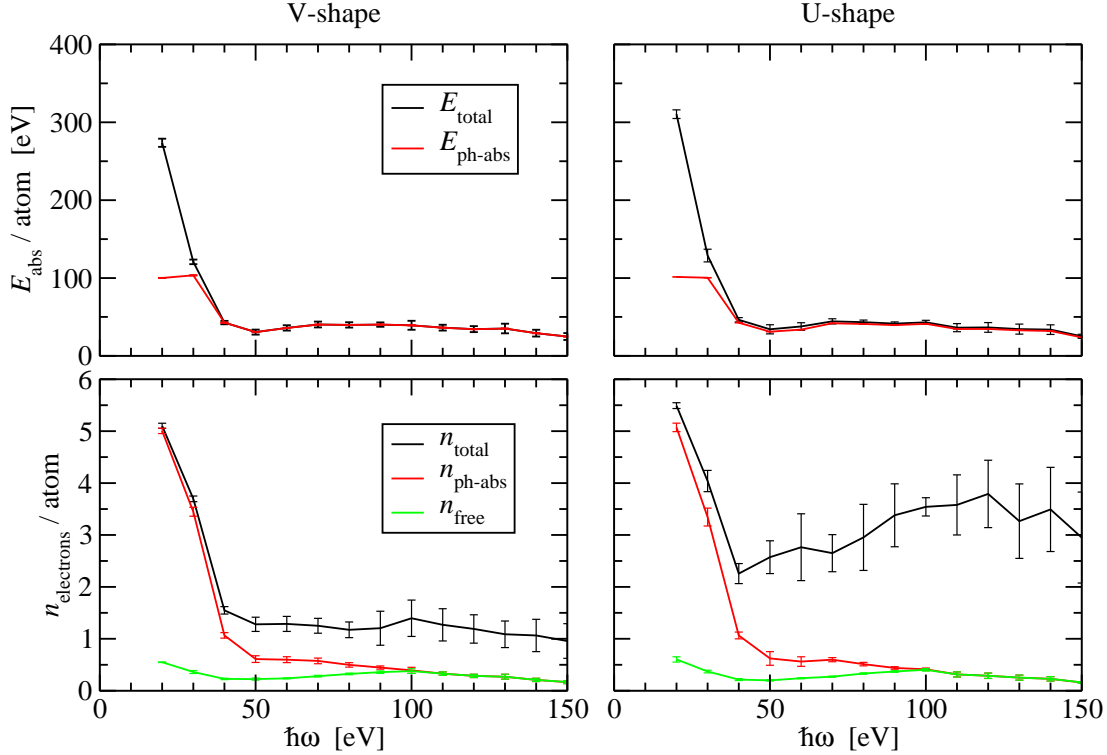

Figure 5.7: Average energy absorption and ionization degree in Ar_{147} illuminated with a 100 fs laser pulse for several frequencies of the latter. Two model potentials, V- and U-shape as defined in Eqs. (4.40) and respectively (4.37) have been used for the interaction of charged particles.

We have investigated the energy absorption and ionization in Ar_{147} as a function of the laser frequency for both model potentials introduced in Sec. 4.2. The results are summarized in Fig. 5.7. Both potentials show similar behavior, with dominant inverse bremsstrahlung at lower frequency and almost non-existent beyond 40 eV. At high frequencies photo-ionization is solely responsible for energy absorption. The minimum at 50 eV owes to the Cooper minimum of the cross-section (Fig. 4.2). The number of photo-ionized electrons is almost identical for both potentials. Differences arise from the ionization "bias" of the U-shaped potential. By construction, $U(r) \leq V(r)$ for all r, see also Fig. 4.9, such that $U(r)$ will always yield lower ionization thresholds. This bias towards ionization can be observed much better not at the photo-ionization curve, but at the number of field-ionization events, given by the difference $n_{total} - n_{photo}$ in the lower panels of Fig. 5.7. Fluctuations of the plasma micro-field make isolated ionization events possible without absorption of a photon. Though present for both potentials, these events are obviously more numerous for $U(r)$.

Photon energies larger than 40 eV show the main pitfall of our approach. In this

range not all atoms in the cluster will have been ionized by the end of the laser pulse due to the very small cross-section. Collisions between neutral and charged atoms become possible, because neutral atoms are fully transparent to the charged ones. We do not account for the direct interaction of the nuclei if their charge is no longer effectively screened by the electron cloud, as it happens when two atoms come too close to each other and their electron clouds overlap. An approaching charged ion can thus field ionize electrons off the valence orbital of a neutral atom by lowering the potential barrier. By the time the heavy ions start to repel each other, they will have come so close to each other, that they will have engaged a closed loop of field ionization events, where they reciprocally lower the potential barrier. $U(r)$ is especially sensitive here, as it generally yields lower ionization thresholds.
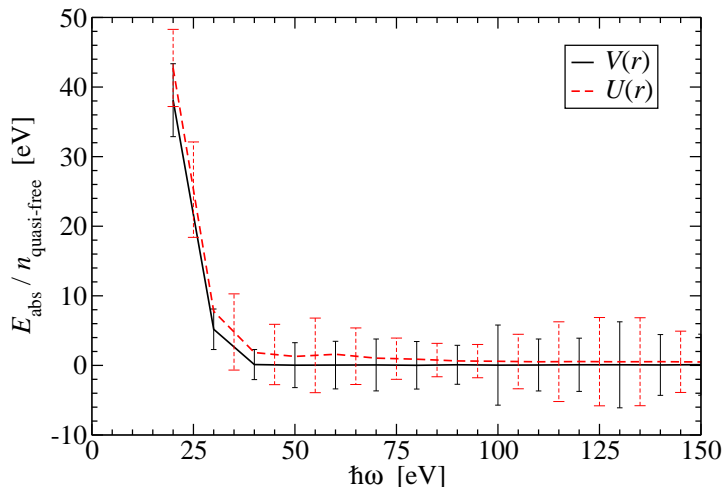

Figure 5.8: Comparison of E_{IBS} for Ar_{147} as a function of the laser frequency for the two different model potentials, $U(r)$ and $V(r)$. E_{IBS} has been normalized to the number of quasi-free electrons.

Resonance effects, meant to be prevented by the choice of $V(r)$ in Sec. 4.2, can be out-ruled as a cause for the excess electrons when $U(r)$ is used. The main observables of the experiment, the total energy absorption or the number of outer-ionized electrons are identical for both $U(r)$ and $V(r)$. The fact emphasizes once more the very weak coupling between the laser field and the quasi-free electrons at high frequencies. Although more electrons are available with $U(r)$, they have no effect on the outcome. Fig. 5.8 shows E_{IBS} renormalized to the number of active (quasi-free) electrons. Although $U(r)$ seems slightly more effective, the effectiveness stays well within the error bars.

The cross-over of $n_{\mathrm{ph\text{-}abs}}$ and n_{free} at $\hbar\omega = 100$ eV in Fig. 5.7 marks the maximum photon energy for which a plasma can form. Beyond that energy all photo-electrons leave the cluster. The limit can be shifted by varying the laser intensity, thus the total space charge, as shown in Fig. 5.9. At the lower intensity $I = 4.9 \times 10^{13}$ W/cm^2 the maximum photon energy for plasma formation drops to 90 eV, but at the ten fold intensity it is already larger than 150 eV. For $I = 9.8 \times 10^{14}$ W/cm^2 inverse
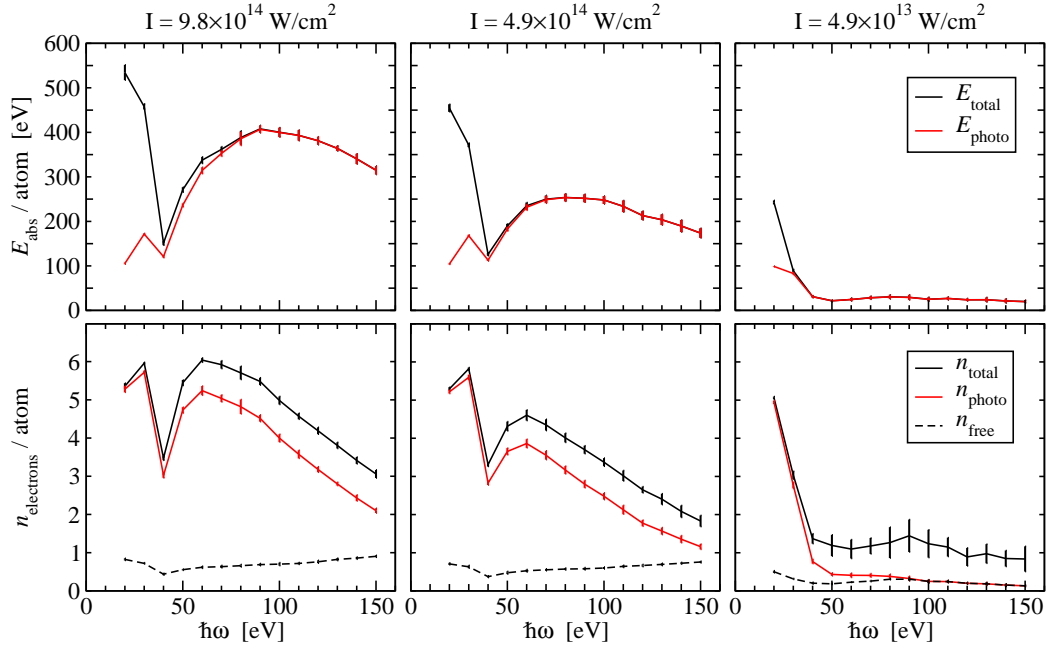
Figure 5.9: Absorption spectra and ionization degree of Ar_{147} clusters for different laser intensities. At low frequencies the cluster is fully ionized and the energy absorption is dominated by inverse bremsstrahlung, which becomes rapidly irrelevant with increasing frequency.

bremsstrahlung is present up to 90 eV.

The minimum for photo-absorption also shifts with laser intensity. At low intensities, the average charge is +1 or less beyond 40 eV, such that photo-absorption is dominated by neutral Ar and the minimum appears at the Cooper minimum. The average charge increases to +3 at high intensities, such that neutral Ar saturates and photo-absorption is dominated by the higher charges. The minimum is shifted to down 40 eV.

A detailed investigation of the model potentials $U(r)$ and $V(r)$ for a single electron driven by a laser a field, as well as an analysis of the Krainov scaling law for dense, highly collisional correlated plasma are presented in Appendix C.

5.3 Sequential cluster ionization

November 2005 another stage of the FEL at DESY became operational providing radiation down to 13 nm and peak power densities up to 10^{14} W/cm^2 (Ayvazyan et al. 2006). Fig. 5.10 shows results of first experiments, where argon clusters containing on average $\langle N \rangle \approx 900$ atoms were exposed to 25 fs and 32 nm ($\hbar\omega = 38.75$ eV) FEL pulses with power densities varying from 1.18×10^{13} W/cm^2 up to $I = 6.23 \times 10^{13}$ W/cm^2 (Möller 2007). The main peaks at a time of flight of ≈ 50 ns can be attributed to the Ar $3p$ electrons. The data have been obtained by filtering the electron spectra according to selected energy windows of the FEL pulse.

Other peaks in the spectra are therefore either due to insufficient statistics, or a proof for sequential escape of electrons from the cluster.
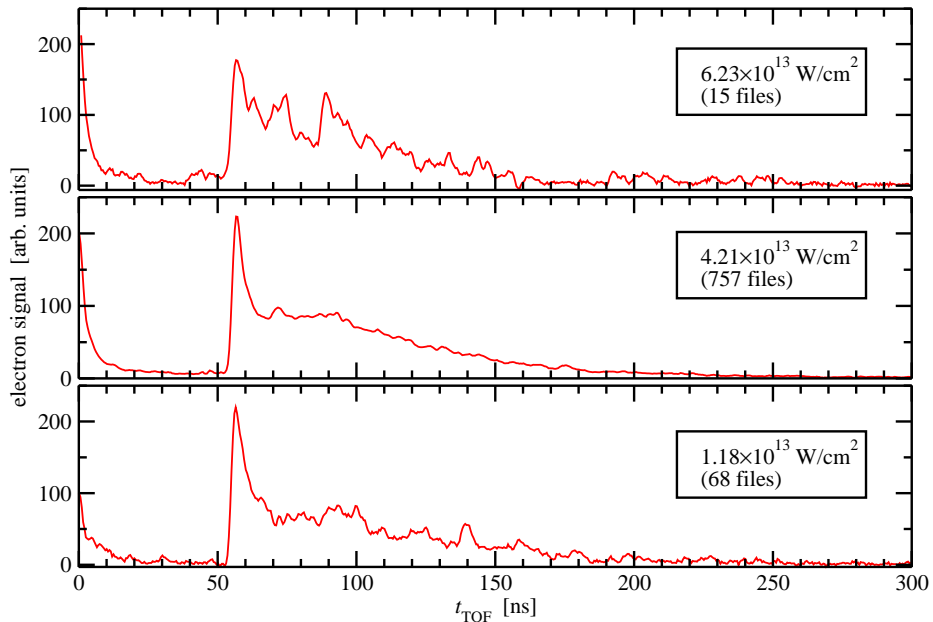

Figure 5.10: Electron time of flight spectra for $Ar_{\langle 917 \rangle}$ clusters exposed to FEL 25 fs pulses at 32 nm. The spectra have been filtered according to the instantaneous energy in the FEL pulses. From Möller (2007).

The photon energy $\hbar\omega = 38.75$ eV is close to the Cooper minimum of Ar (Fig. 4.2). The photo-ionization rate is here very low, such that the electrons leave the cluster one by one. In a single cluster measurement they would be observed as isolated peaks in the TOF spectra, as the cluster charge increases with each photo-ionized electron, slowing the next one down.

No electrons with time of flight shorter than that of the Ar $3p$ main line have been observed for any of the depicted intensities. They correspond to kinetic energies higher than that of the Ar $3p$ electron and are normally a signature for thermionic emission. Their absence implies that there is no other energy absorption mechanism, in particular no inverse bremsstrahlung, besides photo-ionization. These were also our findings in the previous section for four times longer and slightly stronger pump pulses.

We have performed calculations with similar parameters for a quantitative comparison. Icosahedral Ar_{923} clusters have been exposed do 30 fs pulses with $\hbar\omega = 38.64$ eV for two intensities, $I = 4.9 \times 10^{13}$ W/cm^2 and 9.8×10^{13} W/cm^2, respectively. The recorded electron spectra have been averaged over 70 ensembles and are shown in Fig. 5.11 along with the experimental results for 6.23×10^{13} W/cm^2. The time axis of the spectra was normalized to a single point, the position of the Ar $3p$ maximum. The yields have been normalized such that the maxima stay in the same ratio to each other as the corresponding pump pulse energies do. The agreement is almost perfect. The low energy tails, corresponding to longer times of flight, decay at
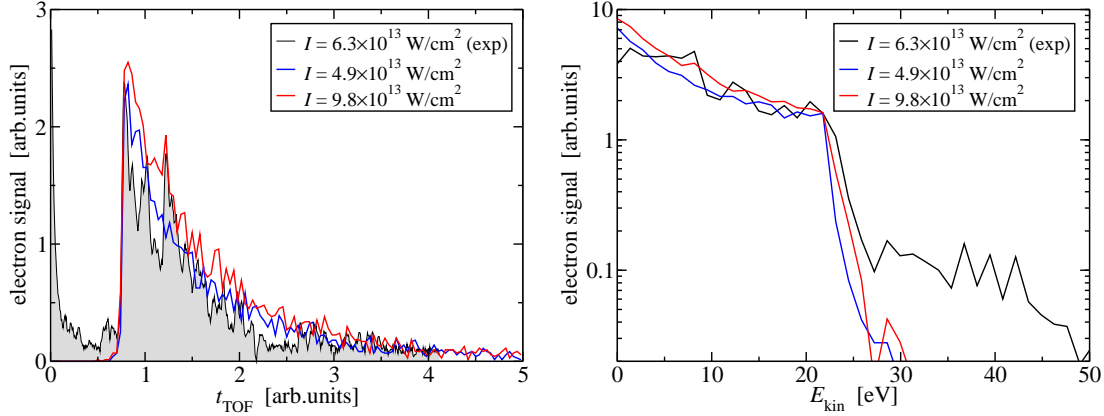
Figure 5.11: Comparison of experimental and theoretical electron spectra of Ar clusters exposed to 38.7 eV FEL radiation. Left, time of flight, right kinetic energy spectra. The black lines (shaded gray on the left) correspond to the upper panel of Fig. 5.10. The red and blue lines show our findings for Ar_{923} icosahedral cluster exposed to 38.64 eV, 30 fs pulses with $I = 9.8 \times 10^{13}$ W/cm^2 and respectively $I = 4.9 \times 10^{13}$ W/cm^2. The time axis was normalized to a single point, the maximum of the Ar $3p$ lines. The yields were normalized such that the intensities of the Ar $3p$ lines stay in the same ratio to each other as the respective pump pulse energies do.

the same rate. They are a superposition of sequential production of electrons during the laser pulse and evaporation of quasi-free electrons from the cluster plasma. As shown in Fig. 5.12, only a small fraction of the photo-ionized electrons are actually outer ionized, despite the low cross-section, short excitation time and Lucite low intensities. Although the cluster is not fully ionized, it is large enough such that the absolute charge can trap electrons to form a plasma. Thermal electrons evaporate from this plasma during the subsequent expansion and fragmentation, producing the characteristic exponential decay of the spectrum in the low energy range, Fig. 5.11, right. The decay constant is approximatively $E_0 = 10.6$ eV.

With less power density, the Ar $3p$ main line is emphasized with respect to the rest of the spectrum. As Fig. 5.12 suggests, as long as $I > 7.1 \times 10^{12}$ W/cm^2, the laser intensity has no impact on the photo-electrons actually leaving the cluster. It merely changes the number of photo-electrons which remain trapped and form a plasma. With less electrons in the plasma, less electrons can evaporate and the thermionic tail in Fig. 5.10 vanishes. The sharp features observed in Fig. 5.10(b,c) could therefore be attributed to the spatial distribution of clusters in the laser focus, where the main Ar $3p$ line could be amplified by clusters in the outer region of the focus. The reason why they cannot be seen in Fig. 5.10(a) may simply be bad statistics, where specific parts of the focus space have not been sampled. Only 15 shots are shown there, as opposed to 750 in (b) and 68 in (c). The cluster size distribution plays a similar role. In large clusters the energy difference between two consecutive photo-electrons is smaller due to the larger rms distance to an already ionized atom. This would
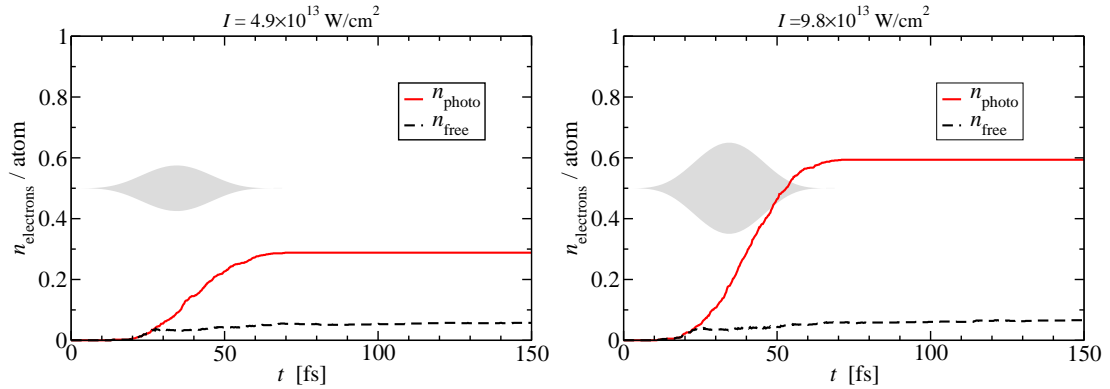
Figure 5.12: Average photo- and outer ionization in Ar_{923} exposed to $\hbar\omega = 38.64$ eV, 30 fs laser pulses for two intensities, $I = 4.9 \times 10^{13}$ W/cm^2 (left) and respectively $I = 9.8 \times 10^{13}$ W/cm^2 (right).

again amplify the main Ar $3p$ peak with respect to the rest of the spectrum. The topic requires obviously more investigation, as well as more experimental data, and will be subject to future work.

Chapter 6

Probing the cluster dynamics with attosecond laser pulses

Time-resolved analysis of the laser-cluster interaction, as performed in the previous chapter, is not accessible experimentally. In the following we will present a scheme where an additional attosecond laser pulse in the extreme ultraviolet regime (XUV) can be employed to probe the incoherent many-particle dynamics inside the cluster.

Applications of attosecond pulses have been so far limited to initiating single- or few-electron coherent dynamics in a series of elementary processes, which will be summarized in first section. Section two will then deal with the main concerns involved with extending their applicability to probing incoherent, many-particle dynamics in a cluster. Finally, Ar_{13} clusters will be probed while pumped by 100 fs VUV pulses, similar to those available at FLASH and employed in the previous chapters.

The method would also help to shed more light on the underlying mechanisms of energy absorption, since they are still controversial. Several theoretical works (Bauer 2004; Georgescu et al. 2007a; Jungreuthmayer et al. 2005; Rusek and Orlowski 2005; Santra and Greene 2003; Siedschlag and Rost 2004) that followed the original Hamburg experiment (Wabnitz et al. 2002) have reproduced its main observables, that is average energy absorption and ionic charge distribution. They have also identified inverse bremsstrahlung as the main absorption mechanism, but they disagree concerning the origin of its efficiency. To be specific, the transient charge of the ions in the cluster varies from very high, such as 8+ with Siedschlag and Rost (2004) or 6+, as encountered in the previous chapter, down to very low, such as +2 with Santra and Greene (2003).

In particular, Santra and Greene (2003) find effective IBS heating with weakly charged ions due to the use of a strongly singular effective nuclear potential for the electron-ion interaction

$$V_i(r) = -\frac{1}{r}[i + (Z - i)e^{-\alpha_i r}]e^{-r/\lambda_D} . \tag{6.1}$$

Colliding electrons experience thus the full nuclear charge Z as they penetrate the ion. i represents in this case the ionic charge state and α_i parameterizes the screening of the electron cloud, whereas λ_D describes screening due to the electron plasma.
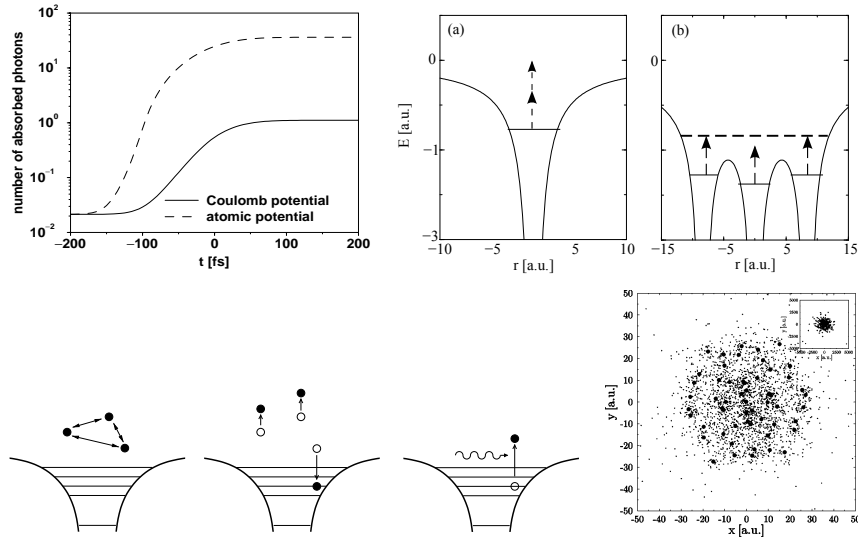
Figure 6.1: Main theoretical proposals for the mechanisms leading to the unexpectedly high energy absorption in rare gas clusters irradiated by VUV laser fields (Wabnitz et al. 2002). (top left): IBS due to highly singular effective potential, from Santra and Greene (2003); (top right) IBS due to high density of the electron nano-plasma, from Siedschlag and Rost (2004); (bottom left) many-body recombination (MBR), from Jungreuthmayer et al. (2005); (bottom right) Thomas-Fermi approach with nine active electrons, from Rusek and Orlowski (2005).

α_i were chosen in such a way that the ionization potential of the Xe $5p$ electron in $V_i(r, \lambda_\mathrm{D} = \infty)$ was identical to the experimentally known value. IBS is calculated over quantum free-free transition cross-sections for delocalized, inner-ionized electrons in the infinite periodical extension of V_i. The result shows 20-fold absorption over the simple Coulomb potential $-\frac{i}{r}$, see also Fig. 6.1 top left.

6.1 Coherent few particle experiments with attosecond pulses

The development of strong, phase-stabilized, few- to single-cycle, infrared laser fields (Brabec and Krausz 2000; Goulielmakis et al. 2004) marked the beginning of attosecond physics. Strong few-cycle pulses have been used to control the motion of the electron with sub-femtosecond precision, as it is ionized (Kienberger et al. 2002), accelerated by the field and then driven back to re-collide with the mother atom or molecule (Itatani et al. 2005; Niikura et al. 2002, 2003; Zeidler et al. 2005). When this happens, it can recombine to release a photon, it can ionize a second electron or just scatter off and re-collide later.

Filtering the high harmonics generated by the re-colliding electron upon recombination has been used to generate first sub-femtosecond pulses less than a decade ago (Hentschel et al. 2001). Pulse durations as short as 170 as at $\hbar\omega \approx 100$ eV have

been reported recently (Lopez-Martens et al. 2005; Schultze et al. 2007). When the electron is ionized from a molecule, it can be used to image the molecular orbital by studying the emitted HH spectrum emitted at re-collision (Itatani et al. 2004; Torres et al. 2007). The spatial resolution obtained corresponds to the wavelength of the re-colliding electron $\sim 1 - 2$ Å. The temporal resolution is given by the time the electron needs to return, that is roughly one half cycle period, 1.3 fs.
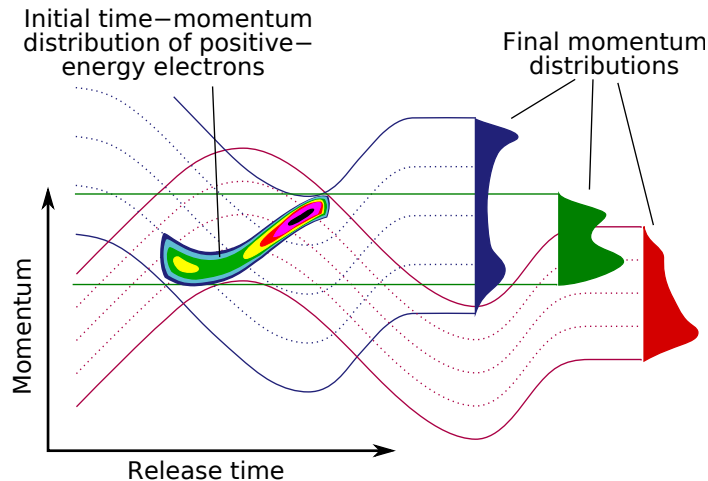

Figure 6.2: Principle of the atomic transient recorder. A sudden excitation places an electron wave packet in the continuum. A near-infrared (NIR) field encodes the time in the drift momentum of the electrons according to Eq. (6.2). If the final momentum distribution is measured for several delays between the pump and the NIR probe, the full time- and momentum structure of the electron wave packet can be retrieved. From Kienberger et al. (2004).

Experiments with attosecond laser pulses have so far only dealt with coherent dynamics of single to few electrons. The attosecond pulse initiates a sudden excitation of the system, whose relaxation is probed with a femtosecond, weak near-infrared (NIR) pulse. The probe pulse accelerates the electrons right from their emergence in the continuum at time t_i with momentum $\mathbf{p}_0$, encoding the instantaneous phase of its vector potential, hence the time, in the final momenta of the electrons

$$\mathbf{p}_{\text{final}} = \mathbf{p}_0(t_i) + q\mathbf{A}(t_i). \qquad (6.2)$$

The scheme, also known as attosecond streaking (Drescher et al. 2001), is depicted in figure 6.2. If no external field is present, the wave-packet moves along the lines of constant momentum, yielding the field-free momentum distribution (in green). In the presence of an electromagnetic field, the wave-packet moves along the lines of constant canonical momentum $\mathbf{p}(t) + q\mathbf{A}(t)$ (red and blue). If several such tomographic projections are recorded for various delays between the excitation and the probe field, an "atomic transient recorder" is obtained (Kienberger et al. 2004), which reconstructs the original time-momentum distribution of the electron emission.

First streaking experiments have studied electron wave-packets created via photo-ionization or Auger-decay. In the former, the ionization of a valence electron by an

attosecond XUV pulse was traced. The intensity profile of the XUV pulse itself was thus retrieved, confirming the sub-femtosecond duration (Hentschel et al. 2001) and the light-field oscillations of the long, 30 fs NIR probe pulse were recorded (Gouliel-makis et al. 2004; Hentschel et al. 2001). Other studies have observed the decay of a core whole created by an XUV pulse and the decay time was measured (Drescher et al. 2002). Strictly speaking, the additional probe was superfluous in both experiments. Due to the coherent nature of the single electron dynamics, a full measurement in the energy domain would have sufficed for the determination of time structure. Time and energy are canonical conjugate variables and thus Fourier related. In this spirit, strong-field ionization of argon with a few-cycle pulse was used to implement the equivalent of a double-slit experiment in the time domain (Lindner et al. 2005).

6.2 Prerequisites for probing many-particle dynamics

In contrast to the above mentioned experiments, coherence is lost early in a cluster due to dissipation of energy along many degrees of freedom, resulting into cluster expansion. Their complete determination, as performed currently in the reaction microscope (Dorner et al. 2000; Ullrich et al. 2003), could in principle be imagined, but the number of particles is simply too large, thus not possible.
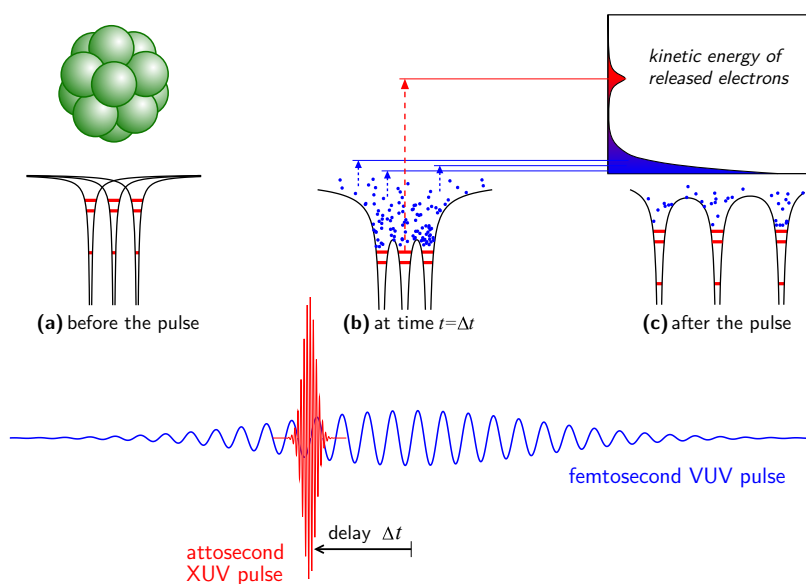

Figure 6.3: Scheme for a slow pump fast probe experiment with rare gas clusters. A VUV femtosecond laser is shone upon a rare gas cluster and creates a dense nano-plasma by exciting many electrons per atom into inner-ionized states. An attosecond XUV laser pulse of high photon energy probes the charge of the atoms by ionizing valence electrons, whose kinetic energy at the detector is a direct measure for the initial ionization potential, and hence for the original charge of the atoms.

We reverse the role of the laser pulses and suggest a long slow pump and a short fast probe. The cluster is excited by a femtosecond VUV pulse and probed by an attosecond XUV pulse. The latter creates fast photo-electrons which, much faster than any other electrons in the system, will be able to leave the cluster in a short time with almost no interaction. The kinetic energy of these electrons at the detector will bare the imprint of the instantaneous ionization potential at the atom, as sketched in Fig. 6.3. The slower they are, the higher the charge of the ions. If the delay between the VUV and the XUV pulse is varied, the time-resolved charging of the cluster can be retrieved.

Employing electrons to read out the charge of the ions raises several issues

1. the XUV photo-electrons should be clearly distinguishable from the other electrons,

2. inelastic collisions with ions and electrons should be kept to a minimum,

3. their kinetic energy should uniquely identify the charge state of the parent ion.

We will address these issues for those excitation parameters characteristic for FLASH and studied in the previous chapter, that is $T = 100$ fs, $\hbar\omega_{\mathrm{vuv}} = 20$ eV and $I_{\mathrm{vuv}} = 7 \times 10^{13}$ W/cm^2. The VUV photo-electrons carry at most 4.5 eV of kinetic energy for Ar$_N$ or 7.9 eV for Xe$_N$. The large majority of the electrons in the continuum have evaporated from the cluster nano-plasma and show an exponentially decaying distribution with energies well below 40 eV (see Fig. 5.5). Issue number one can therefore be solved by increasing the photon energy. Observation of Ar^{5+}, for which $E_{\mathrm{ip}}(\mathrm{Ar}^{5+}) = 91$ eV, demands thus for at least 130 eV of photon energy. Current high harmonic sources operate already at $\hbar\omega \approx 100$ eV (Drescher et al. 2001, 2002; Schultze et al. 2007) and photon energies up to keV are considered (Agostini and DiMauro 2004), since the high-harmonic cutoff $E_{\mathrm{ip}}+3.17U_{\mathrm{p}}$ increases with the squared wavelength of the generating field. At 800 nm and $I = 10^{15}$ W/cm^2, it lies already at 220 eV. The conversion efficiency would decrease strongly in this case due the increased spread of the re-colliding electron wave-packet, but it is not a handicap for our probe scheme, as it will soon become clear.

The second issue can be addressed with smaller clusters, to decrease the distance the electrons travel on their way out of the cluster with respect to the mean-free path. Higher photon energy helps here also, because the electrons' mean-free path in the cluster scales roughly as E_{kin}^2 (Spitzer 1962, §5.3), meaning that they would not only leave the cluster fast, but also collision free.

Though quasi-free electrons represent indeed an obstacle for the XUV photo-electrons, they do not couple to the XUV radiation because they are delocalized in the cluster volume. It has already been shown in Section 5.2, that at the afore mentioned laser frequency $\hbar\omega = 130$ eV inverse bremsstrahlung is irrelevant for the total energy absorption. The ponderomotive amplitude is negligible here $x_{\mathrm{p}} = 7.4 \times 10^{-3}$ au = 0.39 pm, even with a high power density $I = 10^{15}$ W/cm^2.

That quasi-free electrons do not couple to XUV radiation is desirable for issue number three, since only photo-ionization of bound electrons can deliver information
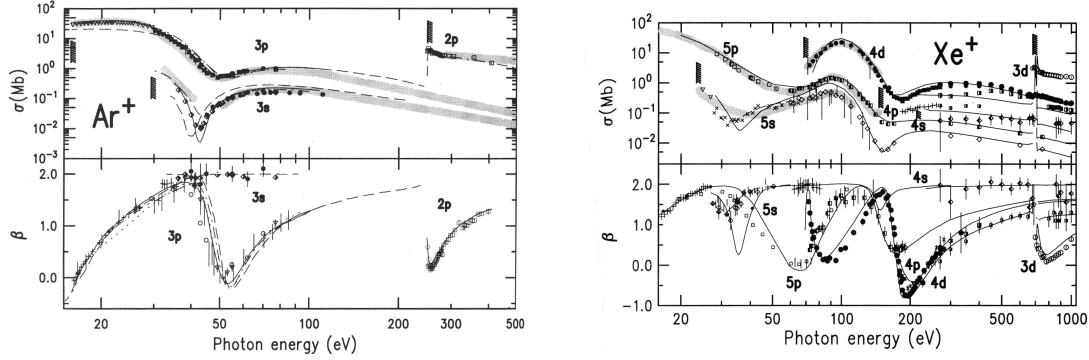
Figure 6.4: Orbital resolved photo-ionization cross-sections for Ar (left) and Xe (right). From Becker and Shirley (1996).

about the charge of the atoms. A one-to-one relationship of the escape kinetic energy to the charge of the atom is only possible if electrons from deeper bound orbitals cannot be mistaken for electrons from higher orbitals of higher charged ions. The situation is illustrated in Fig. 6.4 for Ar and Xe. For the latter at least three orbitals can be ionized with the above mentioned minimum photon energy $\hbar\omega = 130$ eV, namely $5p$, $5s$ and $4d$ with E_{ip} of 12.1, 22 and 64 eV, respectively. A Xe $4d$ electron could thus be mistaken for a Xe^{5+} $5p$ electron, with $E_{ip}(Xe^{5+}, 5p) = 63$ eV. Ar represents a much better target in this energy range. Only the $3s$ and $3p$ orbitals can be ionized at 130 eV. The threshold for $2p$ is already higher than 250 eV.

6.3 Attosecond resolved charging of Ar_{13}

We have performed calculations on Ar for the smallest icosahedral structure Ar_{13}. The pump pulse was $\hbar\omega_{vuv} = 20$ eV, $I_{vuv} = 7 \times 10^{13}$ W/cm^2 and $T_{vuv} = 100$ fs. For the XUV probe pulse we chose $\hbar\omega_{xuv} = 150$ eV, $T_{xuv} = 500$ as and $I_{xuv} = 1.4 \times 10^{15}$ W/cm^2. The energy of the XUV pulse was chosen in such way, that the probe does not perturb the cluster dynamics. No more than one electron per cluster should be created. The photo-ionization cross-section of the neutral Ar at $\hbar\omega = 150$ eV is ≈ 0.47 Mb. The probability to ionize a single atom under these circumstances is $w = 16.85 \times 10^{-3}$ and to ionize a single atom in the whole cluster $W(1) = \binom{N}{1} w^1 (1-w)^{N-1} \approx 0.18$. The probability to ionize two atoms during the XUV pulse is $W(2) = \binom{N}{2} w^2 (1-w)^{N-2} \approx 0.018$. If, on the other hand, the probe intensity is too low, it can be compensated with higher repetition rate.

The two pulses interact with the cluster ions in exactly the same way, as described in Chapter 4. If by the end of the XUV pulse no XUV photo-electron has been created, the simulation is aborted and another one is started. It would be useless to continue propagating, since we are only interested in kinetic energy spectra. As mentioned above, only 1 run out of 5 will produce an XUV photo-electron and 1 out

of 50 will produce two. If at least one is produced, then we continue propagating for 55×10^3 au, that is ≈ 1.34 ps, to ensure the probe electrons have left the system. The cluster will have completely disintegrated during this time, to an average inter-ionic distance $R_{\mathrm{avg}} = 21$ nm from originally 3.4 Å. A 50 eV fast electron will have travelled 5.5 μm during this time. The field of the XUV pulse is neglected during the particle propagation due to the small ponderomotive amplitude x_{p} and the small pulse duration.

Finally, the kinetic energy spectra are recorded. The XUV part of the spectra is additionally convoluted with the spectral profile of the XUV pulse, which for a $\sin^2$ envelope (5.1) corresponds to

$$
\begin{aligned}
E(\omega) &= \frac{1}{2\pi} \int_{-\alpha T/2}^{\alpha T/2} E_0 \cos^2 \frac{\pi t}{\alpha T} e^{i(\omega - \omega_0)t} \mathrm{d}t \\
&= \frac{2\pi E_0}{4\pi^2 - (\omega - \omega_0)^2 \alpha^2 T^2} \cdot \frac{\sin(\omega - \omega_0)\alpha T/2}{\omega - \omega_0},
\end{aligned}
\tag{6.3}
$$

where $\alpha = 1/(1 - 2\arcsin(0.5^{1/4})/\pi) \approx 2.75$ and the zero centered $\cos^2$ representation of the intensity profile was used. The full width half maximum bandwidth can be estimated numerically to be

$$
\Delta\omega \approx \frac{2 \times 4.525}{\alpha T} \approx \frac{3.295}{T},
\tag{6.4}
$$

which for $T = 500$ as yields $\Delta\omega \approx 4.48$ eV.

Kinetic energy spectra of the released electrons are summarized in Fig. 6.5 for several delays between the pump and the probe pulse. The dashed lines correspond to the escape energies of electrons photo-ionized from isolated Ar ions and provide the reference for the average ion charge in the cluster. For very small delays, when the attosecond pulse comes before the VUV pulse, the neutral argon is probed. The characteristic peaks of the $3s$ and respectively $3p$ orbitals, separated by 15 eV are obtained. They are shown separately in Fig. 6.6(b). The surface of the peaks, that is, the cross-section for photo-ionization is influenced solely by the occupation number of each orbital at this photon energy. The line broadening is caused by the bandwidth $\hbar\Delta\omega$ of the XUV laser.

With increasing delay the intensity of the VUV pulse increases and cluster ionization sets in. First just as a broadening and a slight red shift of the peaks due to the increasing cluster charge, from $\Delta t = -105$ fs onward as a strong shift towards higher charges as ionization gains momentum. The shape of the spectrum stabilizes around $\Delta t = -70$ fs, when ionization of the atoms saturates. The shift continues, though at lower pace, due to electron evaporation (see also Fig. 5.1) and hence increasing space charge.

The low energy part of the spectrum, displayed in detail in Fig. 6.6(a), does not change with the delay. These are the electrons set free by the VUV laser. Their thermal origin is emphasized by the exponential fit with the equivalent temperature $E_0 = 3.3$ eV, in agreement with the previous findings for Ar_{147} (Fig. 5.5) and experimental results (Laarmann et al. 2005). The temperature E_0 is lower due to the smaller cluster size and correspondingly less efficient energy absorption.
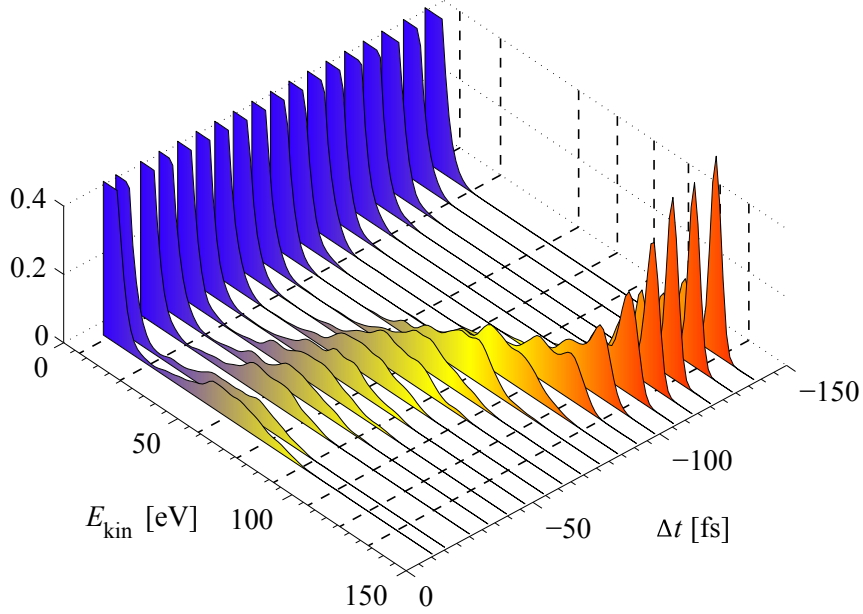
Figure 6.5: Kinetic energy spectra of the outer ionized electrons for several delays of the XUV probe with respect to the VUV pump. The dashed lines correspond to the escape energies $\hbar\omega - E_{\text{ip}}(\text{Ar}^{q+})$ of electrons ionized from isolated Ar ions and provide the reference for the ionization degree.
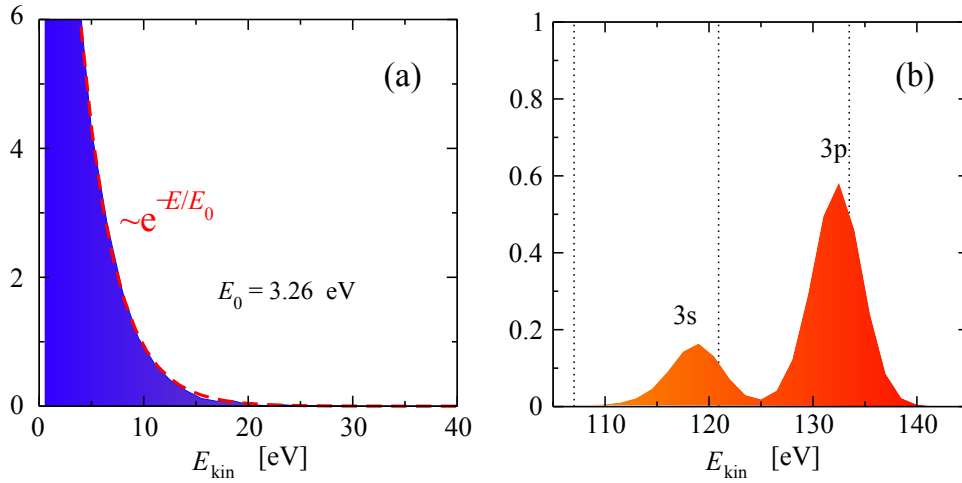

Figure 6.6: Low energy (a) and high energy (b) components of the electron spectrum for $\Delta t = -137$ fs, when the XUV pulse comes before the VUV one. The XUV pulse probes the $3s$ and $3p$ orbitals of the ground state neutral argon in this case, whose ionization potentials differ by ≈ 15 eV.
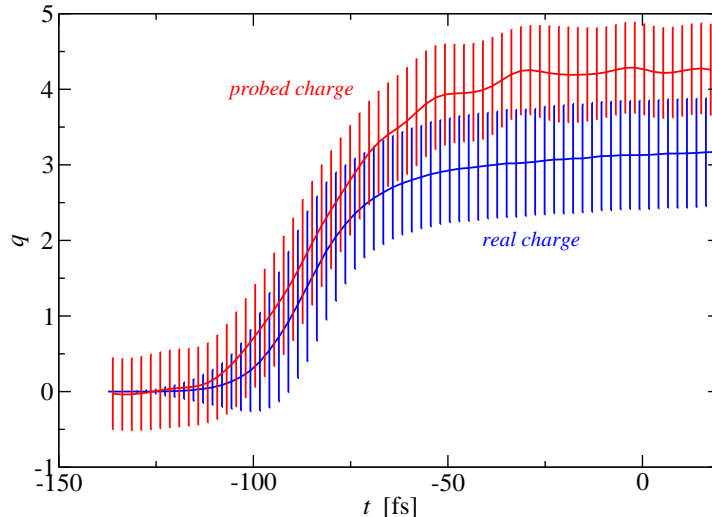
Figure 6.7: Average effective ionic charge as extracted directly from the MD simulation (blue line) compared to the probed charge (red line).

The center of gravity of the XUV part of the energy spectrum can be subtracted from the photo energy $\hbar\omega_{\mathrm{XUV}}$ to calculate the average ionization potential. Interpolating over the ionization potentials of the ionization series of Ar, an average ionic charge can be estimated. It is necessary, however, to account for the inherent $3s - 3p$ splitting of the valence shell. We do this by taking an average E_{ip} as the reference $E_{\mathrm{ip}}(\mathrm{Ar}^{q+})$, where the ionization potential of the $3s$ and $3p$ orbitals have been weighted by their respective occupation number. The probed average charge is compared in Fig. 6.7 to the real one as extracted directly from the MD simulation. Real charge means here the effective charge of the ion, including localized electrons.

The probed charge closely follows the real one and they agree very well within the error bars. The bandwidth of the laser is responsible for less than 10% of the error. There is a systematic deviation towards higher charges due to the positive space charge of the cluster and the excited states of the ions. The former decelerates the electrons by up to 7.5 eV, which translates into probed charges higher by roughly one half. The latter is actually a counting error. The real charge q shown by the blue line considers the full charge of the localized electrons. Excited electrons do not fully screen the nuclear charge. Lower lying electrons screen more, yielding an instantaneous $E_{\mathrm{ip}}(\mathrm{Ar}^{+q*})$ closer to $E_{\mathrm{ip}}(Ar^{+q})$, higher excited ones screen less, such that $E_{\mathrm{ip}}(\mathrm{Ar}^{+q*})$ approaches $E_{\mathrm{ip}}(Ar^{+q+1})$. Hence $E_{\mathrm{ip}}(\mathrm{Ar}^{+q*}) > E_{\mathrm{ip}}(\mathrm{Ar}^{+q})$, such that asserting the average charge from the effective ionization potential will always overestimate. Excited electrons are not counted by their full charge.

The current example conveys a general idea for a yet not suggested use of attosecond pulses: initiate a relatively slow excitation process in an extended system through a femtosecond laser pulse and probe the non-stationary, most likely dissipative relaxation dynamics by time-delayed attosecond pulses.

The experimental implementation at the free electron laser in Hamburg is very difficult, but not impossible, mainly due to the difficulties imposed by the synchro-

nization of two independent light sources with femtosecond, if not sub-femtosecond precision. There are indeed proposals for attosecond FEL pulses (Feldhaus et al. 2005; Saldin et al. 2004a,b; Zholents and Fawley 2004), but it could take long until one is implemented. The experiment could also be performed when both pulses are generated from high harmonics. Most of the technology is already available (Krausz 2007) and the topic will be explored in the next chapter.

Chapter 7

Tracing non-equilibrium plasma dynamics on the attosecond timescale

The combination of a VUV laser pulse from an FEL with an attosecond XUV probe, though promising, is still experimentally out of reach. It is very difficult to synchronize two different light sources with sub-femtosecond precision, especially with the current FEL implementation where the radiation is generated from shot noise. There are proposals to generate attosecond pulses in the FEL itself, going as far as 300 as (Saldin et al. 2004a,b; Zholents and Fawley 2004) or even 200 as (Feldhaus et al. 2005), but they won't be available in a near future also.

Instead of generating just the XUV probe from high-harmonics, one could use the same process to generate the VUV pump too, where the two pulses would be filtered from different regions of the HH spectrum generated by a single NIR pulse. The technology will be available in a near future (Krausz 2007) and it will unite the advantage of the affordable table-top experiment with the intrinsic excellent control of the delay[1]. The drawback would be much shorter pump pulses, almost 100 times shorter as with FEL radiation, and generally little energy in the pulse, due to the low conversion efficiency of the HH process.

The first part of the chapter will analyze the dynamics of Ar_{13} and Ar_{55} clusters excited by few femtosecond VUV laser pulses, focusing on the time-resolved mapping of the charging with an attosecond XUV probe pulse. In contrast to the earlier, adiabatic pump with long FEL pulses, we observe interesting competition between very fast ionization and relaxation of the nano-plasma. The second part investigates this phenomenon by analyzing the relaxation of the electron plasma after instantaneous full ionization of the cluster. The plasma shows in this case strongly-coupled behavior, accompanied by oscillations between kinetic and potential energy with plasma frequency, similar to observations from ultra-cold neutral plasma (Kulin et al. 2000; Pohl et al. 2005) or extended strongly one-component plasma (Zwicknagel 1999). The

---

[1]Timing better than ±200as has been reported so far (Drescher et al. 2002; Kienberger et al. 2002) for the delay of an attosecond XUV pulse with respect to its NIR generator.

initial crossover between ionization and relaxation is reminiscent of this behavior. The last section will show that attosecond pulses can indeed be used to induce and probe strongly-coupled plasma far from equilibrium. Oscillations of the potential energy will be traced in form of oscillations of the probed ionic charge.

7.1 Dynamics of Ar clusters exposed to few femtosecond VUV pulses

The parameters of the pump and probe pulse where chosen according to their experimental availability (Krausz 2007). In the VUV range, $1-5$ fs pulses with $\hbar\omega = 20$ eV and $I = 7 \times 10^{13}$ W/cm^2 were used. The probe was performed with 500 as, $\hbar\omega_{\mathrm{xuv}} = 150$ eV and $I = 1.4 \times 10^{15}$ W/cm^2 pulses. The intensity of the probe is to a large extent irrelevant. Low intensity can be compensated by the repetition rate. There is an upper limit, however, where no more than one probe electron per cluster should be generated, in order not to perturb the subsequent dynamics. For the chosen intensity, the probability to create a single XUV electron in the whole Ar$_{13}$ cluster is $W(1) \approx 0.18$ and for two or more $W(n_{\mathrm{XUV}} \geq 2) \approx 0.02$.
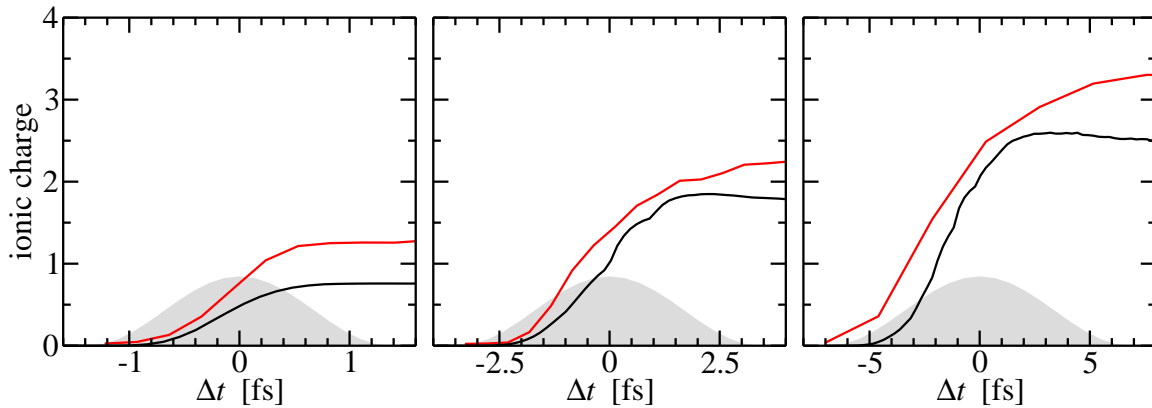

Figure 7.1: Charging of Ar$_{13}$ clusters exposed to very short, that is 1, 2.5 and respectively 5 fs VUV pulses with $\hbar\omega = 20$ eV and $I = 7 \times 10^{13}$ W/cm^2. Black: average effective charge, as extracted directly from the MD simulation. Red: the result of the attosecond probe.

Figures 7.1 and 7.2 show the charging of Ar$_{13}$ and respectively Ar$_{55}$ for various energies of the pump pulse. With Ar$_{13}$ the intensity was kept constant and the pulse duration was reduced, for Ar$_{55}$ the vice versa. The large photo-ionization cross-section has allowed so far full ionization of the cluster within just a few femtoseconds, long before the pulse had reached its maximum. This changes with less pulse energy. The average effective charge, as extracted directly from the MD calculation, is shown in these figures with black lines. Only ³/₄ of all atoms are ionized by the weakest pulse with Ar$_{13}$, with Ar$_{55}$ only ½. The pulses did not carry the same amount of energy. All pulses are too short for electron localization. It sets in rather late and some is

visible for the stronger, or longer, pulses at the slight decay of the effective charge after maximum ionization has been reached. Quasi-free electrons start to recombine into excited states, reducing the effective charge of the ions. For earlier times, the effective charge is equal to the real charge, that is the ions are in their ground state.

The red lines show the results of the XUV probe. For incomplete cluster ionization the probed and the real charge diverge linearly from the beginning. Otherwise the overall behavior is similar to the longer pump. The probed charge follows the real charge until photo-ionization has reached its maximum. The deviation is again somewhere between one half and one full charge. From this point on, the curves diverge. Electron loss via evaporation gains momentum and the charge of the cluster increases, leading to overestimation of the probed charge. At the same time, cluster expansion and electron evaporation cool down the nano-plasma, which enhances electron localization and reduces the effective charge.
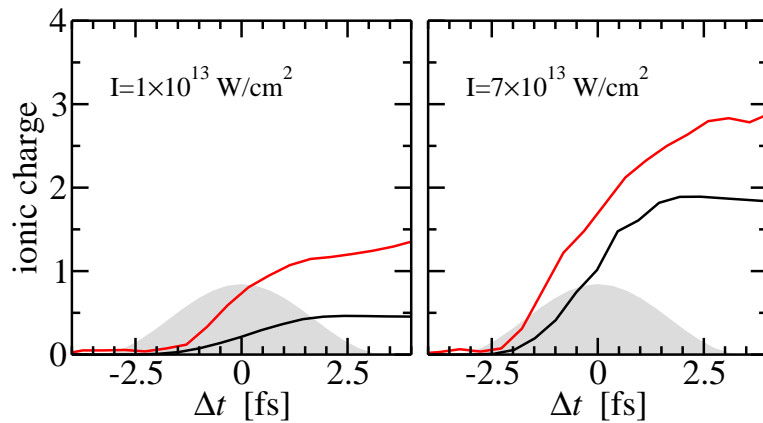

Figure 7.2: Charging of Ar_{55} exposed to 2.5 fs, $\hbar\omega = 20$ electronvolt VUV pulses with $I = 1 \times 10^{13}$ W/cm^2 and respectively $I = 7 \times 10^{13}$ W/cm^2.

With Ar_{55}, the intensity of the probe was lowered to $I_{xuv} = 7 \times 10^{13}$ W/cm^2, to keep the number of XUV electrons below one per cluster. With four times more electrons in the cluster than in the previous cases, the cluster dynamics is no longer so sensitive against the probe. We have lowered the intensity for accuracy reasons, since four XUV electrons per cluster, as obtained with $I_{xuv} = 1.4 \times 10^{15}$ W/cm^2, resulted into a tail at the low energy side of the peaks in Fig. 6.5. The charge of the cluster increases with each probe electron, slowing the subsequent ones down.

Fig. 7.3 depicts the energy balance of the measurement at the example of Ar_{13} irradiated by the 2.5 fs pulse. The spatial charge density at $t = 1$ fs has been averaged over 1000 ensembles and the potential along one axis of the cluster is shown in red. The black dashed lines show the potentials of individual atoms. The difference between the full cluster potential and the potential of an individual atom yields $E_{ip}^{cluster}$, the cluster ionization potential. An outgoing XUV electron hits the detector with $E_{kin} = \hbar\omega - E_{ip}(Z) - E_{ip}^{cluster}$. The energy balance for photon absorption can be depicted easily due to the choice rule (4.38) of the parameter a of the model potential (4.42), which in this case translates to $E_{ip}(Z) = (Z+1)/a$. The origin of the absorp-
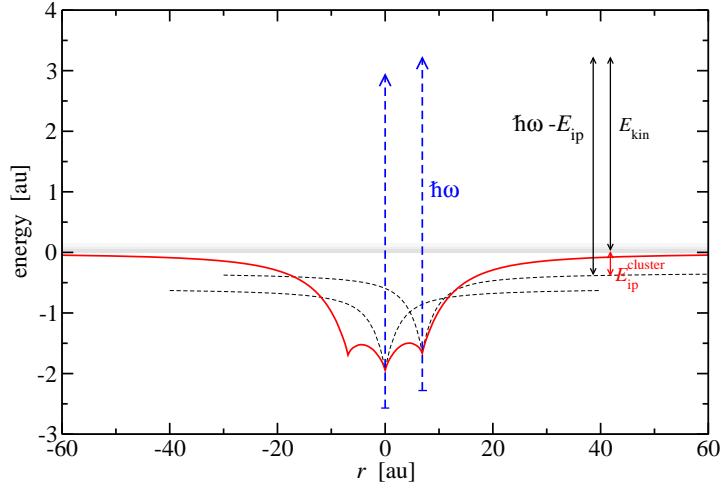
Figure 7.3: Potential landscape in Ar_{13} irradiated by a T=2.5 fs pulse, at $t = 1$ fs after maximum. The potential (red line) was obtained by interpolating along the line connecting the atoms at $(-1/3, -6, -10/3)$ and $(1/3, 6, 10/3)$. The dashed lines show the potential of the individual atoms, where the charge $\bar{Z}$ of an atom has been averaged over all 1000 ensembles. The XUV photo-electrons arrive at the detector with $E_{kin} = \hbar\omega - E_{ip} - E_{ip}^{cluster}$. The absorption arrows have been shifted by $-1/a$ according to Eq. (4.38), which yields $(Z + 1)/a = E_{ip}(Z)$.

tion arrows should thus be placed $1/a$ below the minima of the potential landscape. Absorption of a photon places the electron at the final energy

$$E_f = \hbar\omega + V(\alpha) - 1/a\,, \qquad (7.1)$$

where $V(\alpha)$ is the potential created by all particles in the system at atom α, including by the atom itself.

Figure 7.4 shows an overview of $E_{ip}^{cluster}$ for the two clusters, Ar_{13} and Ar_{55}. The former in the upper row, the latter in the lower. Two time instants are displayed, at the end of the pulse, when $t = T$ and a few femtoseconds later, at $t = 5$ fs. Though more energetic pulses induce higher charging, we see an interesting reversal with Ar_{13} where

$$E_{ip}^{cluster}(T = 5 \text{ fs}) < E_{ip}^{cluster}(T = 2.5 \text{ fs}) < E_{ip}^{cluster}(T = 1 \text{ fs}) \qquad (7.2)$$

for both time instants. Electron evaporation increases $E_{ip}^{cluster}$ during this first stage of the relaxation. The ions are frozen on this time scale.

Shorter pulses induce less ionization events, but the plasma they create inside the cluster is not well localized. Weak ionization creates a shallow cluster potential, such that absorption of a VUV photon with $\hbar\omega = 20$ eV $= 0.735$ au places the photo-electron very close to the cluster threshold, allowing it to travel long excursions outside the cluster volume. With less plasma electrons in the cluster volume to screen the charge of the ions, the XUV photo-electrons experience a higher barrier on their way out. Stronger ionization, in this case longer pulses, creates a deeper cluster potential which keeps more electrons within the cluster volume.
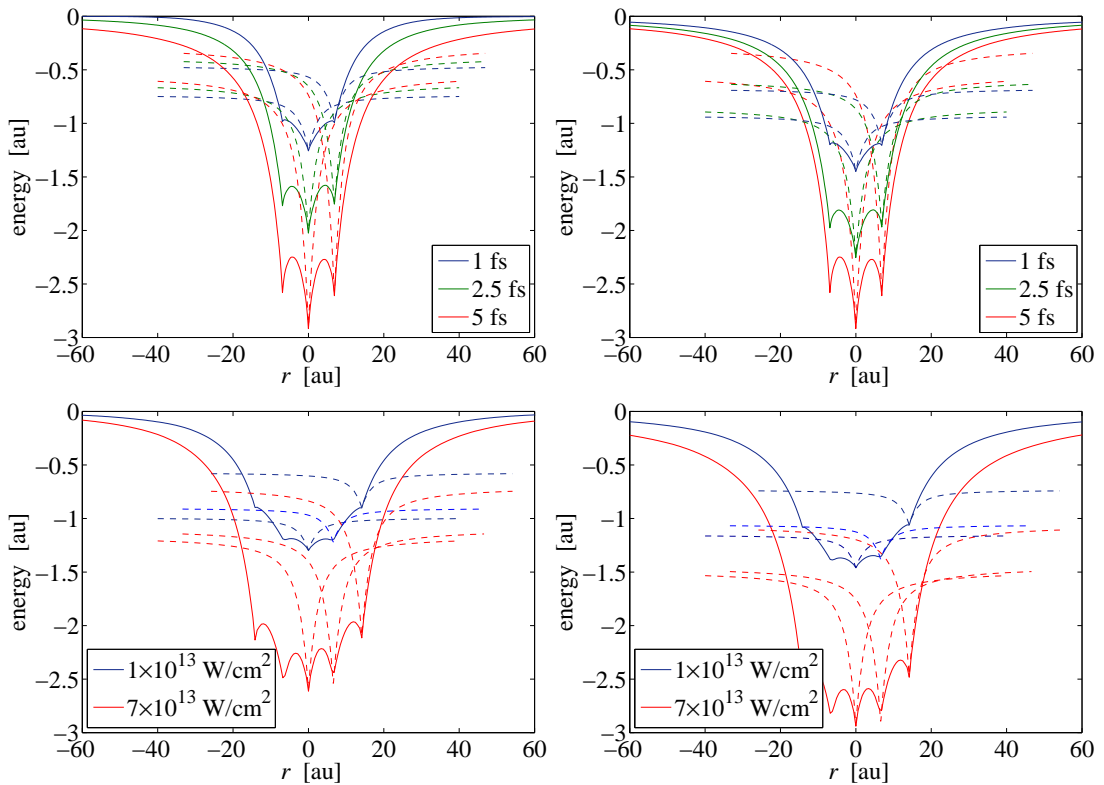
Figure 7.4: Potential landscapes for the excitation scenarios depicted in Fig. 7.1 and 7.2 at two time instants: at pulse end (left column) and at $t = 5$ fs (right column). Top row: Ar_{13}; bottom row: Ar_{55}.

The situation changes already with Ar_{55}, where the larger number of atoms creates a deeper potential for the same ionization degree. The electrons are trapped inside the cluster even for the weakest pulse, such that the cluster barrier is determined directly by the overall charge. The higher the charging, the higher $E_{ip}^{cluster}$.

Figure 7.5 compares the overall charging for both clusters and all pulses studied so far. The charging is given by the number of outer ionized electrons, that is electrons with positive total energy $E > 0$, normalized to the cluster size, such that Ar_{13} and Ar_{55} bare comparison. Two stages are distinct: initial ionization, followed by electron evaporation. The competition between ionization and evaporation leads to either a plateau or, if the initial ionization is very fast, to a local maximum followed by a minimum. Rapid initial ionization happens if the field strength increases sharply, as with the $T = 1$ fs pulse, or if a large number of atoms can be ionized, as with Ar_{55}. This transient overshooting of the ionization degree of the cluster can be understood best if the limit of instantaneous ionization of the electrons is considered.
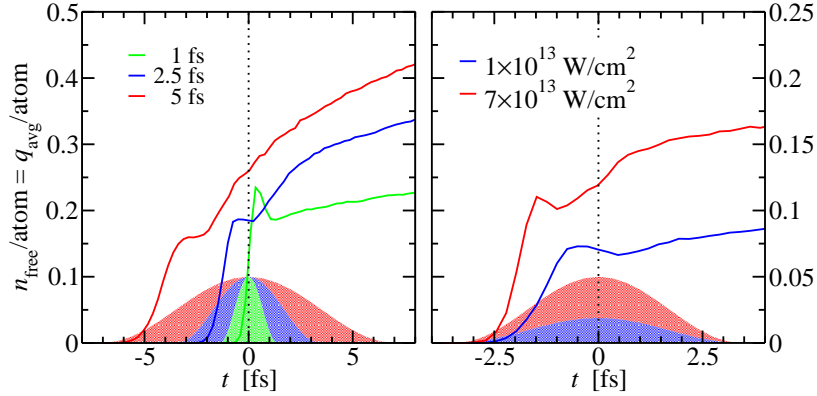
Figure 7.5: Charging of the cluster, that is the number of electrons with positive total energy, normalized to the size of the cluster. Left: Ar_{13}, for the situation described in Fig. 7.1; Right: Ar_{55}, corresponding to Fig. 7.2.

7.2 Instantaneous cluster ionization: formation and relaxation of a nano-plasma

Let us assume all atoms absorb simultaneously one photon each. At $t = 0$ we create one electron at the nucleus of each atom. The electrons are launched in random directions with identical velocities, corresponding to the asymptotic kinetic energy $\hbar\omega - E_{ip} = 4.24$ eV, given by the photon energy $\hbar\omega = 20$ eV and the ionization potential of neutral Ar, 15.76 eV.

The charge of the cluster, that is, the number of electrons with positive total energy is initially 55. But only a fraction of the electrons can actually leave the cluster. Full ionization to Ar_{55}^{55+} requires 3 keV, whereas the total excess energy of the electrons adds up to only 233 eV. The charge of the cluster, normalized to the cluster size is shown in Fig. 7.6(a). The total available energy is quickly redistributed among the electrons, since the average charge drops within 200 as from 1.0 to 0.3. The previously observed overshooting of the cluster charge (Fig. 7.5) can now be traced back to instantaneous, or almost instantaneous ionization of the cluster atoms, where the electrons are *created* at a faster rate than they can exchange energy. The final charge of 0.2 per atom is close to the ones observed earlier with realistic calculations (Fig. 7.5).

The initial state is at the same time one of minimum total potential energy and maximum kinetic energy. The relaxation of the energy distribution is shown in Fig. 7.6(b) with the average potential and kinetic energy of the trapped, inner-ionized electrons. After the initial redistribution of the electrons within the cluster volume, marked by the sharp increase of the potential energy, the plasma relaxation continues into a series of energy oscillations, with a continuous exchange of kinetic and potential energy. The period of the energy oscillations $\tau_{osc} \approx 0.79$ fs is in good agreement with the plasma period $\tau_{pl} = 2\pi/\omega_{pl} = \sqrt{\pi m/\rho} = 0.77$ fs, corresponding to an effective cluster radius of 8.5 Å. The total energy is conserved, violated only
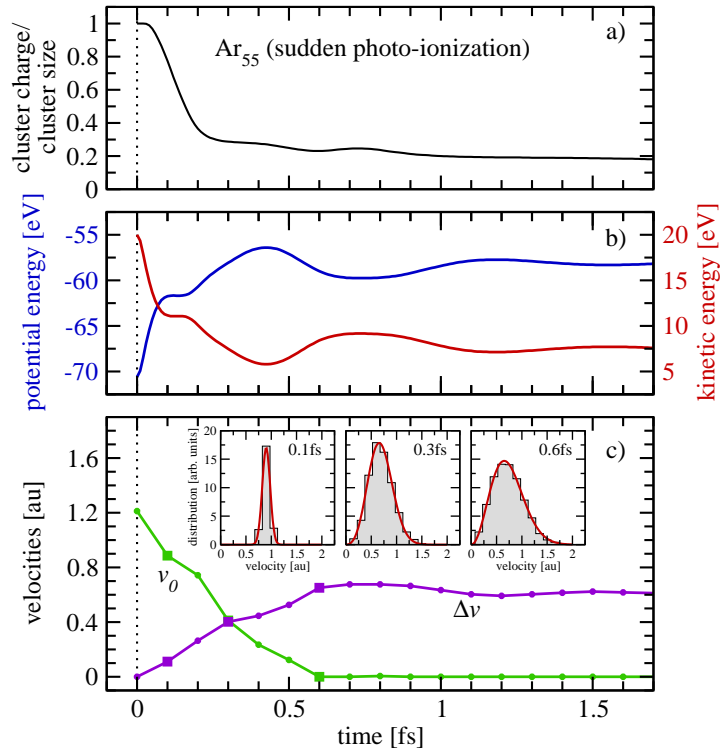
Figure 7.6: Relaxation of Ar_{55} after sudden ionization of all atoms. (a) charging or outer ionized electrons per atom; (b) total kinetic and potential energy of the electrons, per electron; (c) Fit parameters for the shifted thermal-like velocity distribution (7.3). Insets: fits of the velocity distributions at several instants during the relaxation.

slightly through electrons which leave the cluster. This violation is however negligible, because the number of these electrons is small on this time scale. Moreover, they are slow and carry little energy.

To check for the existence of a plasma, we have fitted the velocity distributions of the electrons with the function (MacDonald et al. 1957):

$$f_{v_0, \Delta v}(v) = C \cdot v^2 \cdot \exp\left(-\frac{(v - v_0)^2}{\Delta v^2}\right), \tag{7.3}$$

where C is just a normalization constant. $f_{v_0, \Delta v}(v)$ contains both limits: the initial mono-energetic distribution with $v_0 = \sqrt{2E_0/m}$ and $\Delta v = 0$, as well as the thermalized electron plasma, characterized by a Maxwell-Boltzmann distribution with $v_0 = 0$ and $\Delta v = \sqrt{2kT/m}$. The ratio $v_0/\Delta v$ can therefore be used to quantify the relaxation of the cluster as a function of time. It is infinite for a mono-energetic electrons and zero for an equilibrated, Maxwell-Boltzmann velocity distribution.

Fig. 7.6(c) shows the fit parameters v_0 and Δv at several time instants during the evolution of the electron plasma. At $t = 0$ one has $v_0 = \sqrt{2E_0/m}$ and $\Delta v = 0$. Surprisingly, the electron velocity distribution equilibrates within just 0.6 fs, when

$v_0 = 0$ and Δv stabilizes. It continues though to perform slight oscillations in phase with the oscillations of E_{kin} in Fig. 7.6(b).

In weakly coupled plasma, correlations build up faster than the relaxation of the single particle distribution function. Assuming that the latter is also faster than the global relaxation of the system, such as expansion, the Bogoliubov hierarchy of characteristic times is obtained. This hierarchy breaks down in strongly coupled plasmas, that is when the Coulomb coupling parameter $\Gamma > 1$. The time scales for spatial correlation and equilibration approach each other, leading to oscillations of the temperature around the average as equilibrium is reached (Pohl et al. 2005; Zwicknagel 1999). It is the situation encountered here, where the relaxation time $\tau = 0.6$ fs of the single particle distribution function is of the same order as the period $\tau_{\text{pl}} = 0.77$ fs for plasma oscillations, which sets the time scale for correlation build-up. The period $\tau_{\text{osc}} = 0.79$ fs of the energy oscillations is almost equal to τ_{pl}, indicating volume plasmon oscillations. The oscillations damp quickly after just two plasma periods, which is typical for an inhomogeneous plasma (Pohl et al. 2005). For comparison, a rough estimation of the plasma equilibration time using Spitzer's self-collision time t_c (4.15) yields only $t_c = 287$ as.

Whereas plasma oscillations have been observed so far with extended OCP's (Zwicknagel 1999) or ultra-cold plasma with million of particles (Kulin et al. 2000; Pohl et al. 2005), we observe strongly coupled regime with only 55 electrons having an average temperature of $25,000$ K.

7.3 Creating and monitoring non-equilibrium nano-plasma in clusters with attosecond laser pulses

The first requirement for the observation of energy oscillations in a nano-plasma is very high temporal resolution, able to resolve the sub-femtosecond oscillation period. As mentioned earlier, light pulses generated from high harmonics of a single NIR pulse already offer this potential. At the moment, each pulse can be timed within ± 200 as with respect to the generating NIR field (Drescher et al. 2002; Kienberger et al. 2002). This section will therefore address the question whether plasma oscillations can be initiated and probed with attosecond laser pulses. The first requirement, temporal resolution, is already fulfilled.

If the same scheme for probing the ionic charge with attosecond XUV laser pulses is employed, than the energy oscillations of the quasi-free electrons will affect the initial potential energy, in other words, $E_{\text{ip}}^{\text{cluster}}$ of the XUV photo-electrons and will be reflected in oscillations of the probed charge. Maximum potential energy corresponds to maximum delocalization of the electron cloud which, as shown in figure 7.4, imposes a higher barrier on the outgoing XUV photo-electrons, hence higher probed charge. By the same reasoning, minimum potential energy corresponds to maximum localization and minimum error of the probed charge.

We have chosen $T = 250$ as for both the pump and the probe pulse, to ensure that the initial excitation and the probe are fast on the time-scale of the system

$\tau_{\text{pl}} = 770$ as. Experimentally this is already possible: pulses as short as 170 as have been achieved so far (Lopez-Martens et al. 2005; Schultze et al. 2007). The intensity $I = 5 \times 10^{14}$ W/cm^2 of the pump was chosen such, that approximatively one electron per atom is ionized. Though this intensity is not available yet, it is under active development (Krausz 2007). The intensity of the probe $I_{\text{xuv}} = 2.45 \times 10^{14}$ W/cm^2 ensures that multiple probes, that is, several XUV photo-electrons produced during the laser pulse, will not distort the final result considerably. The probability $W(2) = 2.11 \times 10^{-3}$ to produce two XUV photo-electrons in the whole cluster during the probe pulse is approximatively 30 times less than the probability $W(1) = 6.56 \times 10^{-2}$ for just one. As before, a too low probe intensity can be compensated by a higher repetition rate.

The very short pulse raises two more issues. One of them, the spectral bandwidth, has already been encountered in the previous chapter. It becomes even more important now, since the pump is just as short as the probe and can no longer be assumed monochromatic. The bandwidth of a 250 as Gaussian pulse is $\Delta\omega = 4\log(2)/T = 7.36$ eV, roughly on third of the photon energy of the pump. Near threshold, the photo-ionization cross-section cannot be considered constant. It decays almost as $\omega^{-3.5}$, such that the VUV photo-electrons will not only be launched with different initial velocities, but more electrons will be ionized at the red part of the pulse than at the blue one.

The other issue arises from the finite number of oscillations performed by the electric field of a $T = 250$ as pulse of $\hbar\omega = 20$ eV photon energy, namely two. Fermi's Golden Rule (Friedrich 2006, §2.4) assumes infinitely long interaction times, or at least long on the scale of the field oscillations.

Both issues can be dealt with if a Gaussian pulse $\mathbf{E}(t) = \hat{\epsilon}_0 \mathcal{E} e^{-t^2/2\sigma^2} \cos\omega_0 t$ is assumed from the beginning when Fermi's Golden Rule is derived. The transition probability does not diverge anymore and the limit $t \to \infty$ for an average transition rate is no longer needed.

In first order perturbation theory (Eq. (2.11)), the excitation probability into the final state state $|f\rangle$, such as $E_f - E_i = \hbar\omega$ is

$$w_{i \to f}(t) = \frac{1}{\hbar^2} \left| \int_{-\infty}^{t} \langle f|V(t')|i\rangle e^{i\omega t'} \right|^2 , \tag{7.4}$$

which for a Gaussian pulse leads to

$$
\begin{aligned}
w_{i \to f}(t) &= \frac{1}{\hbar^2} \left| \langle f|\hat{\epsilon}_0 \mathcal{E} \cdot \mathbf{r}|i\rangle \int_{-\infty}^{t} \exp\left(-\frac{t'^2}{2\sigma^2} + i\omega t'\right) \frac{e^{i\omega_0 t'} + e^{-i\omega_0 t'}}{2} dt' \right|^2 \\
&= \frac{\pi\sigma^2 \mathcal{E}^2}{8\hbar^2} |\langle f|\hat{\epsilon}_0 \cdot \mathbf{r}|i\rangle|^2 \times \\
&\quad \left[\exp\left(-\frac{1}{2}(\omega - \omega_0)^2 \sigma^2\right) \left(1 + \text{erf}\left(\frac{t}{\sqrt{2}\sigma} - i\frac{(\omega - \omega_0)\sigma}{\sqrt{2}}\right)\right) + \right. \\
&\quad \left. + \exp\left(-\frac{1}{2}(\omega + \omega_0)^2 \sigma^2\right) \left(1 + \text{erf}\left(\frac{t}{\sqrt{2}\sigma} - i\frac{(\omega + \omega_0)\sigma}{\sqrt{2}}\right)\right) \right]^2 .
\end{aligned}
\tag{7.5}
$$

The two terms inside the square brackets are alternatively significantly different from zero for either $\omega - \omega_0 \to 0$ or $\omega + \omega_0 \to 0$. We discard the latter, which describes stimulated emission

$$
\begin{aligned}
w_{i \to f}(t) = \frac{\pi \sigma^2 \mathcal{E}^2}{8\hbar^2} |\langle f|\hat{\epsilon}_0 \cdot \mathbf{r}|i\rangle|^2 \times \\
\exp\left((\omega - \omega_0)^2 \sigma^2\right) \left[1 + \mathrm{erf}\left(\frac{t}{\sqrt{2}\sigma} - i\frac{(\omega - \omega_0)\sigma}{\sqrt{2}}\right)\right]^2 .
\end{aligned}
\tag{7.6}
$$

Moreover, $\frac{\sigma}{\sqrt{\pi}} e^{-(\omega \pm \omega_0)^2 \sigma^2 / 2}$ becomes a δ-function for large σ. In this case, the imaginary part of the argument to the error function is suppressed and Fermi's Golden Rule is obtained when $t \to \infty$

$$
w_{i \to f}(t \to \infty) = \frac{\pi^{3/2} \sigma \mathcal{E}^2}{2\hbar^2} |\langle f|\hat{\epsilon}_0 \cdot \mathbf{r}|i\rangle|^2 \delta(\omega - \omega_0) .
\tag{7.7}
$$

Eq. (7.7) differs from the textbook formula (Cohen-Tannoudji et al. 1997, §B$_{\mathrm{IV}}$.1) by a factor of $\sqrt{\pi}$ due to the Gaussian shape of the pulse. Renormalization to a square pulse eliminates it.
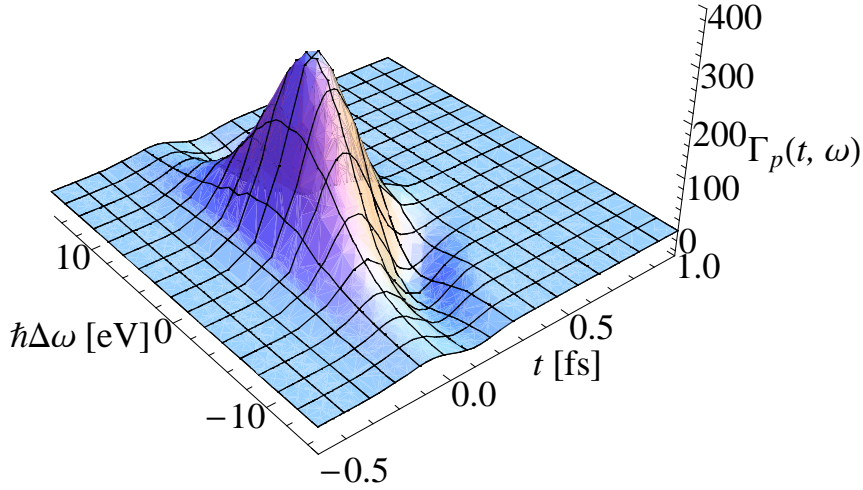

Figure 7.7: Time and frequency dependence of the transition rate as introduced by a Gaussian pulse with $T = 250$ as. The dipol matrix element is not included, that is $\Gamma_p(t) = \frac{\mathrm{d}}{\mathrm{d}t} \frac{w_{i \to f}(t)}{|\langle f|\hat{\epsilon}_0 \cdot \mathbf{r}|i\rangle|^2}$ is shown.

For a fincite pulse and consequently non-zero bandwidth, the ionization probability presents an oscillatory behaviour due to the imaginary part of the argument to the error function in Eq. (7.6). This leads to negative instantaneous ionization rates $\Gamma_{i \to f}(t) = \mathrm{d}w_{i \to f}(t)/\mathrm{d}t$, which though physical, are incompatible with the current Monte Carlo approach. It is not possible to recombine electrons back from the continuum the same way they have been created. This situation is illustrated in Fig. 7.7 at the example of a 250 as pulse. Only the influence of the pulse envelope is

shown, that is the instantaneous ionization rate $\Gamma_{i \to f}(t)$ was divided by the modulus square $|\langle f|\hat{\epsilon}_0 \cdot \mathbf{r}|i\rangle|^2$ of the dipol matrix element. There are two regions of $\Gamma_{i \to f}(t) < 0$, namely for $t > 0$ and off-central frequencies. They account however for very little of the whole ionization yield, for which reason we renormalized the final ionization probability $w_{i \to f}(t \to \infty)$ to the intensity profile to obtain the instantaneous ionization rate

$$
\begin{aligned}
\Gamma_{i \to f}(t, \omega) &= \frac{\pi^{1/2}\sigma\mathcal{E}^2}{2\hbar^2}|\langle f|\hat{\epsilon}_0 \cdot \mathbf{r}|i\rangle|^2 \exp\left[-(\omega - \omega_0)^2\sigma^2 - \frac{t^2}{\sigma^2}\right] \\
&= \frac{\pi^{1/2}\sigma}{2\hbar^2}|\langle f|\hat{\epsilon}_0 \cdot \mathbf{r}|i\rangle|^2 e^{-(\omega-\omega_0)^2\sigma^2} I(t)\,.
\end{aligned}
\tag{7.8}
$$

In our Monte Carlo approach, photo-ionization is evaluated according to the probability distribution $\Gamma_{i \to f}(t, \omega)\mathrm{d}t\mathrm{d}\omega$ of Eq. (7.8) in each time step for 20 equidistant frequencies in the range $-4\sigma_\omega \leq \omega - \omega_0 \leq 4\sigma_\omega$, for both the VUV pump and the XUV probe.
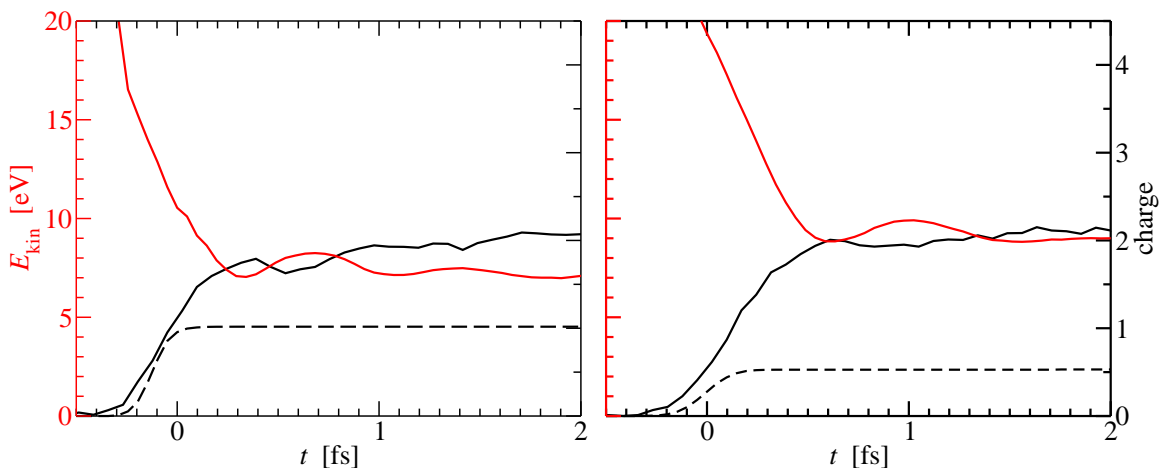

Figure 7.8: Pump-probe experiment with two very short, equally long $T = 250$ as pump and probe pulses. Left: pump with $\hbar\omega = 20$ eV; right: with $\hbar\omega = 30$ eV. The dashed lines show the real average charge as extracted directly from the MD simulation, the continuous black lines the probed one. The average kinetic energy of the electrons is shown in red.

The results are shown in Fig. 7.8 for two pump frequencies, $\hbar\omega = 20$ eV on the left and $\hbar\omega = 30$ eV on the right. The dashed lines show the average charge of the atoms, the continuous black line the probed one. For $\hbar\omega = 30$ eV the photo-ionization cross-section is smaller, such that the cluster is only half ionized. Accordingly, the probed and the real charge diverge linearly from the beginning. The final deviation is also much larger than with 20 eV, since the larger photon energy allows more electrons to leave the cluster, increasing the space charge.

The red lines depict the average kinetic energy of all electrons, decaying from $\hbar\omega$ for the very first electron created, down to approximatively 7 eV for the 20 eV and

respectively 10 eV for the 30 eV pulse. The relaxation turns into small oscillations, which are mirrored in the probed charge as expected. Minima of the potential energy, corresponding to maxima of the kinetic energy, are synchronized with minima of the probed charge and vice versa. Two oscillations with a period of roughly 0.7 fs are performed with the 20 eV pump and only one of ≈ 0.95 fs with the 30 eV pulse. The smaller oscillation period in the first case accounts for the more effective ionization, hence increased plasma density. The larger density also increases the average pairwise Coulomb energy, which together with the lower kinetic energy of the electrons yields a stronger coupled plasma. The damping of the oscillations should be attributed to the finite size of the system, as energy is dissipated into electron evaporation (Pohl et al. 2005). No energy has yet been dissipated in the cluster expansion.

In conclusion, attosecond pulses have been used to create a nano-plasma and monitor its dynamics in systems with radius of only 8.5 Å. Attosecond probing, as introduced in Chapter 6 has been employed not only during the initial excitation, but also afterwards, to monitor relaxation. Strong parallels to ultra-cold neutral microscopic plasma (Killian et al. 1999; Kulin et al. 2000; Pohl et al. 2005) containing thousands to millions of particles could be observed, owing to the strong-coupling. With as little as 55 electrons, or even 22, and an average temperature larger than $25,000$ K, the created nano-plasma show fast equilibration on the time scale of the plasma period, followed by energy oscillations with plasma frequency. Such behavior had been known so far only from extended one-component plasma (Zwicknagel 1999) or ultra-cold neutral plasma (Killian et al. 1999; Kulin et al. 2000; Pohl et al. 2005).

Chapter 8

Summary and Outlook

This thesis has focused on the interaction of intense VUV laser light with rare-gas clusters. This new parameter regime, namely the interaction of matter with strong high frequency laser radiation, has been sparked by the ongoing efforts to achieve microscopy with atomic resolution, time resolved on the scale of atomic motion. Being able to record the diffraction image of a single object with a single laser pulse requires very high photon energy to achieve the needed spatial resolution and very high photon flux, to ensure detectability due to the low cross-section for coherent scattering. Free electron lasers, now under construction at LCLS in Stanford, at DESY in Hamburg and at RIKEN in Japan are the only systems that can deliver laser radiation with the required parameters. However, the dynamics of the target under intense radiation is not yet fully understood. It is currently assumed that it would be destroyed within less than 5 fs (Neutze et al. 2000), but the damage threshold could be much higher.

The first experiments with intense high frequency laser radiation were performed in the VUV regime at 98 nm in 2001 (Wabnitz et al. 2002), during the first testing phase of the FEL at DESY, in Hamburg. They have shown surprising 40 fold enhancement of energy absorption in atomic clusters with respect to isolated atoms. Theoretical investigation performed in several groups have identified inverse bremsstrahlung (IBS) as the dominant absorption mechanism in this regime, but they disagree strongly with respect to the origin of its efficiency.

We have developed a hybrid quantum-classical approach to laser-cluster interaction which pays special attention to screening effects in the cluster nano-plasma. At the cross-over between IR and X-rays, VUV radiation represents a unique combination of medium photon-energy and small ponderomotive amplitude. The photo-electrons are slow. Trapped in the background charge of the ions, they form a dense, warm nano-plasma. Lacking an immediate heating from the laser due to the small ponderomotive amplitude, the plasma screens the cluster ions and modifies their further absorption properties.

It was possible to identify those electrons which localize about the ions and perform the screening. They are in effectively excited states about these ions, a kind of multiple Rydberg excitations, which allowed us to cast the cluster dynamics under a new perspective: effectively highly excited ions which interact with each other in the presence of a fully delocalized electron plasma. We have estimated the binding energy

and the photo-ionization cross-section of valence or core electrons in the presence of electrons on Rydberg orbits. On the other hand, the mean revolution period T_i of the electrons on those orbits defines the time scale on which the excited ions respond to changes in the cluster environment. These electrons and the time intervals T_i they define are the key elements for the description of the entire cluster dynamics. All rate based quantum-mechanical processes are considered in a fixed cluster environment, defined by the time intervals T_i. They provide thus the natural time scale to interpolate between the deterministic classical description of the plasma dynamics and the quantum-mechanical, rate based description of photo-ionization.

The model was illustrated at the example of an Ar_{147} cluster exposed to VUV radiation similar to the one available at FLASH, in Hamburg. The decay of the inverse bremsstrahlung (IBS) with laser frequency was then analyzed. Normalized per inner-ionized electron, the IBS absorption proved to be independent of the particular non-singular approximation of the Coulomb potential over the whole frequency range, thus mitigating the initial suspicion for technically induced resonances. Indirect effects on the *total* IBS absorption are still possible due to slightly different ionization thresholds each approximation yields, leading to a different number of absorbing inner-ionized electrons. It was not possible though to identify one model potential as being superior. Possible implications of a particular choice should be checked on a case to case basis.

Comparison of the IBS absorption rate with the analytical approach by Krainov (2000) emphasized the role of correlation effects and multiple collisions in a high density plasma.

In 2005, the new stage of FLASH lased at 32 nm (Ayvazyan et al. 2006). New, yet unpublished electron time of flight spectra were available (Möller 2007), which the new model reproduced.

The transient dynamics of the clusters during their interaction with the laser field is not accessible in the experiment. The final ionic charges measured at the detector can differ considerably from the ones during the laser excitation due to recombination during the cluster expansion. Moreover, the incoherent nature of the process makes it impossible to reconstruct previous states of the system from the standard experimental observables, such as time of flight or charge spectra.

We have proposed a scheme to probe the transient cluster dynamics with attosecond laser pulses during the interaction with VUV radiation. Operating in the extreme ultraviolet (XUV), the time delayed attosecond pulse creates very fast photo-electrons, which leave the cluster immediately. Their kinetic energy at the detector bares the fingerprint of the binding energy, hence the charge, at the mother atom. This scheme would shed more light on the absorption mechanisms in the VUV range, thus helping to discriminate between the different theoretical interpretations (Bauer 2004; Georgescu et al. 2007a; Jungreuthmayer et al. 2005; Rusek and Orlowski 2005; Santra and Greene 2003; Siedschlag and Rost 2004). At the same time, our specific example conveys the general idea for a so far not suggested use of attosecond pulses: Initiate a relatively slow excitation process in an extended system through a femtosecond laser pulse, and probe the non-stationary, most likely dissipative relaxation dynamics by time-delayed attosecond pulses.

In the last part we have turned our attention to diabatic excitation schemes. They were motivated by technological advance of high harmonics (HH) sources which would allow the implementation of the VUV pump - XUV probe scheme in a table-top experiment. Not only the probe, but also the pump would be generated from high harmonics. Pulse durations almost hundred times shorter then with FEL radiation are characteristic here due to the low conversion efficiency of the HH process. In this limit, an interesting competition between fast ionization and relaxation of the electron plasma was observed. Analysis in the instantaneous-ionization limit and realistic calculations with 250 as showed fast relaxation of the single particle distribution function on the time scale of the plasma period, as well as subsequent energy oscillations with the period of the plasma oscillations. This situation is known as the breakdown of the Bogoliubov time hierarchy in strongly coupled plasma, when the equilibration speeds up and the correlation building slows down, to meet at the period of plasma oscillations. Such behavior was only known so far from extended one component plasma (Zwicknagel 1999) or ultra-cold neutral plasma (Kulin et al. 2000; Pohl et al. 2005). The initial competition appears now as the reminiscence of this behavior. The dynamics was probed by the same method with 250 as XUV pulses not only during the initial excitation, but also during the relaxation to monitor the energy oscillations at oscillations of the probed charge.

The hybrid quantum-classical interaction model, the attosecond pump-probe scheme and the diabatic excitation scheme have been published as Georgescu et al. (2007a), Georgescu et al. (2007b) and Saalmann et al. (2008), respectively.

The time-resolved study of ultrafast dynamical processes in finite systems requires for new probing techniques. In the future we would like to eliminate the systematic error introduced by the space charge with the current probing scheme. The attosecond probe pulse could be replaced by a few cycle IR pulse, in a method similar to attosecond streaking. Instead of recording the time and momentum distribution of an electron wave packet emerging from a single atom, one could measure the time and momentum distribution of a whole electron cloud being ionized from a highly excited cluster. Alternatively, tuning the probe to a non-linear resonance in the self consistent potential outside the cluster would provide very fast electron beams at regular time intervals as observed by Fennel et al. (2007) in SPARC. The *comb* of electron beams could be used to induce fast decaying core hole excitations in the ions and allow therefore a time resolved study of the charging via the emitted X-ray photons, which are no longer subject to interaction with the space charge.

Appendix A

Average photo-ionization cross-section for a many-electron isolated atom

Given the electronic configuration of an atom with q orbitals

$$l_1^{w_1} \ldots l_i^{w_i} \ldots l_q^{w_q} , \tag{A.1}$$

where l_j denotes the orbital and w_j its occupation number, we are interested in the average cross-section for a single electron transition from l_i to l_f under absorption of one photon

$$l_1^{w_1} \ldots l_i^{w_i} \ldots l_f^{w_f-1} \ldots l_q^{w_q} + \hbar\omega \rightarrow l_1^{w_1} \ldots l_i^{w_i-1} \ldots l_f^{w_f} \ldots l_q^{w_q} . \tag{A.2}$$

l_f can also denote a state in continuum, corresponding to ionization. There are several allowed states, or energy levels, for each of the initial and final configurations, denoted by γJ and $\gamma' J'$, respectively. J is the total angular momentum of the electron cloud and γ stands for the rest of the good quantum numbers. No particular coupling conditions have been assumed yet and magnetic fields are absent. The transition cross-section is spread over a whole array $\gamma J - \gamma' J'$ of transitions allowed between the initial and final configurations.

The photo-ionization cross-section for a single line, that is for a single $\gamma J M - \gamma' J' M'$ transition reads (Friedrich 2006)

$$\sigma = 4\pi^2 \alpha \hbar\omega |\langle \gamma' J' M' | \hat{\mathcal{D}} | \gamma J M \rangle|^2. \tag{A.3}$$

with the dipole operator

$$\hat{\mathcal{D}} = e \sum_i \mathbf{r}_i , \tag{A.4}$$

where e is the electron charge and the sum runs over all electron coordinates.

The average cross-section is obtained by summing over the final and averaging

over the initial states

$$\sigma_{\text{avg}} = 4\pi^2 \alpha \hbar \omega \frac{\sum_{\gamma JM, \gamma' J'M'} |\hat{\mathcal{D}}_{\gamma JM, \gamma' J'M'}|^2}{\sum_{\gamma J} 2J+1}$$
$$= 4\pi^2 \alpha \hbar \omega \frac{\text{Sp}\left[(\hat{\mathcal{D}}_{\gamma M, \gamma' M'})(\hat{\mathcal{D}}^*_{\gamma M, \gamma' M'})^{\text{T}}\right]}{\sum_{\gamma J} 2J+1}. \tag{A.5}$$

The trace operator is invariant with respect to any orthogonal transform and the multiplicity of a given configuration, in its turn a trace over the identity operator of the subspace spanned by $|\gamma JM\rangle$, also. Hence, σ_{avg} is independent of the chosen coupling representation of the total wave function, such jj, LS or alike. In the following LS or Russel-Saunders coupling scheme will be used.

In the LS scheme, all w_j electrons in l_j are coupled together to a total orbital angular momentum L_j and total spin S_j, which are then coupled onto the total momenta of the underlying sub-shells

$$[[[\ldots[(L_1 S_1)\mathfrak{L}_1\mathfrak{S}_1, L_2 S_2]\mathfrak{L}_2\mathfrak{S}_2, \ldots]\mathfrak{L}_{q-1}\mathfrak{S}_{q-1}, L_q S_q]\mathfrak{L}_q\mathfrak{S}_q]\mathfrak{J}\mathfrak{M} \tag{A.6}$$

to obtain total intermediate momenta $\mathfrak{L}_j$ and $\mathfrak{S}_j$. After the last orbital q, the total orbital angular momentum $L = \mathfrak{L}_q$ and the total spin $S = \mathfrak{S}_q$ are obtained. $J = \mathfrak{J}$ is the total angular momentum and $M = \mathfrak{M}$ its magnetic quantum number.

The obtained wave function still lacks antisymmetry, which is added in two steps. The first one is performed within each sub-shell in a recurrent manner for each electron, in parallel with coupling of angular momenta. The method, known as coefficients of fractional parentage – *cfp*, is described in detail in Cowan (1981, §9-5). The resulting states $|l_j^{w_j} L_j S_j, M_{L_j} M_{S_j}\rangle$ are fully antisymmetric and coupled. The product states

$$|l_1^{w_1} L_1 S_1 M_{L_1} M_{S_1}\rangle \ldots |l_i^{w_i} L_i S_i M_{L_i} M_{S_i}\rangle \ldots |l_q^{w_q} L_q S_q M_{L_q} M_{S_q}\rangle \tag{A.7}$$

are then coupled to ψ_b according to Eq. (A.6). ψ_b is only antisymmetric with respect to permutation of coordinates within the same sub-shell. Full antisymmetry is achieved by performing a Slater-like step

$$|\gamma JM\rangle \equiv \Psi_b = \left[\frac{\prod_j w_j!}{N!}\right]^{1/2} \sum_P (-1)^P \psi_b^{(P)}, \tag{A.8}$$

where the sum runs only over permutations of coordinates among different sub-shells.

Before σ_{avg} is evaluated, it should be noted that it does not depend on the field polarization. If the Wigner-Eckart theorem (Brink and Satchler 1993, 4.7), (Cowan 1981, 11-4) is applied

$$\langle \gamma JM|\hat{\mathcal{D}}_q^{(1)}|\gamma' J'M'\rangle = (-1)^{j-m} \begin{pmatrix} J & 1 & J' \\ -M & q & M' \end{pmatrix} \langle \gamma J\|\hat{\mathcal{D}}^{(1)}\|\gamma' J'\rangle \tag{A.9}$$

and inserted in (A.5), the sum over the magnetic quantum numbers MM' is equivalent to a spherical average

$$\sum_{MM'} \sigma = \frac{4\pi^2 \alpha \hbar \omega}{[1]} \sum_{MM'} [1] \begin{pmatrix} J & 1 & J' \\ -M & q & M' \end{pmatrix}^2 |\langle \gamma J || \hat{\mathcal{D}}^{(1)} || \gamma' J' \rangle|^2$$

$$= \frac{4\pi^2 \alpha \hbar \omega}{3} \mathsf{S}_{\gamma J, \gamma' J'} , \qquad (A.10)$$

which eliminates the laser polarization q. The orthogonality relation of the 3j symbols (Brink and Satchler 1993, AI),(Cowan 1981, 5.1) was used and $\hat{\mathcal{D}}_q^{(1)}$ is the representation of $\hat{\mathcal{D}}$ in the $\mathcal{D}_1$ rotation group, corresponding to linear polarization for $q = 0$ and circular polarization for $q = \pm 1$. $[j]$ is the shorthand for $2j + 1$ and

$$\mathsf{S}_{\gamma J, \gamma' J'} = |\langle \gamma J || \hat{\mathcal{D}}^{(1)} || \gamma' J' \rangle|^2 \qquad (A.11)$$

is the line strength (Shortley 1935).

Because electron coordinates are fully equivalent in Ψ_b and $\hat{\mathcal{D}}$ is just a sum over single particle operators, it should be in principle possible to reduce the line strength $\mathsf{S}_{\gamma J, \gamma' J'}$ to a single particle reduced matrix element

$$\mathsf{S}_{\gamma J, \gamma' J'} = |\langle \Psi_b || \hat{\mathcal{D}}^{(1)} || \Psi_b' \rangle|^2 = |D_1|^2 \cdots |D_5|^2 |\langle l_i || \mathbf{r}_N || l_f \rangle|^2 . \qquad (A.12)$$

The stepwise reduction leads to five coefficients. A strict derivation requires seven (Cowan 1981), but two of them can be eliminated if it is assumed that the coupling scheme has been changed such, that the initial and the final orbitals, the only orbitals affected by the transition, are moved at the end of the LS coupling chain (A.6) for both configurations. The total orbital angular momentum $\mathfrak{L}_q$, the total spin $\mathfrak{S}_q$ or angular momentum $\mathfrak{J}_q$ remain unchanged. On the other hand, both configurations have identical quantum numbers $L_j, S_j, \mathfrak{L}_j, \mathfrak{S}_j$ for all other sub-shells $j = 1 \ldots q - 2$, which simplify to δ factors when the reduced matrix element (A.11) is evaluated. With this sub-shell, or orbital permutation, the initial, or source orbital is forelast $i = q - 1$ and the final one, or the destination is at the end of the coupling chain $f = q$.

If Eq. (A.4) and (A.8) are considered, $\langle \Psi_b | \hat{\mathcal{D}} | \Psi_{b'} \rangle$ is quickly reduced to the matrix element of the single particle dipole operator with the coupled and partially anti-symmetrized states ψ_b

$$\langle \Psi_b | \hat{\mathcal{D}} | \Psi_{b'} \rangle = D_1 \langle \psi_b^{P_N} | \mathbf{r}_N | \psi_{b'}^{P_N'} \rangle \qquad (A.13)$$

where $D_1 = (-1)^{w_f - 1} \sqrt{w_i w_f}$ and P_N and P_N' are two identical permutations, except that the former maps $\mathbf{r}_N$ into the source orbital l_i and the latter into the destination orbital l_f.

Eq. (A.8) involves a summation over permutations of coordinates, whereas coupling involves in general summations over magnetic quantum numbers. These two summations are thus interchangeable and the result of Eq. (A.13) can be applied to the reduced matrix element (A.11)

$$|\langle \gamma J || \hat{\mathcal{D}}^{(1)} || \gamma' J' \rangle|^2 = |D_1|^2 |\langle \psi_b^{P_N} || \mathbf{r}_N || \psi_{b'}^{P_N'} \rangle|^2 . \qquad (A.14)$$

The second coefficient, D_2, will remove the antisymmetry remaining within the source and the destination sub-shells l_i and l_f, but will not remove the coupling. The coupling will be removed by D_4.

$$D_2 = (l_i^{w_i}\alpha_i L_i S_i\{|l_i^{w_i-1}\alpha_i' L_i' S_i')(l_f^{w_f-1}\alpha_f L_f S_f|\}l_f^{w_f}\alpha_f' L_f' S_f'). \tag{A.15}$$

D_3 uncouples the total spin from the total orbital angular momentum since $\mathbf{r}_N$ does not couple to spin (Brink and Satchler 1993, 5.3), (Cowan 1981, 11-7)

$$D_3 = \delta_{\mathfrak{S}_q\mathfrak{S}_q'}(-1)^{\mathfrak{L}_q+\mathfrak{S}_q+\mathfrak{J}_q'+1}[\mathfrak{J}_q,\mathfrak{J}_q']^{1/2} \begin{Bmatrix} \mathfrak{L}_q & \mathfrak{S}_q & \mathfrak{J}_q \\ \mathfrak{J}_q' & 1 & \mathfrak{L}_q' \end{Bmatrix}. \tag{A.16}$$

With D_4 and D_5, the coupling chain is reordered again, such that it is identical up to the momenta l_i and l_f of the active coordinate $\mathbf{r}_N$. One electron is uncoupled from within the source orbital $[\mathfrak{L}_{i-1}\mathfrak{S}_{i-1}, (l_i^{w_i-1}L_i'S_i', l_i)L_iS_i]\mathfrak{L}_i\mathfrak{S}_i$ and re-coupled on top of the underlying orbitals as $[(\mathfrak{L}_{i-1}\mathfrak{S}_{i-1}, l_i^{w_i-1}L_i'S_i')\mathfrak{L}_i'\mathfrak{S}_i', l_i]\mathfrak{L}_i\mathfrak{S}_i$

$$D_4 = \left(\prod_{m=1}^{i-1} \delta_{\alpha_m L_m S_m, \alpha_m' L_m' S_m'}\delta_{\mathfrak{L}_m\mathfrak{S}_m, \mathfrak{L}_m'\mathfrak{S}_m'}\right)(-1)^{\mathfrak{L}_{i-1}+L_i'+l_i+\mathfrak{L}_i}\times$$
$$\times[\mathfrak{L}_i', L_i]^{1/2}\begin{Bmatrix}\mathfrak{L}_{i-1} & L_i' & \mathfrak{L}_i' \\ l_i & \mathfrak{L}_i & L_i\end{Bmatrix}\times \text{ spins} \tag{A.17}$$

l_i is still coupled inside $\mathfrak{L}_i$. It is uncoupled again and re-coupled onto the destination orbital $l_f^{w_f-1}$ to obtain $(l_f^{w_f-1}L_fS_f, l_i)L'S'$. The matrix element with the same orbital of the final configuration, $l_f^{w_f}L_f'S_f'$, is then evaluated.

$$\langle[(\mathfrak{L}_i'\mathfrak{S}_i', l_i)\mathfrak{L}_i\mathfrak{S}_i, L_fS_f]\mathfrak{L}_f\mathfrak{S}_f\|\mathbf{r}\|[\mathfrak{L}_i'\mathfrak{S}_i', (l_f^{w_f-1}L_fS_f, l_f)L_f'S_f']\mathfrak{L}_f'\mathfrak{S}_f'\rangle =$$
$$= \delta_{\mathfrak{S}_f, \mathfrak{S}_f'}(-1)^{\mathfrak{S}_{f-1}+\mathfrak{S}_f+S_f'}[\mathfrak{S}_{f-1}, S_f']^{1/2}\begin{Bmatrix}\mathfrak{S}_{f-1}' & S_f' & \mathfrak{S}_f \\ S_f & \mathfrak{S}_{f-1} & s\end{Bmatrix}\times$$
$$\times(-1)^{L_f+l_f+L_f'}[\mathfrak{L}_{f-1}, L_f', \mathfrak{L}_f, \mathfrak{L}_f']^{1/2}\begin{Bmatrix}\mathfrak{L}_{f-1} & \mathfrak{L}_{f-1}' & l_i \\ L_f & L_f' & l_f \\ \mathfrak{L}_f & \mathfrak{L}_f' & 1\end{Bmatrix}\langle l_i\|\mathbf{r}_N\|l_f\rangle =$$
$$= D_5\cdot\langle l_i\|\mathbf{r}_N\|l_f\rangle \tag{A.18}$$

where the intermediate summation over $L'S'$ has been left out (see D_7 in Cowan (1981, 14-13) for the missing step).

The average cross-section (A.5) requires the summation of (A.11) over all quantum numbers $L_m S_m \mathfrak{L}_m \mathfrak{S}_m$ of all states $\mathfrak{J}$ of the initial and final configuration, abbreviated so far by γJ and $\gamma' J'$ respectively

$$\sum_{\gamma J, \gamma' J'}\mathsf{S}_{\gamma J, \gamma' J'} = \sum_{\substack{L_1\mathfrak{L}_1 S_1\mathfrak{S}_1...L_q\mathfrak{L}_q S_q\mathfrak{S}_q\mathfrak{J}_q \\ L_1'\mathfrak{L}_1' S_1'\mathfrak{S}_1'...L_q'\mathfrak{L}_q' S_q'\mathfrak{S}_q'\mathfrak{J}_q'}}|D_1|^2\ldots|D_5|^2|\langle l_f\|\mathbf{r}_N\|l_i\rangle|^2 \tag{A.19}$$

For D_3, the orthogonality of the 6j symbols (Cowan 1981, 5-2) leads to

$$\sum_{\mathfrak{J}_q \mathfrak{J}'_q} |D_3|^2 = \delta_{\mathfrak{S}_q \mathfrak{S}'_q} \sum_{\mathfrak{J}_q} \frac{[\mathfrak{J}_q]}{[\mathfrak{L}_q]} = \delta_{\mathfrak{S}_q \mathfrak{S}'_q}[\mathfrak{S}_q] . \qquad (A.20)$$

Multiplication by D_5^2, summation over $\mathfrak{L}_q, \mathfrak{S}_q, \mathfrak{L}'_q$ and $\mathfrak{S}'_q$ and the orthogonality of the 9j symbols (Cowan 1981, 5-3) yield

$$\sum_{\substack{\mathfrak{L}_q \mathfrak{S}_q \mathfrak{J}_q \\ \mathfrak{L}'_q \mathfrak{S}'_q \mathfrak{J}'_q}} |D_3 D_5|^2 = \frac{[\mathfrak{L}_i, L'_f, \mathfrak{S}_i, S'_f]}{[l_i, l_f, s]} . \qquad (A.21)$$

Next indices in the row are $\mathfrak{L}'_{q-1} \mathfrak{S}'_{q-1}$ and $\mathfrak{L}_{q-1} \mathfrak{S}_{q-1}$, actually $\mathfrak{L}'_i \mathfrak{S}'_i$ and respectively $\mathfrak{L}_i \mathfrak{S}_i$, since the source orbital is now forelast $i = q - 1$. We multiply now by D_4^2. Summation over $\mathfrak{L}'_i \mathfrak{S}'_i$ leads to a series of δ's, additional summation over $\mathfrak{L}_i \mathfrak{S}_i$ leads to $\sum_{\mathfrak{L}_i \mathfrak{S}_i} [\mathfrak{L}_i \mathfrak{S}_i] = [\mathfrak{L}_{i-1}, L_i, \mathfrak{S}_{i-1} S_i]$.

$$\sum_{\substack{\mathfrak{L}_i \mathfrak{S}_i \mathfrak{L}_f \mathfrak{S}_f \mathfrak{J}_q \\ \mathfrak{L}'_i \mathfrak{S}'_i \mathfrak{L}'_f \mathfrak{S}'_f \mathfrak{J}'_q}} |D_3 D_5 D_4|^2 = \left(\prod_{m=1}^{i-1} \delta_{\alpha_m L_m S_m, \alpha'_m L'_m S'_m} \delta_{\mathfrak{L}_m \mathfrak{S}_m, \mathfrak{L}'_m \mathfrak{S}'_m} \right)$$

$$\frac{[\mathfrak{L}_{i-1}, L_i, \mathfrak{S}_{i-1} S_i, L'_f, S'_f]}{[l_i, l_f, s]} \quad (A.22)$$

Multiplication by D_2^2 and summation over $L'_i S'_i$ and $L_f S_f$ yields an unity due to the orthogonality of the cfp coefficients (Cowan 1981, §9.5). Summation over $\alpha_m L_m S_m \mathfrak{L}_m \mathfrak{S}_m \alpha'_m L'_m S'_m \mathfrak{L}'_m \mathfrak{S}'_m$ for $m = 1, i-1$ eliminates all δ factors from Eq. (A.22) leading to

$$\sum_{\substack{L_1 S_1 \mathfrak{L}_1 \mathfrak{S}_1 \dots L_f S_f \mathfrak{L}_f \mathfrak{S}_f \mathfrak{J}_q \\ L'_1 S'_1 \mathfrak{L}'_1 \mathfrak{S}'_1 \dots \quad \mathfrak{L}'_f \mathfrak{S}'_f \mathfrak{J}'_q}} = |D_3 D_5 D_4 D_2|^2 \sum_{L_1 S_1 \dots L_{f-1} S_{f-1}} \prod_{m=1}^{f-1} [L_m, S_m] \frac{[L'_f, S'_f]}{[l_i, l_f, s]} \qquad (A.23)$$

since

$$\sum_{\mathfrak{L}_1, \mathfrak{S}_1 \dots \mathfrak{L}_{i-1}, \mathfrak{S}_{i-1}} [\mathfrak{L}_{i-1}, \mathfrak{S}_{i-1}] = \prod_{m=1}^{i-1} [L_m, S_m] \qquad (A.24)$$

Each term in Eq. (A.23) represents the multiplicity of a final state with prescribed $L'_f S'_f$. Additional summation over $L'_f S'_f$ completes then the summation over all possible states of the given final configuration. The sum over the states of the initial configuration was also performed, but was largely eliminated by δ factors, as planed. Multiplication by D_1^2 and insertion into Eq. (A.5) for the average cross-section yields then

$$\sigma_{\text{avg}} = \frac{4}{3} \pi^2 \alpha \hbar \omega w_i w_f |\langle l_f \| \mathbf{r}_N \| l_i \rangle|^2$$

$$\times \frac{\left(\sum_{L_1 S_1 \dots L_{f-1} S_{f-1}} \prod_{m=1}^{f-1} [L_m, S_m] \right) \sum_{L'_f S'_f} \frac{[L'_f, S'_f]}{[l_i, l_f, s]}}{\left(\sum_{L_1 S_1 \dots L_{f-1} S_{f-1}} \prod_{m=1}^{f-1} [L_m, S_m] \right) \sum_{L_f S_f} [L_f, S_f]} . \quad (A.25)$$

When the final state is a Rydberg orbital or an ionized state in the continuum, the final orbital is unoccupied in the initial configuration, such that $L_f = S_f = 0$, whereas for the final configuration one has $L'_f = l_f$ and $S_f = s$. We apply once more the same operation that has been applied already with D_3 and D_5, namely the separation of spectator spaces (Brink and Satchler 1993, 5.3) in the reduced matrix element. In this case we separate the spectator radial coordinate r from the angular ones

$$\langle l_f \| \mathbf{r} \| l_i \rangle = (-1)^{l_f} [l_f, l_i]^{1/2} \begin{pmatrix} l_i & 1 & l_f \\ 0 & 0 & 0 \end{pmatrix} \int_0^\infty \phi_{n_i l_i}(r) \phi_{n_f l_f}(r) \mathrm{d}r \ ,$$

$$= (-1)^{l_i+1} \sqrt{l_i \pm 1} d_r(n_i, l_i; n_f, l_i \pm 1) \tag{A.26}$$

such that after adding both the contribution from the step up $l_f = l_i + 1$ and the step down $l_f = l_i - 1$ terms, the average cross-section becomes

$$\sigma_{\mathrm{avg}} = \frac{4\pi^2 \alpha \hbar \omega w_i}{3(2l_i + 1)} \big[(l_i + 1) d_r(n_i, l_i; n_f, l_i + 1)^2$$

$$+ (l_i - 1) d_r(n_i, l_i; n_f, l_i - 1)^2 \big] . \tag{A.27}$$

It depends only on the number of electrons in the initial orbital, its angular momentum l_i and on the single particle radial integrals

$$d_r(n_i, l_i; n_f, l_f) = \int_0^\infty \phi_{n_i l_i}(r) \phi_{n_f l_f}(r) \mathrm{d}r \ , \tag{A.28}$$

which can be evaluated directly with a HF code, such as Cowan's, available from `ftp://aphysics.lanl.gov/pub/cowan` and described in Cowan (1981).

Eq. (A.27) can actually be generalized for higher order transitions, such as E_2 or M_1. The dipole operator $e\mathbf{r}$ was used explicitly only in the last step, Eq. (A.26), where it has been assumed that it is a rank one tensor operator. The rest of the derivation is actually independent of the actual transition operator, as long as it remains a single particle operator.

Eq. (A.27) plays a central role for the screening approach described in Sec. 4.1.3 and Sec. 4.1.5. The interpolation procedure of Eq. (4.26) for the ionization potential E^*_{ip} of an ion screened by surrounding electrons, is actually just an approximation for the radial part of the screened wave functions. External screening weakens the attraction of the nucleus, such that the bound electrons delocalize. The radial component of the wave function is then expressed in terms of the radial component of an equivalent configuration of less total charge, whose bound electrons are delocalized *naturally* due to the reciprocal repulsion. The screened photo-ionization cross-section can be approximated similarly. According to Eq. (A.5), only the occupation number w_{active} and the radial integrals d_r are needed. The latter can be copied by the above prescription from σ_{avg} of the equivalent configuration, such that the screened cross-section can be obtained from the one of the equivalent configuration by simple exchange of the occupation number

$$\sigma^{\mathrm{scr}}_{\mathrm{avg}} = \frac{w_{\mathrm{active}}}{w_i} \cdot \sigma_{\mathrm{avg}} \tag{A.29}$$

Appendix B

The cluster potential landscape

The goal is to calculate the average cluster potential as seen by a bound electron to be ionized. According to the time scale separation introduced in Chapter 4, the properties of the cluster environment have to be averaged over the natural time scale given by the mean revolution periods T_i of the localized electrons.

The average cluster potential is determined by the time averaged charge distribution, which is cumulated on a three dimensional grid during a time interval T_i. Renormalization to the number of time steps and the volume of a grid cell yields the average charge density in the cluster for the next time interval T_{i+1}. The spacing is chosen such, that there are 8 grid points between the closest two atoms in the system. The size of the grid is adjusted automatically and allows for a buffer of at least 16 points between the outermost atom of the cluster and the grid boundary[1].

The Poisson equation with open boundary conditions can be solved with the method of the image charges (James 1977). Because the model potentials used in this work no longer obey a Poisson equation, we resort to solving the full three-dimensional convolution problem

$$\phi_{ijk} = \sum_{rst} q_{rst} g_{i-r,j-s,t-k} \tag{B.1}$$

by means of a Fourier ansatz similar to that of James (1977). q_{rst} is the charge, not the density of the cell and $g_{jkl} = g(\sqrt{i^2 + j^2 + k^2})$ is the generator of the spherically symmetric potential, such as the U-shaped (4.37), the V-shaped (4.40) or the Coulomb one. Special care needs to be taken here because periodic boundary conditions do not hold for g_{jkl}.

We will illustrate the approach in one dimension and then switch over to the full 3D problem, where the special requirements of `FFTW` (FFT 2008), the library used to perform the FFT, are considered.

The generator $g(r)$ of the spherically symmetric potential is an even function, for which reason its Fourier transform will reduce to an expansion in cosine functions,

---

[1]Outermost atoms are dropped from the cluster when the separation is large enough, that the grid based method and a simple two body estimation of the barrier lowering yield the same results.

such as

$$g_i = \sum_{\alpha=0}^{n-1} g^\alpha \cos \frac{i\alpha\pi}{n} \,. \tag{B.2}$$

Eq. (B.2) is actually wrong. While it preserves the symmetry properties at the origin, it automatically assumes periodic boundary conditions for g_i. Later on, the correct expansion under the correct boundary conditions will be introduced and used, but for illustration purposes this form is more compact. Inserting (B.2) in the one-dimensional Eq. (B.1) one obtains

$$
\begin{aligned}
\phi_i &= \sum_r q_r \sum_{\alpha=0}^{n-1} g^\alpha \cos \frac{(i-r)\alpha\pi}{n} \\
&= \sum_{\alpha=0}^{n-1} g^\alpha \sum_r q_r \left(\cos \frac{i\alpha\pi}{n} \cos \frac{r\alpha\pi}{n} + \sin \frac{i\alpha\pi}{n} \sin \frac{r\alpha\pi}{n} \right) \\
&= \sum_{\alpha=0}^{n-1} g^\alpha \left(\cos \frac{i\alpha\pi}{n} \sum_r q_r \cos \frac{r\alpha\pi}{n} + \sin \frac{i\alpha\pi}{n} \sum_r q_r \sin \frac{r\alpha\pi}{n} \right) \\
&= \sum_{\alpha=0}^{n-1} g^\alpha q_c^\alpha \cos \frac{i\alpha\pi}{n} + \sum_{\alpha=0}^{n-1} g^\alpha q_s^\alpha \sin \frac{i\alpha\pi}{n} \,,
\end{aligned}
\tag{B.3}
$$

where the c and s subscripts denote cosine- and respectively sine-expansions.

Eq. (B.3) conveys the general idea that a convolution can still be performed efficiently in the Fourier space when one of the functions can only be expanded in cosines.

Throughout this work C/C++, or zero based indexing will be used for all vectors.

The correct way to formulate a discrete Fourier transform (DFT) for g_i is to extend it by reflection about the last element

$$g_i' = g_{N-i}' = g_i, \quad i = 1 \ldots n-1, \; N = 2(n-1) \,. \tag{B.4}$$

The new vector g' obeys now periodic boundary conditions $g_i' = g_{N+i}'$, such that the Fourier transform is simply

$$g'^\alpha = \sum_{j=0}^{N-1} g_j' \exp\left(2\pi i \frac{j\alpha}{N} \right) \,. \tag{B.5}$$

g' is by Eq. (B.4) even symmetric, such that the summation in (B.5) can be reduced to

$$
\begin{aligned}
g'^\alpha &= g_0' + (-1)^\alpha g_{N/2} + \sum_{j=1}^{N/2-1} g_j' \left[\exp\left(2\pi i \frac{j\alpha}{N} \right) + \exp\left(2\pi i \frac{(N-j)\alpha}{N} \right) \right] \\
&= g_0' + (-1)^\alpha g_{n-1} + 2 \sum_{j=1}^{n-2} g_j' \cos \frac{j\alpha\pi}{n-1} \,.
\end{aligned}
\tag{B.6}
$$

g'^α is obviously also even symmetric; insert $\alpha \to N - \alpha = 2(n-1) - \alpha$ in Eq. (B.6). Eliminating the redundant elements of g' and g'^α the *discrete cosine transform* (DCT) is obtained

$$g^\alpha = g_0 + (-1)^\alpha g_{n-1} + 2 \sum_{j=1}^{n-2} g_j \cos \frac{j\alpha\pi}{n-1} . \tag{B.7}$$

The inverse DCT or, in other words, the expansion of g_i in a series of cosine functions has the same structure, but will be stated explicitly for reference

$$g_j = \sum_{\alpha=0}^{n-1} w(\alpha) g^\alpha \cos \frac{j\alpha\pi}{n-1} , \tag{B.8}$$

where the weightings $w(\alpha)$ have been introduced for compactness

$$w(\alpha) = \begin{cases} 1 & \alpha = 0, n-1 \\ 2 & \text{otherwise.} \end{cases} \tag{B.9}$$

The overall normalization constant is $1/N = 1/2(n-1)$. It is also clear now that choosing n as customary a power of two will not achieve the highest performance, but $n = 2^m + 1$. The FFT algorithm is actually being performed on g', hence N, not n, should be either power of two, or at least a multiple of small prime numbers.

The DCT is just a particular case of a DFT, where the symmetry of the input, in this case the even symmetric input vector g' of size N, has been used to reduce the amount of storage to $N/2 + 1$, at the same time reducing the computation time. The other way around: based on the way the given vector g_i should be expanded to the periodic g_i', four kinds of DCTs can be distinguished (from (FFT 2008))

- DCT-I: even around $j = 0$ and even around $j = n - 1$.

- DCT-II, the DCT: even around $j = -0.5$ and even around $j = n - 0.5$.

- DCT-III, the IDCT: even around $j = 0$ and odd around $j = n$.

- DCT-IV: even around $j = -0.5$ and odd around $j = n - 0.5$.

If $g(r)$ were odd, Eq. (B.6) would yield an expansion in sine functions, which can again be classified into

- DST-I: odd around $j = -1$ and odd around $j = n$.

- DST-II: odd around $j = -0.5$ and odd around $j = n - 0.5$.

- DST-III: odd around $j = -1$ and even around $j = n - 1$.

- DST-IV: odd around $j = -0.5$ and even around $j = n - 0.5$.

In the following the type-I DST (DST-I) will be needed. The input vector g_j has n elements $g_{0...n-1}$ and the boundary conditions are $g_{-1} = g_n = 0$. For storage and speed reasons, FFTW does not store the zero elements explicitly. The expansion g' has $N = 2(n+1)$ elements and is odd symmetric

$$g'_j = -g'_{N-j} \, . \tag{B.10}$$

The elements of g_j have also been shifted by one $g'_{j+1} = g_j$, $j = 0 \ldots n-1$ to explicitly include the boundary conditions $g'_0 = g_{-1} = 0$ and respectively $g'_{n+1} = g_n = 0$. Inserting into Eq. (B.5) one obtains

$$
\begin{aligned}
g'^\alpha &= \sum_{j=0}^{N/2-1} g'_j \left[\exp\left(2\pi i \frac{j\alpha}{N} \right) - \exp\left(2\pi i \frac{(N-j)\alpha}{N} \right) \right] \\
&= 2i \sum_{j=0}^{n} g'_j \sin \frac{j\alpha\pi}{n+1}
\end{aligned}
\tag{B.11}
$$

Because g'^α is also odd symmetric ($g'^{N-\alpha} = g'^{2(n+1)-\alpha} = -g'^\alpha$), performing the inverse Fourier transform on g'^α yields basically the same formula but with the opposite sign

$$g'_j = -2i \sum_{\alpha=0}^{n} g'_j \sin \frac{j\alpha\pi}{n+1} \tag{B.12}$$

Eliminating the redundant elements in g'_j and g'^α, including the zeros, the DST-I transform can be defined

$$g^\alpha = 2 \sum_{j=0}^{n-1} g_j \sin \frac{(j+1)(\alpha+1)\pi}{n+1} \, . \tag{B.13}$$

The imaginary pre-factors i and respectively $-i$ have been removed for symmetry reasons. Again, for reference, the inverse DST-I reads

$$g_j = 2 \sum_{\alpha=0}^{n-1} g^\alpha \sin \frac{(\alpha+1)(j+1)\pi}{n+1} \, . \tag{B.14}$$

The normalization factor is in this case $1/N = 1/2(n+1)$ and highest performance is achieved for $n = 2^m - 1$.

Inserting the DCT-I expansion of the generator $g(r)$ in Eq. (B.1) and applying the cosine sum rule as in (B.3), a series of eight distinct transforms of the charge distribution q_{rst} can be isolated, according to whether a cosine or a sine transform is

performed along each space coordinate

$$\phi_{jkl} = \sum_{r,s,t=0}^{n-1} q_{rst} g_{j-r,k-s,l-t} = \sum_{\alpha\beta\gamma} w(\alpha)w(\beta)w(\gamma) g^{\alpha\beta\gamma} \times$$

$$\left\{ \cos\frac{j\alpha\pi}{n-1} \cos\frac{k\beta\pi}{n-1} \cos\frac{l\gamma\pi}{n-1} \sum_{rst} \cos\frac{r\alpha\pi}{n-1} \cos\frac{s\beta\pi}{n-1} \cos\frac{t\gamma\pi}{n-1} + \right.$$

$$+ \; \mathsf{CCS} + \mathsf{CSC} + \mathsf{SCC} + \mathsf{CSS} + \mathsf{SCS} + \mathsf{SSC} +$$

$$\left. + \sin\frac{j\alpha\pi}{n-1} \sin\frac{k\beta\pi}{n-1} \sin\frac{l\gamma\pi}{n-1} \sum_{rst} \sin\frac{r\alpha\pi}{n-1} \sin\frac{s\beta\pi}{n-1} \sin\frac{t\gamma\pi}{n-1} \right\}, \quad \text{(B.15)}$$

where the CCSs abbreviate the respective cosine or sine terms. The summations about the rst indices can be contracted to individual DCT and/or DST transforms of the charge distribution. The CCS term yields for example

$$h^{\alpha\beta\gamma}(\mathsf{ccs}) = \sum_{rst=0}^{n-1} q_{rst} \cos\frac{r\alpha\pi}{n-1} \cos\frac{s\beta\pi}{n-1} \sin\frac{t\gamma\pi}{n-1} =$$

$$= \frac{1}{8} \sum_{rst=0}^{n-1} \left[w(r) + \delta_{r,0} + \delta_{r,n-1} \right] \left[w(s) + \delta_{s,0} + \delta_{s,n-1} \right] w(t) \times$$

$$\times \cos\left(\frac{r\alpha\pi}{n-1}\right) \cos\left(\frac{s\beta\pi}{n-1}\right) \sin\left(\frac{t\gamma\pi}{n-1}\right) q_{rst}$$

$$= \frac{1}{8} \left[q^{\alpha\beta\gamma}(\mathsf{ccs}) + c_r^{\alpha} \cdot q_r{}^{\beta\gamma}(\mathsf{cs}) + c_s^{\beta} \cdot q^{\alpha}{}_s{}^{\gamma}(\mathsf{cs}) + c_r^{\alpha} c_s^{\beta} \cdot q_{rs}{}^{\gamma}(\mathsf{s}) \right].$$

$$\text{(B.16)}$$

The sine term vanishes for $t = 0$ and $t = n-1$, such that according to Eq. (B.13) a DST-I transform of size $n-2$ along the z direction is obtained. The upper indices denote the coordinates in the Fourier space, the lower ones in the direct space. $q_r{}^{\beta\gamma}(\mathsf{cs})$ is for example a 2D transform in a yz plane with a DCT along the y axis and a DST along z. The coefficients c_r^{α} select the plane, actually the face of the cube, and the phase

$$c_r^{\alpha} = \delta_{r,0} + (-1)^{\alpha} \delta_{r,n-1}. \quad \text{(B.17)}$$

A product of two c_a^b coefficients selects an edge, three of them selects a corner. The transforms generated by the other seven terms of Eq. (B.15) are summarized in Eq. (B.18)

$$h^{\alpha\beta\gamma}(\mathsf{ccc}) = \frac{1}{8}\Big[q^{\alpha\beta\gamma}(\mathsf{ccc}) + c_r^{\alpha}\cdot q_r{}^{\beta\gamma}(\mathsf{cc}) + c_s^{\beta}\cdot q^{\alpha}{}_s{}^{\gamma}(\mathsf{cc}) + c_t^{\gamma}\cdot q^{\alpha\beta}{}_t(\mathsf{cc})+$$
$$+ c_r^{\alpha}c_s^{\beta}\cdot q_{rs}{}^{\gamma}(\mathsf{c}) + c_s^{\beta}c_t^{\gamma}\cdot q^{\alpha}{}_{st}(\mathsf{c}) + c_r^{\alpha}c_t^{\gamma}\cdot q_r{}^{\beta}{}_t(\mathsf{c}) + c_r^{\alpha}c_s^{\beta}c_t^{\gamma}\Big]$$

$$h^{\alpha\beta\gamma}(\mathsf{csc}) = \frac{1}{8}\Big[q^{\alpha\beta\gamma}(\mathsf{csc}) + c_r^{\alpha}\cdot q_r{}^{\beta\gamma}(\mathsf{sc}) + c_t^{\gamma}\cdot q^{\alpha\beta}{}_t(\mathsf{cs}) + c_r^{\alpha}c_t^{\gamma}\cdot q_r{}^{\beta}{}_t(\mathsf{s})\Big]$$

$$h^{\alpha\beta\gamma}(\mathsf{scc}) = \frac{1}{8}\Big[q^{\alpha\beta\gamma}(\mathsf{scc}) + c_s^{\beta}\cdot q^{\alpha}{}_s{}^{\gamma}(\mathsf{sc}) + c_t^{\gamma}\cdot q^{\alpha\beta}{}_t(\mathsf{sc}) + c_s^{\beta}c_t^{\gamma}\cdot q^{\alpha}{}_{st}(\mathsf{s})\Big]$$

$$h^{\alpha\beta\gamma}(\mathsf{css}) = \frac{1}{8}\Big[q^{\alpha\beta\gamma}(\mathsf{css}) + c_r^{\alpha}\cdot q_r{}^{\beta\gamma}(\mathsf{ss})\Big] \qquad . \quad \text{(B.18)}$$

$$h^{\alpha\beta\gamma}(\mathsf{scs}) = \frac{1}{8}\Big[q^{\alpha\beta\gamma}(\mathsf{scs}) + c_s^{\beta}\cdot q^{\alpha}{}_s{}^{\gamma}(\mathsf{ss})\Big]$$

$$h^{\alpha\beta\gamma}(\mathsf{ssc}) = \frac{1}{8}\Big[q^{\alpha\beta\gamma}(\mathsf{ssc}) + c_t^{\gamma}\cdot q^{\alpha\beta}{}_t(\mathsf{ss})\Big]$$

$$h^{\alpha\beta\gamma}(\mathsf{sss}) = \frac{1}{8}q^{\alpha\beta\gamma}(\mathsf{sss})$$

Inserting the $h^{\alpha\beta\gamma}(\cdots)$'s back into Eq. (B.15), one recognizes the backwards transforms of the inner tensor products $g^{\alpha\beta\gamma}\odot h^{\alpha\beta\gamma}(\cdots)$ and the potential ϕ_{jkl} in the direct space is obtained

$$\phi_{jkl} = \sum_{\alpha\beta\gamma} w(\alpha)w(\beta)w(\gamma)g^{\alpha\beta\gamma}\times$$
$$\times\Big\{\cos\frac{j\alpha\pi}{n-1}\cos\frac{k\beta\pi}{n-1}\cos\frac{l\gamma\pi}{n-1}\cdot h^{\alpha\beta\gamma}(\mathsf{ccc})+$$
$$+ \mathsf{CCS} + \mathsf{CSC} + \mathsf{SCC} + \mathsf{CSS} + \mathsf{SCS} + \mathsf{SSC}+ \qquad \text{(B.19)}$$
$$+ \sin\frac{j\alpha\pi}{n-1}\sin\frac{k\beta\pi}{n-1}\sin\frac{l\gamma\pi}{n-1}\cdot h^{\alpha\beta\gamma}(\mathsf{sss})\Big\}$$
$$= \mathcal{F}_{\mathsf{ccc}}[g^{\alpha\beta\gamma}\odot h^{\alpha\beta\gamma}(\mathsf{ccc})] + \ldots + \mathcal{F}_{\mathsf{sss}}[g^{\alpha\beta\gamma}\odot h^{\alpha\beta\gamma}(\mathsf{sss})]\,.$$

The overall calculation is quite involved. For the forward step eight three dimensional DFTs over the whole grid volume need to be performed, 48 over the faces and 96 along the edges. And just as many for the backward step. The FFTW API allows one to group these together, such that all faces or edges corresponding to a certain transform, such as CSC, can be transformed with a single function call.

Fig. B.1 shows a simple verification on a $33\times33\times33$ grid. $n = 2^m + 1$ is optimal for both the DCT-I and the DST-I transform, since the effective size of the latter is $n-2$. A single charge $q = +1$ has been placed at various critical spots on the grid and the result of the convolution is compared with the direct calculation. This way one can ensure that no face, edge, or corner has been skipped, either during the forward or during the backward Fourier transforms, nor have any indices been reversed, in which case a charge at one side of the grid would generate a potential centered at the opposite side.

The method of the image charges mentioned above would have saved all three-dimensional transforms but SSS. The simplest finite difference representation of the
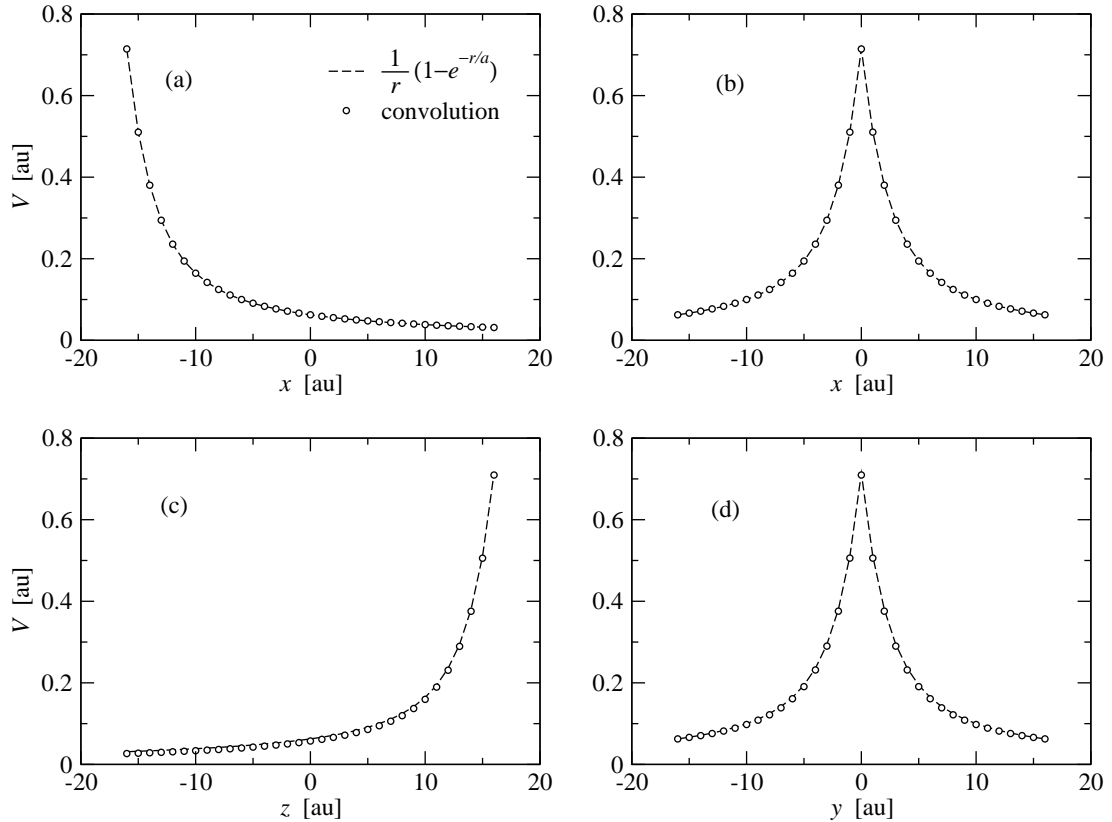
Figure B.1: Simple checks of the Fourier based implementation on a $33 \times 33 \times 33$ grid with spacing $\Delta x = \Delta y = \Delta z = 1$. A single charge $q = +1$ has been placed at critical spots on the grid, such as corners, faces or center, to check for possible summation errors or missing terms. The generator $g(r)$ was the v-shaped potential Eq. (4.40) for $a = 1.4$. $\circ$: numerical convolution; dashed line: direct plot. (a) charge at a corner, $(-16, -16, -16)$, V along the $(x, -16, -16)$ line is shown; (b) grid center, $(0, 0, 0)$, V along $(x, 0, 0)$; (c) on the $(x, y, 16)$ face, at $(0, 0, 16)$, V along $(0, 0, z)$; (d) the same, V along $(0, y, 16)$.

Poisson equation is

$$\left(\Delta x^{-2} \delta_x^2 + \Delta y^{-2} \delta_y^2 + \Delta y^{-2} \delta_y^2 \right) \varphi_{jkl} = -4\pi \rho_{jkl} \tag{B.20}$$

where $\delta_x^2 = \{ \cdot \}_{j+1} + \{ \cdot \}_{j-1} - 2\{ \cdot \}_j$ is the differencing operator.

One simulates a grounded metallic layer around the grid by taking zero Dirichlet boundary conditions for φ_{jkl}. Only sine expansions along each coordinate are required in this case and the Poisson equation in the Fourier space reads simply

$$\phi^{\alpha\beta\gamma} = q^{\alpha\beta\gamma} / C^{\alpha\beta\gamma} \tag{B.21}$$

with

$$C^{\alpha\beta\gamma} = \frac{\Delta x \Delta y \Delta z}{2\pi} \left[\frac{1}{\Delta x^2} \left(1 - \cos \frac{\alpha\pi}{n-1} \right) + \frac{1}{\Delta y^2} \left(1 - \cos \frac{\beta\pi}{n-1} \right) + \right.$$
$$\left. + \frac{1}{\Delta z^2} \left(1 - \cos \frac{\gamma\pi}{n-1} \right) \right] . \quad \text{(B.22)}$$

Applying Eq. (B.20) one finds a set of induced charges on the "metallic" boundary which is different from the prescribed ones. Thus, one can consider the prescribed charge distribution as a superposition of the one which generates ϕ and some corrections charges δq. Obviously, the potential $\delta\phi$ arising from the later needs to be added to ϕ to obtain the full free space potential φ. $\delta\phi$ is obtained from δq by performing the full three-dimensional convolution (B.1), which simplifies to the set of 48 two- and 96 one-dimensional transforms selected by the c_r^α coefficients in Eqs. (B.16) and (B.18) because the distribution δq is hollow.

Appendix C

Inverse bremsstrahlung in one dimension

Classical propagation of Coulomb particles faces the problem of the singular potential at nucleus. If two electrons collide close to a positive ion, one of the electrons can fall onto a state of very low energy and the other one will be ionized with the energy difference. The same phenomenon is known from stellar dynamics, where three-star encounters can lead to formation of binaries. But if the singularity of the potential represents there just a numerical overhead, requesting for propagation with very small time steps at close encounters, it becomes a fundamental problem for ion-electron binaries. Quantum mechanics sets a lower limit for the total energy of the interaction, namely the energy of the lowest bound state, the ground state.

The simplest non-singular approximation to the Coulomb interaction is the *soft-core* potential

$$U(r) = \frac{1}{r^2 + a^2},\tag{C.1}$$

which was already introduced in Sec. 4.2. In molecular dynamics a is usually chosen such that the depth Z/a of the potential well corresponds to the ground state ionization potential of the bound electron-ion system

$$E_{\mathrm{ip}}^{(Z-1)} = \frac{Z}{a}.\tag{C.2}$$

The soft-core potential $U(r)$ becomes harmonic close to the nucleus with the eigenfrequency $\omega_0 = \sqrt{Z/a^3}$. If a low energy particle is trapped in this effectively quadratic region of the potential well, resonance phenomena can arise when an oscillating external field is applied. To avoid this artifact, a new model potential was introduced, which is not derivable at origin

$$V(r) = -\frac{Z}{r}(1 - e^{r/a})\tag{C.3}$$

and whose *eigenfrequency* diverges (Eq. (4.41))

$$\lim_{E \to -Z/a} \omega_V = \lim_{E \to -\frac{Z}{a}} \frac{\pi}{4}\sqrt{\frac{Z}{a}}\left(E + \frac{Z}{a}\right)^{-\frac{1}{2}} = \infty.\tag{C.4}$$

A frequency dependent study of the energy absorption and ionization in clusters for the two model potentials $U(r)$ and $V(r)$ could not reveal any resonance like behavior. The only significant difference they have introduced was the height of the ionization thresholds, which are generally lower for $U(r)$ (see Fig. 4.9) and enhance inner ionization. Outer ionization, as well as the IBS absorption per inner-ionized electron were practically identical.

To extend the knowledge about the role of the interacting potential when a driving field is present, we have continued our investigations to a very simple system: the one dimensional motion of a single bound electron in the presence of a laser field. A typical result is shown in Fig. C.1 for the Coulomb potential. Each full line shows the final energy E_f of the electron after the interaction with a laser pulse as a function of the laser frequency ω for a given initial energy E_i. The $\sin^2$ pulses are 1.18 fs long, which corresponds to a 10 cycle pulse at $\hbar\omega = 0.47$ au $= 12.7$ eV. The frequency of the laser is then increased in cycle steps, until $\hbar\omega = 2.82$ au $= 76.73$ eV is reached, corresponding to 60 cycles within the same time frame. All pulses have the same intensity $I = 7 \times 10^{13}$ W/cm^2. The final energy E_f is averaged over 150 initial conditions, which are evenly distributed along the closed trajectory $E = E_i$ in phase space. The core singularity of the Coulomb potential is removed by means of a canonical coordinate transform. A detailed description of the numerical methods employed will follow at the end of this section.
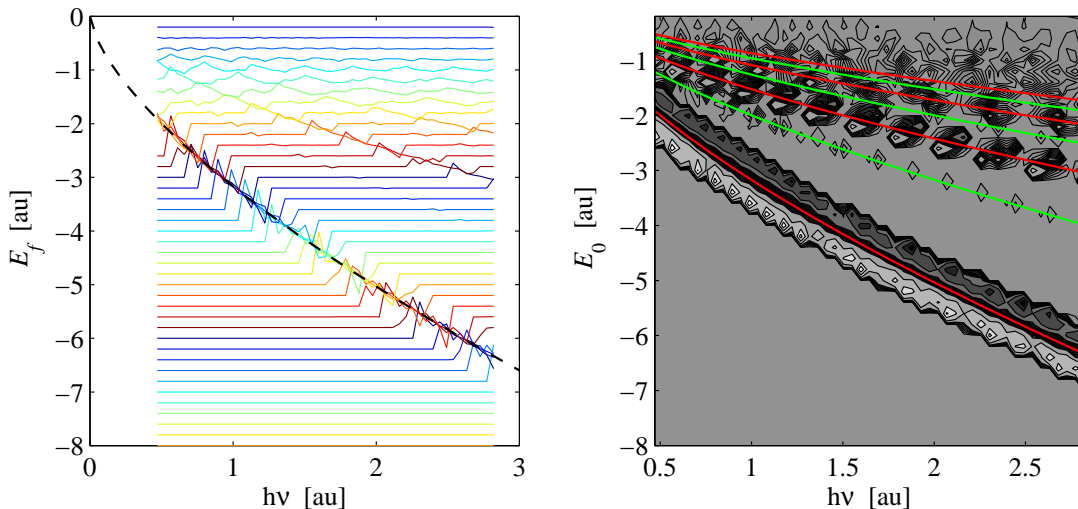
Figure C.1: One dimensional motion of an electron trapped in a Coulomb well $Z = 8$ and driven by a laser field, $I = 7 \times 10^{13}$ W/cm^2, $T = 1.18$ fs. Left: final energy E_f averaged over 150 initial conditions; each line depicts E_f as a function of the laser frequency ν for a given initial energy E_i; dashed line: frequency ω_C as in Eq. (C.5) of periodic motion in the potential well as function of the particle energy (swapped axes). Right: contour map of the absorbed energy $E_f - E_i$; red lines: odd harmonics, green: even harmonics.

The initial energy E_i needed not be shown, as for most of the frequencies no energy

was absorbed on average and $E_f = E_i$. When $E_f \neq E_i$, an interesting phenomenon of auto-resonance is observed. If the laser frequency is less than the frequency ω_C of the electron motion in the Coulomb field, the electron absorbs energy from the field. If on the other hand the field is faster, the electron is decelerated and pushed down into the potential well. ω_C varies non-linearly with the total energy E, decreasing with increasing E and vice-versa

$$\omega_C = \sqrt{\frac{-E^3}{32}} . \tag{C.5}$$

Hence, sub-resonant laser frequencies drag the electron onto orbits of higher energy E, until $\omega_C(E)$ is lowered to ω. The electron is then locked onto this orbit, as the rate of energy absorption and return become equal also. Over-resonant ω behaves similarly, pushing the electron to lower energy. The envelope of the "lock" segments, where the electron oscillates with the laser, is identical with the analytical expression for $\omega_C(E)$, which is shown with a dashed line. The response at higher harmonics can also be observed, as emphasized by the contour map on the right hand side of Fig. C.1. The red lines depict the odd harmonics, the green lines the even ones, which tend to be cancelled due to the symmetry of the potential.
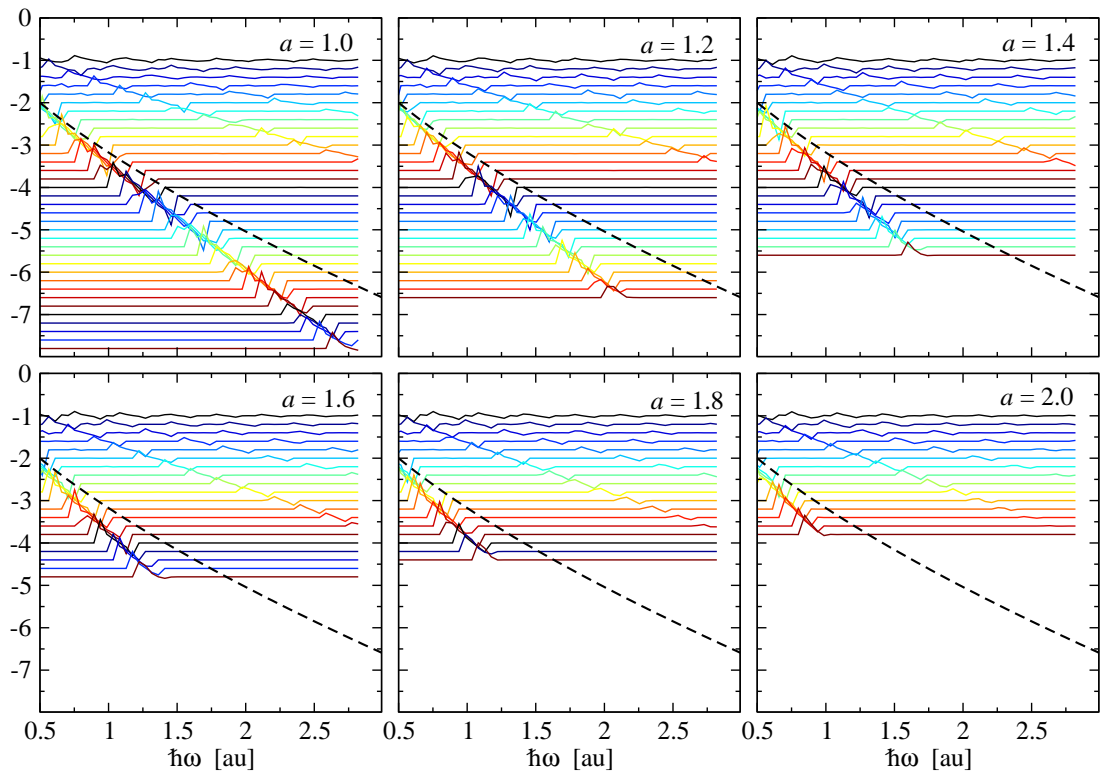
Figure C.2: Same as Fig. C.1, but for $U(r)$ from Eq. (C.1) and several parameters a.

The effect is similar to an auto-resonance effect proposed for the plasma beat-wave accelerator (PBWA) (Lindberg et al. 2004), where a plasma wave is phase-locked to the beating of two co-propagating lasers. A small chirp on one of the beams

drives the phased-locked plasma wave through the plasma resonance. The acceleration process becomes thus more robust against fluctuations of the plasma frequency and accelerating fields beyond 250 GV/m are achieved.

The one-dimensional behavior of the $U(r)$ and $V(r)$ potentials has also been studied, with results shown in Fig. C.2 and Fig. C.3, respectively. Emphasis has been put on studying the behavior of the electron when the initial energy approached the bottom of the potential well $E_i \to -Z/a$, where the energy of the electron can no longer be lowered. $U(r)$ shows here resonant behavior, as the frequency of the electron motion becomes independent of energy. Maximum absorption occurs as expected when the laser frequency is close to the eigenfrequency of the harmonic potential $\omega \to \sqrt{Z/a^3}$. Comparing to Fig. C.1, one can state the response of $U(r)$ is similar to the Coulomb potential in magnitude, but for the wrong frequency. $V(r)$ shows a different behavior, where the frequency of the auto-resonance tends to follow the Coulomb limit, but the magnitude diminishes as E_i approaches the bottom of the well.
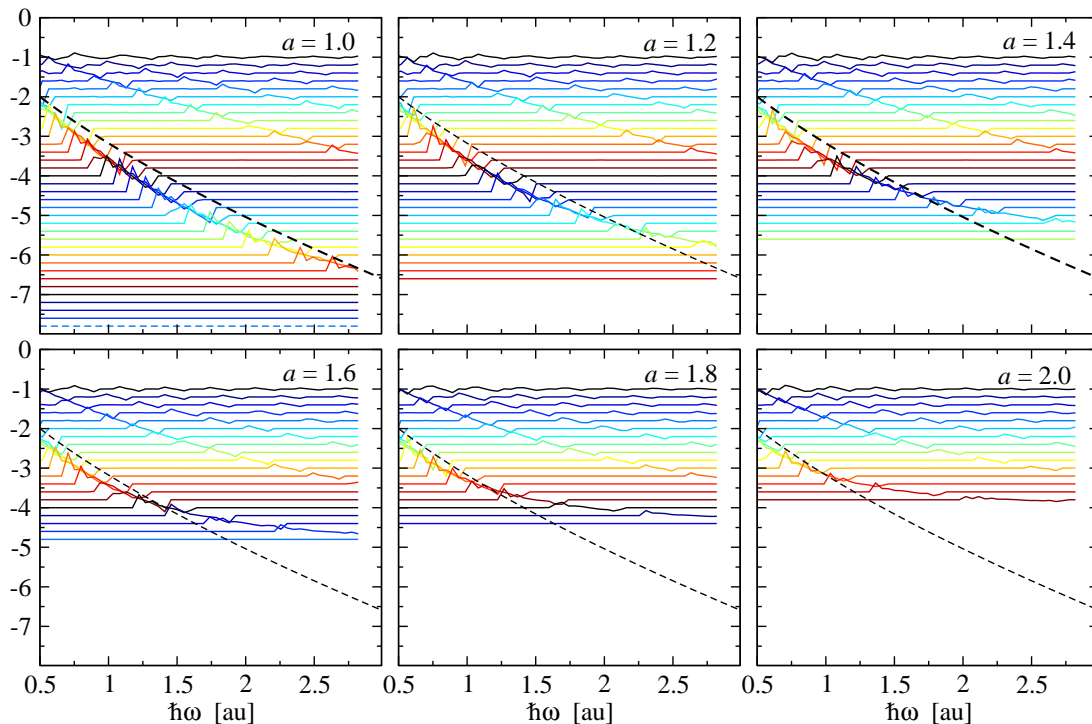
Figure C.3: Same as Fig. C.1 or Fig. C.2, but for $V(r)$ from Eq. (C.3) and the same parameters a as in Fig. C.2.

A decision in a favor of the one or the other potential cannot be made easily. Our three-dimensional frequency dependent investigations for Ar_{147} in Sec. 5.2, Fig. 5.8, could not relate the response, that is IBS absorption per quasi-free electron, to any shape specific, resonant or non-resonant behavior. Therefore, one should always check for possible changes in the outcome of MD simulations when the model potential is changed. This is negligible with IR fields, but not in cold dense systems, such as the

ones encountered in this work.

As mentioned above, the energy absorption was averaged over 150 initial conditions (q_i, p_i) for each initial energy E_i and laser frequency ω. These were generated in the canonical action-angle variables representation, by choosing evenly distributed initial angles, or phases θ in the interval $[0, 2\pi)$. The phase of the laser pulse was in turn kept constant. By definition (Landau and Lifshitz 2005, §50), one has

$$
\begin{aligned}
I &= \frac{1}{2\pi} \oint p \mathrm{d}q \\
\theta &= \frac{\partial S_0(q, I, \lambda)}{\partial I} = \frac{2\pi}{T} t + \text{const.} \\
&= \frac{2\pi}{T} \int_0^q \frac{\mathrm{d}q'}{\partial H / \partial p} = \frac{2\pi}{T} \int_0^q \frac{m \mathrm{d}q'}{\sqrt{2m(E - V(q'))}} \,,
\end{aligned}
\tag{C.6}
$$

where $S_0(q, I, \lambda) = \int p(q', I, \lambda)\mathrm{d}q'$ is the action, I is the action variable and λ is a slowly varying parameter describing external fields and that can be assumed constant over one period of motion. The last equation is solved numerically to generate the initial conditions $(q_i(\theta_i), p_i(\theta_i))$ for a given initial phase θ_i, not only for the Coulomb potential, but also for $U(q)$ and $V(q)$.

Alternatively, one could hold (q_i, p_i) constant and only vary the phase, or the delay of the laser. Though easier, it is longer guaranteed that the phase space is explored in a uniform manner due to the non-constant angular velocity. Regions of lower angular velocity $\dot{\theta} = L/mr^2 \sin\theta$ would be sampled more often than others.

The equations of motion are then integrated in slightly more general framework, which allows one to implement an adaptive time step. One introduces a fictitious time τ (Preto and Tremaine 1999)

$$
\mathrm{d}t = g(\mathbf{q}, \mathbf{p}, t)\mathrm{d}\tau
\tag{C.7}
$$

and takes $t \equiv q_0$ as a new coordinate with the conjugate momentum $p_0 = -H$. The equations of motion in the extended phase space $\mathbf{Q} = (q_0, \mathbf{q})$, $\mathbf{P} = (p_0, \mathbf{p})$ read now

$$
\begin{aligned}
\frac{\mathrm{d}\mathbf{Q}}{\mathrm{d}\tau} &= g(\mathbf{q}, \mathbf{p}, t)\frac{\partial H}{\partial \mathbf{p}} = \frac{\partial \Gamma}{\partial \mathbf{P}} \\
\frac{\mathrm{d}\mathbf{P}}{\mathrm{d}\tau} &= -g(\mathbf{q}, \mathbf{p}, t)\frac{\partial H}{\partial \mathbf{q}} = -\frac{\partial \Gamma}{\partial \mathbf{Q}}
\end{aligned}
\tag{C.8}
$$

with the new Hamiltonian

$$
\Gamma(\mathbf{Q}, \mathbf{P}) = g(\mathbf{q}, \mathbf{p}, q_0)\big(H(\mathbf{q}, \mathbf{p}, q_0) + p_0\big) \,.
\tag{C.9}
$$

Only those solutions on the hyper-surface $\Gamma = 0$ correspond to the trajectories in the original phase space. The fixed time step integration in the extended phase space corresponds thus a variable step integration $\Delta t = g(\mathbf{q}, \mathbf{p}, t)\Delta\tau$ in the reduced phase space.

Starting from the Hamiltonian of a single electron in a potential well $V(r)$ and an oscillating electric field $E_q(t) = E_0 \sin \omega t$

$$H = \frac{p^2}{2} + V(q) - qE_0 \sin \omega t \,, \tag{C.10}$$

we perform a generic canonical transform under the generator $F_3(Q, p) = -pf(Q)$, where $q = \partial F(Q, p)/\partial p$ and $P = -\partial F(Q, p)/\partial Q$. $g(Q) = [f'(Q)]^2$ is then inserted in equations (C.8) and (C.9), thereby extending the phase space to $\mathbf{Q} = (t, Q)$, $\mathbf{P} = (p_0, P)$ with the new Hamiltonian

$$\Gamma' = \frac{P^2}{2} + \left[f'(Q)\right]^2 V(f(Q)) - f(Q)\left[f'(Q)\right]^2 E_q(t) + p_0\left[f'(Q)\right]^2. \tag{C.11}$$

For $f(Q) = Q^3/|Q|$, one obtains $q = Q^3/|Q|$ and $p = P/2|Q|$, such that for the Coulomb potential $V(q) = -Z/|q|$, the new Hamiltonian becomes

$$\Gamma' = \frac{P^2}{2} - 4Z + 4p_0Q^2 - 4|Q|^3 Q E_q(t) \,. \tag{C.12}$$

The canonical equations of motion yield

$$\begin{aligned}
\frac{\partial Q}{\partial \tau} &= P \\
\frac{\partial t}{\partial \tau} &= 4Q^2 \\
\frac{\partial P}{\partial \tau} &= -8p_0Q + 16|Q|^3 E_q(t) \\
\frac{\partial p_0}{\partial \tau} &= 4|Q|^3 Q \frac{\partial E_q(t)}{\partial t}
\end{aligned} \tag{C.13}$$

Because Γ' is not separable, in particular because the equation of motion of coordinate t does not depend on momenta only, one cannot apply a Verlet, or leapfrog integration scheme. Runge-Kutta 4th order was used instead.

The above scheme turned out to actually work worse for $U(r)$ and $V(r)$, in particular because the effective time steps Δt became so small when Q approached 0, that Q could not cross over the origin. For this reason we have resorted to simple leapfrog integration in the extended phase space with $g(t) = 1$, which though superfluous, it allowed one to check the accuracy of the integration by comparing $-p_0$ with the energy obtained explicitly from position and momentum. Special care was paid to $V(r)$ at origin, where the force suddenly changes sign. $V(r)$ was linearized there and the propagation over the origin was performed analytically.

C.1 IBS scaling properties in three dimensions

It is possible though to design a scenario where the potentials lead to essentially different patterns of energy absorption. The original idea was to gain insight into the

screening properties of the electron plasma by studying frequency dependent energy absorption while the quiver amplitude $x_{\mathrm{p}} = \sqrt{I}/\omega^2$ constant. Under these conditions, Rabadan et al. (1994) have observed a resonant like behavior when investigating the scattering of an electron on a Yukawa potential in a high frequency laser field. Fig. C.4 shows the maximum energy transfer ΔE_{max} they have observed as function of $\log \omega$. ΔE_{max} is greatest at a frequency $\omega_{\mathrm{max}} \sim 1$ au which is independent of the impact energy of the electron. They also found ω_{max} to be largely independent of other parameters such as the orientation with respect to the laser field or the impact parameter of the incident electron.
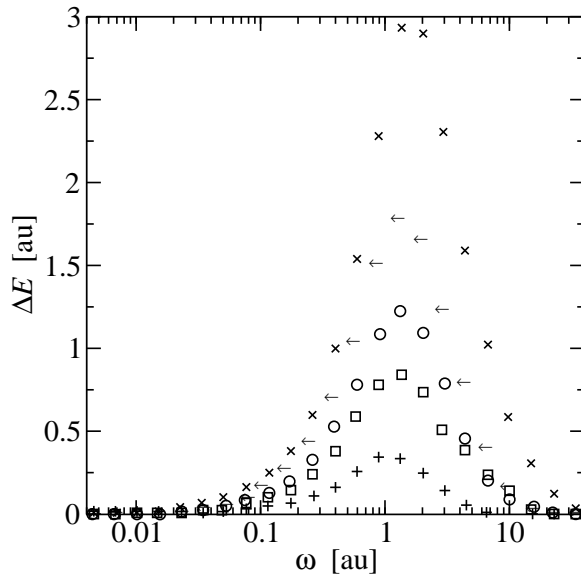
Figure C.4: Maximum energy transfer ΔE_{max} upon scattering of an electron on a Yukawa potential in a laser field. The quiver amplitude was kept constant $x_q = 1.0$ au while the laser frequency ω was varied. Impact energy E of the electron: $\times, E = 0.025$ Hartree; $\leftarrow, E = 0.050$ Hartree; $\circ, E = 0.075$ Hartree; $\square, E = 0.10$ Hartree; $+, E = 0.25$ Hartree. The impact parameter was $b = 2$ au, the Debye length $\lambda_{\mathrm{D}} = 2$ au. The laser field oscillated in the plane of the initial velocity and the origin of the potential, under an angle $\beta = 60°$ to the initial velocity. From Rabadan et al. (1994).

We performed similar investigations on a snapshot of an exploding Xe_{147} cluster, which we illuminated with 2.5 fs probe pulses. The short pulse duration was necessary to prevent cluster expansion. Only plasma properties are of interest here, for which reason photo- and any other ionization effects were also disabled. The intensity of the pulses was increased with increasing photon energy, such that $x_{\mathrm{p}} = 0.2$ au = ct., which corresponds to the ponderomotive amplitude of the Hamburg experiment (Wabnitz et al. 2002) with $\hbar \omega = 12.7$ eV and $I = 7 \times 10^{13}$ W/cm^2. Moreover, we have also varied the parameter a of the model potentials $U(r)$ and $V(r)$. For this reason, the particles were propagated for another 2.5 fs before the probe pulse was applied, to allow the plasma to equilibrate.

Fig. C.5 shows the average absorbed energy due to the applied probe pulse as a
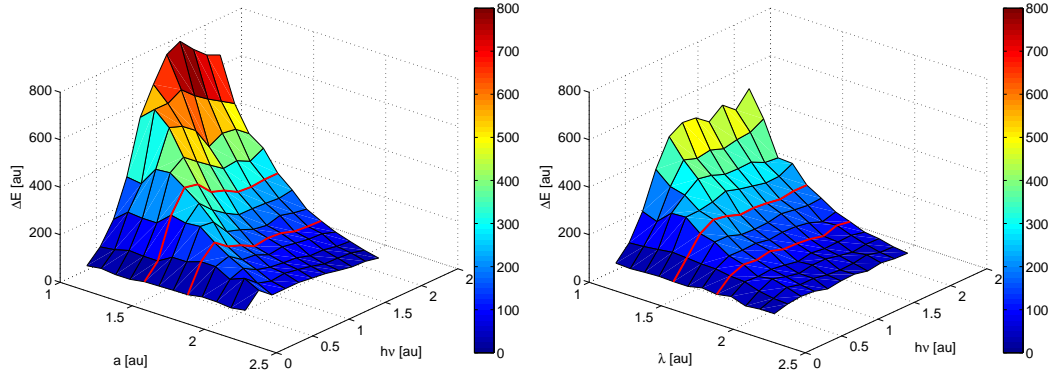
Figure C.5: The role of the model potential on the response of a cluster plasma to a short, periodic driving of variable frequency. The intensity of the 2.5 fs probe pulses was varied along with the frequency, to keep $x_\mathrm{p} = 0.2$ au constant. Left: $U(r)$; Right: $V(r)$. The parameter a of the model potentials was also varied.

function of the laser frequency ω and the parameter a for both $U(r)$ and $V(r)$. For each parameter a, there is a frequency ω for each $U(r)$ yields maximum absorption. $V(r)$ saturates at the same frequency, as the cuts along $a = 1.0$ and $a = 1.4$ confirm in Fig. C.6. $U(r)$ and $V(r)$ perform to a large extend similarly with decreasing a, when they both approach the Coulomb limit. The very high intensities involved with the current findings should also be noted. I scales as $\sim \omega^4$, requiring $I = 3.3 \times 10^{16}$ W/cm^2 for $\hbar\omega = 60$ eV, the highest frequency investigated in Figs. C.5 and C.6. It could be possible, under these circumstances, that the zero difference between $U(r)$ and $V(r)$ observed earlier in Sec. 5.2 could be due to too low an intensity.
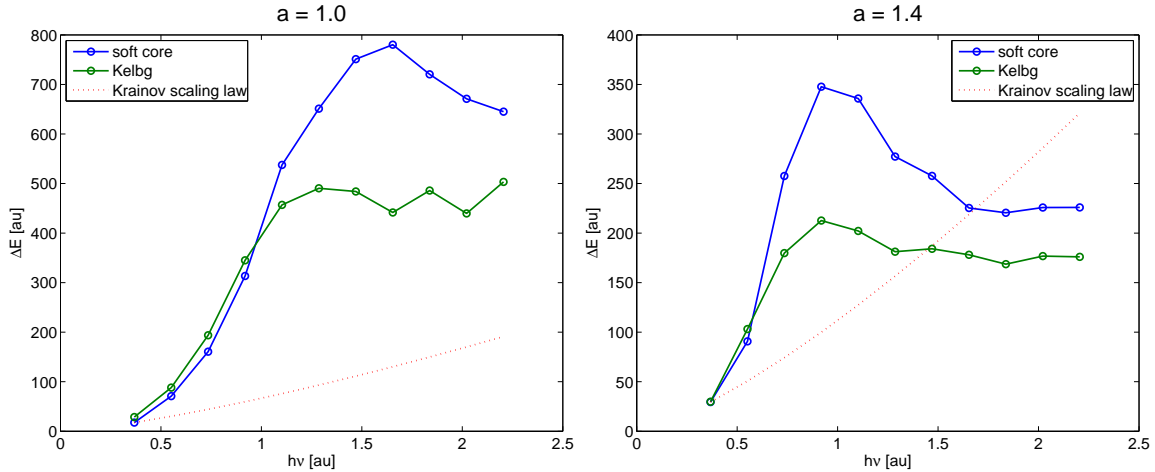
Figure C.6: Cuts along the $a = 1.0$ and respectively $a = 1.4$ lines of Fig. C.5. Blue: $U(r)$; green $V(r)$; dotted lines: extrapolation of the absorbed energy starting from the lowest frequency according to Eq. (5.3), derived by Krainov (2000).

The current scenario is also a very good test for the IBS absorption rate (5.3)

derived by Krainov (2000). According to this equation, the absorbed energy ΔE should increase as $\omega^{4/3}$, because the laser intensity also increases $I = x_{\mathrm{p}}^2 \omega^4$. The dotted lines in Fig. C.6 extrapolate the first data point on each curve according to this prediction. The strong deviation occurs in the whole frequency range, even in the region where both potentials behave essentially as a pure Coulomb potential. Electron correlation effects as well as multiple scattering, characteristic for high density plasma were not included in (5.3). The latter was instead derived for a dilute plasma, where at any moment in time the electron interacts with a single ion and it is not perturbed by any other electron.

Bibliography

FFTW User Manual, 2008. URL `http://www.fftw.org/fftw3_doc/index.html`.

GSL - GNU Scientific Library, 2007. URL `http://www.gnu.org/software/gsl/`.

W. Ackermann et al. Operation of a free-electron laser from the extreme ultraviolet to the water window. *Nature Photonics*, 1(6):336–342, 2007.

L. Adoui et al. Xe(L) X-ray emission from laser-cluster interaction. *Nuclear Instruments and Methods in Physics Research Section B: Beam Interactions with Materials and Atoms*, 205:341–345, 2003.

P. Agostini and L. F. DiMauro. The physics of attosecond light pulses. *Reports on Progress in Physics*, 67(6):813–855, 2004. ISSN 0034-4885.

P. Agostini, F. Fabre, G. Mainfray, G. Petite and N. K. Rahman. Free-free transitions following six-photon ionization of xenon atoms. *Phys. Rev. Lett.*, 42(17):1127–1130, 1979.

M. Altarelli et al. XFEL technical design report. Technical report, DESY, 2006.

V. Ayvazyan et al. A new powerful source for coherent vuv radiation: Demonstration of exponential growth and saturation at the ttf free-electron laser. *The European Physical Journal D - Atomic, Molecular, Optical and Plasma Physics*, 20(1):149–156, 2002a.

V. Ayvazyan et al. Generation of GW radiation pulses from a VUV free-electron laser operating in the femtosecond regime. *Phys. Rev. Lett.*, 88(10):104802, 2002b.

V. Ayvazyan et al. First operation of a free-electron laser generating GW power radiation at 32 nm wavelength. *European Physical Journal D*, 37(2):297–303, 2006.

A. D. Bandrauk and J. Ruel. Charge-resonance-enhanced ionization of molecular ions in intense laser pulses: Geometric and orientation effects. *Phys. Rev. A*, 59(3):2153–, 1999.

S. Banerjee, G. Ravindra Kumar and D. Mathur. Multiple ionization of n_2 in intense, linearly and circularly polarized light fields. *Phys. Rev. A*, 60(1):R25–, 1999.

J. Barnes and P. Hut. A hierarchical $O(N \log N)$ force-calculation algorithm. *Nature*, 324:446–449, 1986.

J. E. Barnes. `treecode v1.4`, 2001. URL `http://ifa.hawaii.edu/~barnes/treecode`.

D. Bauer. Small rare gas clusters in laser fields: ionization and absorption at long and short laser wavelengths. *Journal of Physics B: Atomic, Molecular and Optical Physics*, 37(15):3085–3101, 2004.

A. Becker and F. H. M. Faisal. Intense-field many-body S-matrix theory. *Journal of Physics B: Atomic, Molecular and Optical Physics*, 38(3):R1–R56, 2005.

A. Becker and F. H. M. Faisal. Correlated Keldysh-Faisal-Reiss theory of above-threshold double ionization of He in intense laser fields. *Phys. Rev. A*, 50(4): 3256–3264, 1994.

A. Becker, L. Plaja, P. Moreno, M. Nurhuda and F. H. M. Faisal. Total ionization rates and ion yields of atoms at nonperturbative laser intensities. *Phys. Rev. A*, 64 (2):023408–, 2001.

U. Becker and D. A. Shirley. *VUV and Soft X-Ray Photoionization*. Springer, 1 edition, 1996.

A.-E. Becquerel. Mémoire sur les effets électriques produits sous l'influence des rayons solaires. *Comptes Rendus*, 9:561–567, 1839.

H. A. Bethe and E. Edwin. *Quantum mechanics of one-and two-electron atoms*. Plenum Pub. Corp New York, 1977.

K. Boyer, T. S. Luk, J. C. Solem and C. K. Rhodes. Kinetic energy distributions of ionic fragments produced by subpicosecond multiphoton ionization of n_2. *Phys. Rev. A*, 39(3):1186–1192, 1989.

T. Brabec and F. Krausz. Intense few-cycle laser fields: Frontiers of nonlinear optics. *Rev. Mod. Phys.*, 72(2):545–591, 2000.

B. Bransden and C. Joachain. *Physics of Atoms and Molecules*. Benjamin-Cummings, New York, 2003.

D. M. Brink and G. R. Satchler. *Angular Momentum*. Oxford University Press, 3rd edition, 1993.

F. Brunel. Not-so-resonant, resonant absorption. *Phys. Rev. Lett.*, 59(1):52–, 1987.

W. F. Chan, G. Cooper, X. Guo, G. R. Burton and C. E. Brion. Absolute optical oscillator strengths for the electronic excitation of atoms at high resolution. III. the photoabsorption of argon, krypton, and xenon. *Phys. Rev. A*, 46(1):149–171, 1992.

S. Chandrasekhar. Dynamical Friction. I. General Considerations: the Coefficient of Dynamical Friction. *Astrophysical Journal*, 97:255, 1943.

H. Cheng, L. Greengard and V. Rokhlin. A fast adaptive multipole algorithm in three dimensions. *Journal of Computational Physics*, 155(2):468–498, 1999.

K. Codling, L. J. Frasinski and P. A. Hatherly. On the field ionisation of diatomic molecules by intense laser fields. *Journal of Physics B: Atomic, Molecular and Optical Physics*, 22(12):L321–L327, 1989.

C. Cohen-Tannoudji, J. Dupont-Roc and G. Grynberg. *Introduction to Quantum Electrodynamics*. Wiley, 1997.

R. D. Cowan. *The Theory of Atomic Structure and Spectra*. Los Alamos Series In Basic And Applied Sciences. University Of California Press, 1981. URL `ftp://aphysics.lanl.gov/pub/cowan`.

A. de Castro et al. Non-linear phenomena in atoms and clusters induced by intense vuv radiation from a free electron laser. *Journal of Electron Spectroscopy and Related Phenomena*, 144-147:3–6, 2005.

W. Dehnen. The effect of the outer lindblad resonance of the galactic bar on the local stellar velocity distribution. *The Astronomical Journal*, 119(2):800–812, 2000.

W. Dehnen. A hierarchical (n) force calculation algorithm. *Journal of Computational Physics*, 179:27–42, 2002.

C. Deiss et al. Laser-cluster interaction: X-ray production by short laser pulses. *Phys. Rev. Lett.*, 96(1):013203, 2006.

P. A. M. Dirac. The quantum theory of the emission and absorption of radiation. *Proceedings of the Royal Society of London. Series A, Containing Papers of a Mathematical and Physical Character*, 114(767):243–265, 1927. ISSN 0950-1207.

T. Ditmire, R. A. Smith, J. W. G. Tisch and M. H. R. Hutchinson. High intensity laser absorption by gases of atomic clusters. *Phys. Rev. Lett.*, 78(16):3121, 1997a.

T. Ditmire et al. High-energy ions produced in explosions of superheated atomic clusters. *Nature*, 386(6620):54–56, 1997b.

T. Ditmire et al. Explosion of atomic clusters heated by high-intensity femtosecond laser pulses. *Phys. Rev. A*, 57(1):369, 1998.

T. Ditmire et al. Nuclear fusion from explosions of femtosecond laser-heated deuterium clusters. *Nature*, 398(6727):489–492, 1999.

T. R. Dittrich et al. Diagnosis of pusher-fuel mix in indirectly driven nova implosions. *Phys. Rev. Lett.*, 73(17):2324–, 1994.

T. Döppner, T. Fennel, P. Radcliffe, J. Tiggesbäumker and K.-H. Meiwes-Broer. Ion and electron emission from silver nanoparticles in intense laser fields. *Phys. Rev. A*, 73(3):031202, 2006.

118

R. Dorner et al. Cold target recoil ion momentum spectroscopy: a 'momentum microscope' to view atomic collision dynamics. *Physics Reports*, 330(2-3):95–192, 2000.

J. Doye. Lennard-jones clusters, 1997. URL `http://physchem.ox.ac.uk/~doye/jon/structures/LJ.html`.

M. Drescher et al. X-ray pulses approaching the attosecond frontier. *Science*, 291 (5510):1923–1927, 2001.

M. Drescher et al. Time-resolved atomic inner-shell spectroscopy. *Nature*, 419(6909): 803–807, 2002. ISSN 0028-0836.

A. Einstein. Über einen die Erzeugung und Verwandlung des Lichtes betreffenden heuristischen Gesichtspunkt. *Annalen der Physik*, 322(6):132–148, 1905.

F. H. M. Faisal. Multiple absorption of laser photons by atoms. *Journal of Physics B: Atomic and Molecular Physics*, 6(4):L89–L92, 1973.

J. Feldhaus, J. Arthur and J. B. Hastings. X-ray free-electron lasers. *Journal of Physics B: Atomic, Molecular and Optical Physics*, 38:S799, 2005.

T. Fennel et al. Plasmon-enhanced electron acceleration in intense laser metal-cluster interactions. *Phys. Rev. Lett.*, 98(14):143401, 2007.

L. J. Frasinski et al. Femtosecond dynamics of multielectron dissociative ionization by use of a picosecond laser. *Phys. Rev. Lett.*, 58(23):2424–2427, 1987.

H. Friedrich. *Theoretical Atomic Physics*. Springer, 3rd edition, 2006.

I. Georgescu, U. Saalmann and J. M. Rost. Clusters under strong vuv pulses: A quantum-classical hybrid description incorporating plasma effects. *Phys. Rev. A*, 76(4):043203, 2007a.

I. Georgescu, U. Saalmann and J. M. Rost. Attosecond resolved charging of ions in a rare-gas cluster. *Phys. Rev. Lett.*, 99(18):183002, 2007b.

M. Göppert-Mayer. Über Elementarakte mit zwei Quantensprüngen. *Annalen der Physik*, 401(3):273–294, 1931.

E. Goulielmakis et al. Direct measurement of light waves. *Science*, 305(5688):1267–1269, 2004.

E. Goulielmakis et al. Attosecond control and measurement: Lightwave electronics. *Science*, 317(5839):769–775, 2007.

L. Greengard and V. Rokhlin. A fast algorithm for particle simulations. *Journal of Computational Physics*, 73(2):325–348, 1987.

G. Grillon et al. Deuterium-deuterium fusion dynamics in low-density molecular-cluster jets irradiated by intense ultrafast laser pulses. *Phys. Rev. Lett.*, 89(6): 065005, 2002.

H. Haberland. *Clusters of Atoms and Molecules I.* Springer-Verlag, 1995.

H. Haberland et al. Filling of micron-sized contact holes with copper by energetic cluster impact. *Journal of Vacuum Science & Technology A: Vacuum, Surfaces, and Films*, 12(5):2925–2930, 1994.

O. F. Hagena and W. Obert. Cluster formation in expanding supersonic jets: Effect of pressure, temperature, nozzle size, and test gas. *J. Chem. Phys.*, 56(5):1793–1802, 1972.

W. Hallwachs. Ueber den Einfluss des Lichtes auf electrostatisch geladene Körper. *Annalen der Physik und Chemie*, 269(2):301–312, 1888a.

W. Hallwachs. Ueber die Electrisirung von Metallplatten durch Bestrahlung mit electrischem Licht. *Annalen der Physik und Chemie*, 270(8A):731–734, 1888b.

M. Hentschel et al. Attosecond metrology. *Nature*, 414(6863):509–513, 2001. ISSN 0028-0836.

H. Hertz. Ueber einen Einfluss des ultravioletten Lichtes auf die electrische Entladung. *Annalen der Physik und Chemie*, 267(8):983–1000, 1887.

J. Itatani et al. Tomographic imaging of molecular orbitals. *Nature*, 432(7019):867–871, 2004. ISSN 0028-0836.

J. Itatani et al. Controlling high harmonic generation with molecular wave packets. *Phys. Rev. Lett.*, 94(12):123902, 2005.

M. Y. Ivanov, M. Spanner and O. Smirnova. Anatomy of strong field ionization. *Journal of Modern Optics*, 52(2):165–184, 2005.

R. A. James. The solution of poisson's equation for isolated source distributions. *Journal of Computational Physics*, 25(2):71–93, 1977.

C. Jungreuthmayer, L. Ramunno, J. Zanghellini and T. Brabec. Intense vuv laser cluster interaction in the strong coupling regime. *Journal of Physics B: Atomic, Molecular and Optical Physics*, 38(16):3029–3036, 2005.

G. L. Kamta and A. D. Bandrauk. Nonsymmetric molecules driven by intense few-cycle laser pulses: Phase and orientation dependence of enhanced ionization. *Phys. Rev. A*, 76(5):053409, 2007.

L. Keldysh. Ionization in the field of a strong electromagnetic wave. *Zh. Eksp. Teor. Fiz*, 47:1945–1956, 1964.

R. Kienberger et al. Steering attosecond electron wave packets with light. *Science*, 297(5584):1144–1148, 2002.

R. Kienberger et al. Atomic transient recorder. *Nature*, 427(6977):817–821, 2004.

T. C. Killian et al. Creation of an ultracold neutral plasma. *Phys. Rev. Lett.*, 83(23): 4776–4779, 1999.

L. Köller et al. Plasmon-enhanced multi-ionization of small metal clusters in strong femtosecond laser fields. *Phys. Rev. Lett.*, 82(19):3783–3786, 1999.

G. Kracke, H. Marxer, J. T. Broad and J. S. Briggs. Multiphoton ionisation of atomic hydrogen and the angular distribution of photoelectrons. *Zeitschrift für Physik D Atoms, Molecules and Clusters*, 8(1):103–104, 1988.

V. P. Krainov. Inverse stimulated bremsstrahlung of slow electrons under coulomb scattering. *Journal of Physics B: Atomic, Molecular and Optical Physics*, 33:1585–1595, 2000.

F. Krausz. Private communication. 2007.

S. Kulin, T. C. Killian, S. D. Bergeson and S. L. Rolston. Plasma oscillations and expansion of an ultracold neutral plasma. *Phys. Rev. Lett.*, 85(2):318–321, 2000.

T. Laarmann et al. Interaction of argon clusters with intense vuv-laser radiation: The role of electronic structure in the energy-deposition process. *Phys. Rev. Lett.*, 92(14):143401, 2004.

T. Laarmann et al. Emission of thermally activated electrons from rare gas clusters irradiated with intense vuv light pulses from a free electron laser. *Phys. Rev. Lett.*, 95(6):063402, 2005.

E. Lamour, C. Prigent, J. P. Rozet and D. Vernhet. Physical parameter dependence of the X-ray generation in intense laser-cluster interaction. *Nuclear Instruments and Methods in Physics Research Section B: Beam Interactions with Materials and Atoms*, 235(1-4):408–413, 2005.

L. D. Landau and E. M. Lifshitz. Mechanics. In *Course of theoretical physics*, volume I. Butterworth-Heinemann, 3rd edition, 2005.

I. Last and J. Jortner. Quasiresonance ionization of large multicharged clusters in a strong laser field. *Phys. Rev. A*, 60(3):2215–, 1999.

P. Lenard. Ueber die lichtelektrische wirkung. *Annalen der Physik*, 313(5):149–198, 1902.

R. R. Lindberg, A. E. Charman, J. S. Wurtele and L. Friedland. Robust autoresonant excitation in the plasma beat-wave accelerator. *Phys. Rev. Lett.*, 93(5):055001, 2004.

F. Lindner et al. Attosecond double-slit experiment. *Phys. Rev. Lett.*, 95(4):040401, 2005.

R. Lopez-Martens et al. Amplitude and phase control of attosecond light pulses. *Phys. Rev. Lett.*, 94(3):033001, 2005.

W. M. MacDonald, M. N. Rosenbluth and W. Chuck. Relaxation of a system of particles with coulomb interactions. *Phys. Rev.*, 107(2):350–353, 1957.

K. W. Madison et al. Role of laser-pulse duration in the neutron yield of deuterium cluster targets. *Phys. Rev. A*, 70(5):053201–7, 2004.

T. H. Maiman. Stimulated optical radiation in ruby. *Nature*, 187(4736):493–494, 1960.

T. H. Maiman. Ruby Laser Systems. *U.S. Patent*, pages 3,353,115, 1967.

A. McPherson, B. D. Thompson, A. B. Borisov, K. Boyer and C. K. Rhodes. Multiphoton-induced x-ray emission at 4-5 kev from xe atoms with multiple core vacancies. *Nature*, 370(6491):631–634, 1994.

G. Mie. Beiträge zur Optik trüber Medien, speziell kolloidaler Metallösungen. *Annalen der Physik*, 330(3):377–445, 1908.

R. A. Millikan. A Direct Photoelectric Determination of Planck's "h". *Phys. Rev.*, 7 (3):355–388, 1916.

T. Möller. Private communication. 2007.

P. Mulser, M. Kanapathipillai and D. H. H. Hoffmann. Two very efficient nonlinear laser absorption mechanisms in clusters. *Phys. Rev. Lett.*, 95(10):103401, 2005.

I. Napari and H. Vehkamaki. The role of dimers in evaporation of small argon clusters. *The Journal of Chemical Physics*, 121(2):819–822, 2004.

R. Neutze, R. Wouts, D. van der Spoel, E. Weckert and J. Hajdu. Potential for biomolecular imaging with femtosecond x-ray pulses. *Nature*, 406(6797):752–757, 2000. ISSN 0028-0836.

H. Niikura et al. Sub-laser-cycle electron pulses for probing molecular dynamics. *Nature*, 417(6892):917–922, 2002. ISSN 0028-0836.

H. Niikura et al. Probing molecular dynamics with attosecond resolution using correlated wave packet pairs. *Nature*, 421(6925):826–829, 2003. ISSN 0028-0836.

J. A. Northby. Structure and binding of Lennard-Jones clusters: $13 \leq N \leq 147$. *The Journal of Chemical Physics*, 87(10):6166–6177, 1987.

S. Pfalzner and P. Gibbon. *Many-Body Tree Methods in Physics*. Cambridge University Press, 1996.

M. Planck. Ueber das Gesetz der Energieverteilung im Normalspectrum. *Annalen der Physik*, 309(3):553–563, 1901.

T. Pohl, T. Pattard and J. M. Rost. Relaxation to nonequilibrium in expanding ultracold neutral plasmas. *Phys. Rev. Lett.*, 94(20):205003, 2005.

R. M. Potvliege and R. Shakeshaft. Multiphoton processes in an intense laser field: Harmonic generation and total ionization rates for atomic hydrogen. *Phys. Rev. A*, 40(6):3061–, 1989.

M. Preto and S. Tremaine. A class of symplectic integrators with adaptive time step for separable hamiltonian systems. *The Astronomical Journal*, 118(5):2532–2541, 1999.

I. Rabadan, L. Méndez and A. S. Dickinson. Electron scattering in a yukawa potential in the presence of a high-frequency laser field. *Journal of Physics B: Atomic, Molecular and Optical Physics*, 27:2089–2102, 1994.

H. R. Reiss. Effect of an intense electromagnetic field on a weakly bound system. *Phys. Rev. A*, 22(5):1786–1813, 1980.

C. Rose-Petruck, K. J. Schafer, K. R. Wilson and C. P. J. Barty. Ultrafast electron dynamics and inner-shell ionization in laser driven clusters. *Phys. Rev. A*, 55(2): 1182–, 1997.

J. M. Rost. Analytical total photo cross section for atoms. *Journal of Physics B: Atomic, Molecular and Optical Physics*, 28(19):L601–L606, 1995.

M. Rusek and A. Orlowski. Different mechanisms of cluster explosion within a unified smooth particle hydrodynamics thomas-fermi approach: Optical and short-wavelength regimes compared. *Phys. Rev. A*, 71(4):043202, 2005.

U. Saalmann and J.-M. Rost. Ionization of clusters in strong X-ray laser pulses. *Phys. Rev. Lett.*, 89(14):143401, 2002.

U. Saalmann and J.-M. Rost. Ionization of clusters in intense laser pulses through collective electron dynamics. *Phys. Rev. Lett.*, 91(22):223401, 2003.

U. Saalmann, C. Siedschlag and J. M. Rost. Mechanisms of cluster ionization in strong laser pulses. *Journal of Physics B: Atomic, Molecular and Optical Physics*, 39(4):R39–R77, 2006.

U. Saalmann, I. Georgescu and J. M. Rost. Tracing non-equilibrium plasma dynamics on the attosecond timescale in small clusters. *New Journal of Physics*, 10(2): 025014–, 2008. ISSN 1367-2630.

E. Saldin, E. Schneidmiller and M. Yurkov. A new technique to generate 100 gw-level attosecond x-ray pulses from the x-ray sase fels. *Optics Communications*, 239(1-3): 161–172, 2004a.

E. L. Saldin, E. A. Schneidmiller and M. V. Yurkov. Terawatt-scale sub-10-fs laser technology - key to generation of gw-level attosecond pulses in x-ray free electron laser. *Optics Communications*, 237(1-3):153–164, 2004b.

J. A. R. Samson and W. C. Stolte. Precision measurements of the total photoionization cross-sections of he, ne, ar, kr, and xe. *Journal of Electron Spectroscopy and Related Phenomena*, 123(2-3):265–276, 2002.

R. Santra and C. H. Greene. Xenon clusters in intense VUV laser fields. *Phys. Rev. Lett.*, 91(23):233401, 2003.

R. Santra and C. H. Greene. Multiphoton ionization of xenon in the vuv regime. *Phys. Rev. A*, 70(5):053401, 2004.

A. L. Schawlow and C. H. Townes. Infrared and optical masers. *Phys. Rev.*, 112(6): 1940–1949, 1958.

E. Schrödinger. Quantisierung als Eigenwertproblem. *Annalen der Physik*, 386(18): 109–139, 1926.

W. A. Schroeder et al. Pump laser wavelength-dependent control of the efficiency of kilovolt x-ray emission from atomic clusters. *Journal of Physics B: Atomic, Molecular and Optical Physics*, 31(22):5031–5051, 1998.

M. Schultze et al. Powerful 170-attosecond XUV pulses generated with few-cycle laser pulses and broadband multilayer optics. *New Journal of Physics*, 9(7):243, 2007.

T. Seideman, M. Y. Ivanov and P. B. Corkum. Role of electron localization in intense-field molecular ionization. *Phys. Rev. Lett.*, 75(15):2819–2822, 1995.

G. H. Shortley. Line strengths in intermediate coupling. *Phys. Rev.*, 47(4):295–300, 1935.

C. Siedschlag and J.-M. Rost. Fragmentation in intense time-dependent fields. *Few-Body Systems*, 31:211–216, 2002.

C. Siedschlag and J.-M. Rost. Small rare-gas clusters in soft X-ray pulses. *Phys. Rev. Lett.*, 93(4):043402, 2004.

C. Siedschlag and J. M. Rost. Enhanced ionization in small rare-gas clusters. *Phys. Rev. A*, 67(1):013404–, 2003.

E. M. Snyder, S. A. Buzza and A. W. Castleman, Jr. Intense field-matter interactions: Multiple ionization of clusters. *Phys. Rev. Lett.*, 77(16):3347–3350, 1996.

L. J. Spitzer. *Physics of Fully Ionized Gases*. John Wiley & Sons, New York, 1962.

T. Taguchi, T. M. Antonsen and H. M. Milchberg. Resonant heating of a cluster plasma by intense laser light. *Phys. Rev. Lett.*, 92(20):205003, 2004.

R. Torres et al. Probing orbital structure of polyatomic molecules by high-order harmonic generation. *Phys. Rev. Lett.*, 98(20):203007, 2007.

M. Uiberacker et al. Attosecond real-time observation of electron tunnelling in atoms. *Nature*, 446(7136):627–632, 2007.

J. Ullrich et al. Recoil-ion and electron momentum spectroscopy: reaction-microscopes. *Reports on Progress in Physics*, 66(9):1463–1545, 2003.

H. Wabnitz et al. Multiple ionization of atom clusters by intense soft X-rays from a free electron laser. *Nature*, 420:482–485, 2002.

Z. B. Walters, R. Santra and C. H. Greene. Interaction of intense vuv radiation with large xenon clusters. *Phys. Rev. A*, 74(4):043204, 2006.

C. A. White and M. Head-Gordon. Derivation and efficient implementation of the fast multipole method. *The Journal of Chemical Physics*, 101(8):6593–6605, 1994.

R. Williams. Becquerel photovoltaic effect in binary compounds. *J. Chem. Phys.*, 32 (5):1505–1514, 1960.

XFEL. The european x-ray laser project xfel, 2008. URL `http://xfel.desy.de`.

S. Zamith et al. Control of the production of highly charged ions in femtosecond-laser cluster fragmentation. *Phys. Rev. A*, 70(1):011201–4, 2004.

D. Zeidler et al. Controlling attosecond double ionization dynamics via molecular alignment. *Phys. Rev. Lett.*, 95(20):203003, 2005.

Y. Zel'dovich and Y. Raizer. *Physics of Shock Waves and High-Temperature Hydrodynamic Phenomena*, volume I. Academic Press, New York, 1966.

A. A. Zholents and W. M. Fawley. Proposal for intense attosecond radiation from an x-ray free-electron laser. *Phys. Rev. Lett.*, 92(22):224801–4, 2004.

T. Zuo and A. D. Bandrauk. Charge-resonance-enhanced ionization of diatomic molecular ions by intense lasers. *Phys. Rev. A*, 52(4):R2511, 1995.

J. Zweiback, T. Ditmire and M. D. Perry. Femtosecond time-resolved studies of the dynamics of noble-gas cluster explosions. *Phys. Rev. A*, 59(5):R3166–R3169, 1999.

J. Zweiback et al. Nuclear fusion driven by coulomb explosions of large deuterium clusters. *Phys. Rev. Lett.*, 84(12):2634, 2000.

G. Zwicknagel. Molecular dynamics simulations of the dynamics of correlations and relaxation in an OCP. *Contributions to Plasma Physics*, 39(1-2):155–158, 1999.

Acknowledgements

Versicherung

Hiermit versichere ich, dass ich die vorliegende Arbeit ohne unzulässige Hilfe Dritter und ohne Benutzung anderer als der angegebenen Hilfsmittel angefertigt habe; die aus fremden Quellen direkt oder indirekt übernommenen Gedanken sind als solche kenntlich gemacht. Die Arbeit wurde bisher weder im Inland noch im Ausland in gleicher oder ähnlicher Form einer anderen Prüfungsbehörde vorgelegt.

Die vorliegende Dissertation wurde am Max-Planck-Institut für Physik komplexer Systeme in der Abteilung "Endliche Systeme" unter der wissenschaftlichen Betreuung von Herrn Professor Dr. Jan-Michael Rost und von Herrn Dr. habil. Ulf Saalmann angefertigt.

Ich erkenne hiermit die Promotionsordnung der Fakultät Mathematik und Naturwissenschaften der Technischen Universität Dresden vom 17. April 2003 an.

Ionuţ Georgescu